New Developments in GaAs-based Quantum Cascade Lasers

Chris Neil Atkins

PhD Thesis

October 2013

Department of Physics and Astronomy

Abstract

This thesis presents a study of the design and optimisation of gallium-arsenide-based quantum cascade lasers (QCLs). Traditionally, the optical and electrical performance of these devices has been inferior in comparison to QCLs that are based on the InP material system, due mainly to the limitations imposed on performance by the intrinsic material properties of GaAs. In an attempt to improve the performance of GaAs QCLs, indium-gallium-phosphide and indium-aluminium-phosphide have been used as the waveguide cladding layers in several new QCL designs. These two materials combine low waveguide losses with a high confinement of the laser optical mode, and are easily integrated into typical GaAs QCL structures.

Devices containing a double-phonon relaxation active region design have been combined with an InAlP waveguide, with the result being that the lowest threshold currents yet observed for a GaAs-based QCL have been observed - 2.1kA/cm^2 and 4.0kA/cm^2 at 240K and 300K respectively. Accompanying these low threshold currents however, were large operating voltages approaching 30V at room-temperature and 60V at 80K. These voltages were responsible for a high rate of device failure due to overheating. In an attempt to address this situation, two transitional layer (TL) designs were applied at the QCL GaAs/InAlP interfaces in order to aid electron flow at these points. The addition of the TLs resulted in a lowering of operating voltage by ~12V and 30V at 300K and 240K respectively, however threshold current density increased to 5.1kA/cm^2 and 2.7kA/cm^2 at the same temperatures.

By utilising a high-reflectivity coating and epi-layer down bonding process, a QCL comprising an InGaP waveguide and double-phonon active region was observed to operate in continuous-wave mode up to a temperature of 80K, with an optical output power of 26mW.

Publications

C. N. Atkins, A. B. Krysa, D. G. Revin, K. Kennedy, J. P. Commin, and J.W. Cockburn, *Low threshold room temperature GaAs/AlGaAs quantum cascade laser with InAlP waveguide,* Electronics Letters, **47**, 1193-1194, (2011).

A. B. Krysa, D. G. Revin, J. P. Commin, C. N. Atkins, K. Kennedy, Y. Qiu and J. W. Cockburn, *Room-Temperature GaAs/AlGaAs Quantum Cascade Lasers Grown by Metal-Organic Vapor Phase Epitaxy*. IEEE Photonics Technology Letters, **23**, 774-776, (2011).

D. G. Revin, R. S. Hassan, C. N. Atkins, J. W. Cockburn, A. B. Krysa, K. Kennedy and A. Belyanin, *Spectroscopic study of transparency current in mid-infrared quantum cascade lasers*, Optics Express, **20**, 18925-18930, (2012).

Presentations

D. G. Revin, C. N. Atkins, J. P. Commin, J. W. Cockburn, Y. Qiu, T. Walther and A. B. Krysa, *Room temperature GaAs/AlGaAs quantum cascade lasers with InGaP and InAlP waveguides*, 2011 Conference on Lasers and Electro-Optics: Laser Science to Photonic Applications, Baltimore MD, (2011).

Acknowledgements

First and foremost I'd like to thank my supervisor Professor John Cockburn for giving me the opportunity to undertake my PhD at Sheffield, and for the support, advice and guidance along the way. I am also thankful for the knowledge and assistance provided by Dr Dmitry Revin throughout my time here, without which I would have been lost on many occasions. His humour, words of wisdom and stories of life in the old Soviet Union have made working in the QCL group an enlightening experience - спасибо Дмитрий!

Paul Commin was responsible for honing my skills in the cleanroom and lab during my early days as a postgrad, in addition to helping me quickly settle in to the group. Tales of his weekend shenanigans always made Mondays more entertaining. Cleanroom guru Ken Kennedy has provided vital help with all things related to device processing, making what can at times be a testing endeavour so much easier. I would also like to thank Dr Andrey Krysa for growing the high-quality semiconductor samples which underpin the experimental work presented in this thesis.

Dr Luke Wilson has been another welcome source of help and advice along the way, and also gave me the opportunity to help out in the first year physics lab which has been a thoroughly rewarding experience (and kept my bank balance just about in the black). All the staff and fellow students in the physics department at Sheffield that have made it such a great place to work have my deepest thanks - in particular Dyfrig Davies, Nathan Porter and spin-instructor extraordinaire and supplier of smiles Tracy Hilton ☺.

My dear friends Cole, Jennie, Louise and Flash have been responsible for countless good times over the years, as has my girlfriend Bex - with whom I have shared so many adventures ♡. You have kept me going through it all, and I'm forever indebted to you.

Lastly, I'd like to save the biggest thank-you of all for my mum Jill, who has been selfless in her support for me from the very start, and without whom I could never have got this far. X

Glossary

As an aid to the reader listed below are the various terms used throughout this thesis, along with their definitions.

W_{if} .....electronic transition rate between initial and final states *i* and *f*.

W_{if}^{sp} .....spontaneous transition rate between initial and final states *i* and *f*.

ψ_i / ψ_f.....initial and final wavefunctions of an electron undergoing a transition between states *i* and *f*.

H' .....interaction Hamiltonian for electronic transition between states *i* and *f*.

$\delta(Ef - Ei - \hbar\omega)$ .....density of final states of electronic system undergoing transitions between states *i* and *f*.

z_{ij} .....dipole matrix element for an electronic transition between states *i* and *j*.

E_{ij} .....transition energy between levels *i* and *j*.

$\boldsymbol{e}$ .....polarisation vector of electric field perturbing an electronic system.

$\boldsymbol{p}$ .....linear momentum operator.

E_0 .....amplitude of perturbing electric field.

n_{ref} .....refractive index of medium of interest.

$\alpha_{Tot}/\alpha_W/\alpha_M$ .....total, waveguide and mirror losses from laser cavity.

Γ .....optical mode confinement factor.

ε_0 .....permittivity of free space.

$\varepsilon_1/\varepsilon_2$ .....real and imaginary parts of the complex dielectric constant.

ε_∞ .....high-frequency dielectric constant.

G_p .....peak material gain.

G_{Mod} .....modal gain; the material gain multiplied by the mode confinement factor Γ.

g_c .....gain cross-section; the peak modal gain per unit of upper state population.

g .....gain coefficient; the peak gain per unit threshold current density.

λ .....laser emission wavelength.

E_λ .....QCL emission energy expressed in eV.

$2\gamma_{ij}$ .....spontaneous emission full width at half-maximum.

n_i .....electron sheet density in subband i.

ΔE_c .....conduction band offset.

J .....QCL current density.

J_{th} .....QCL threshold current density.

T_0 .....QCL characteristic temperature.

V_{op} .....QCL operating voltage.

ΔE_V.....QCL active region voltage defect.

dP/dI .....QCL slope efficiency.

S .....above-threshold photon flux density per QCL period, per unit active region width.

τ_n .....electron lifetime at energy level n.

τ_n^{-1} .....electron transition rate from energy level n.

Δn .....electron population difference between intersubband energy levels.

δ .....optical path difference resulting from the changing mirror position within the FTIR interferometer.

v .....emission wavenumber.

$I(\delta)$ .....intensity of IR radiation as a function of optical path difference.

$B(v)$ .....intensity of IR radiation as a function of wavenumber.

R .....reflectivity of the laser facet.

L .....length of the QCL cavity.

L_p .....length of a single active region period.

N_p .....number of QCL core region repeat periods.

c .....speed of light in a vacuum.

e .....electronic charge.

m^* .....electron effective mass.

ω .....angular frequency.

Contents

Chapter Three - Semiconductor Growth and Device Fabrication and Characterisation

Chapter Four - GaAs-based QCLs with InGaP and InAlP Waveguides

Chapter One

Introduction to Quantum Cascade Lasers

1.1 Introduction

In 1994, the quantum cascade laser emerged as an innovative and unique semiconductor device operating in the infrared (IR) region of the spectrum. Since that time the QCL has inspired a large body of scientific research, and today occupies a key position within the field of IR spectroscopy, where it provides the basis for many modern spectroscopic systems. As will be shown over the course of this thesis, QCLs differ radically from conventional semiconductor lasers, both in the way they generate light, and in the range of wavelengths at which different devices can operate. QCLs are *unipolar* devices; i.e. only electrons are involved in the process of generating photons, which are produced when electrons make *intersubband* optical transitions between confined energy states within the conduction band of the QCL structure. This is in direct contrast to devices such as, for example, semiconductor diode lasers which produce light through the recombination of electrons and holes across an energy bandgap. The design scheme of the QCL is extremely flexible, and allows a large variation in output wavelength through judicious tailoring of the energy levels involved in the optical transition - optical output is not necessarily limited by the material from which a device is fabricated. This wavelength flexibility, combined with the fact that many molecules have rotational and vibrational modes resonant with energies corresponding to the mid-infrared portion of the spectrum, means that QCLs now fulfil a vital role at the heart of many gas sensing applications[1,2]. Gases such as methane (CH_4), ammonia (NH_3), sulphur dioxide (SO_2) and carbon monoxide (CO) to name but a few all have absorption peaks in the mid-infrared, and can thus be detected by spectroscopic systems that incorporate a QCL with the appropriate operating wavelength. Gas sensing applications

that utilise mid-infrared lasers also benefit from two atmospheric windows that exist at approximately $3 \leq \lambda \leq 5\mu m$ and $8 \leq \lambda \leq 14\mu m$, in which the attenuation of IR radiation by water vapour in the atmosphere is at a minimum. QCL-based technologies have now been successfully commercialised into products that offer detection at the parts per million to parts per billion level for a diverse range of gases in various settings. These include waste and pollutant monitoring in industrial installations as well as the natural environment[3-5]. Other areas of exploitation include QCL laser systems for so-called infrared countermeasures - applications that involve confusing the radar and guidance systems typically found in military hardware[6] - counter-terrorism applications in the form of explosive detection[7] and breath analysis for health monitoring[8].

1.2 Thesis Outline

This thesis presents an experimental study of gallium-arsenide (GaAs) based quantum cascade lasers (QCLs), with an emphasis on enhancing device performance through optimisation of the laser waveguide structure. Chapter one gives a general introduction to the quantum cascade laser, firstly from an historical perspective, before then introducing the basic concepts behind QCL design and operation. Chapter two discusses some of the theoretical tools that can be used to qualitatively predict key QCL parameters, while chapter three outlines the processes involved in the fabrication and characterisation of the devices presented in the subsequent experimental sections of this thesis. Chapter four begins with a discussion of QCL waveguides as they relate to GaAs-based devices, which is followed by a detailed presentation of the design and performance of GaAs/AlGaAs QCLs which incorporate indium-gallium-phosphide (InGaP) and indium-aluminium-phosphide (InAlP) layers to form the device waveguide. A comparison of their performance relative to previous GaAs-based lasers is also given. Chapter five concerns the optimisation of QCLs with InAlP waveguides, particularly with regard to the large operating voltages that are a feature of the devices presented in chapter four. Again, several different device designs are described and their corresponding operating characteristics compared. Chapter six describes several QCLs with InGaP waveguides, high-reflectivity facet coatings and a redesigned active region that have been observed to operate in continuous-wave mode - an important

advancement in device efficiency when compared to the previous lasers operating in pulsed mode. Finally, chapter seven provides a summary of all experimental work carried out, conclusions that may be drawn from the results and a discussion of the likely direction of future studies.

1.3 Historical Development of the Quantum Cascade Laser

The quantum cascade laser has a development history stretching back over forty years, beginning with the pioneering work of two Soviet physicists who laid the theoretical foundations upon which subsequent applied developments would build. In 1971, Kazarinov and Suris[9] first suggested the possibility that electromagnetic waves might be amplified by a semiconductor superlattice under the influence of an external electric field, due to the optical transitions of electrons between confined states within the lattice quantum wells. Due to limitations in the semiconductor growth techniques of the time, it was not possible to produce the extremely thin and abrupt semiconductor layers required to form these superlattices, and over a decade would pass before the ideas proposed by Kasarinov and Suris could be applied and developed in the laboratory. By the mid-1980s however, semiconductor growth technology had advanced sufficiently to allow the fabrication of high quality semiconductor superlattices, and soon after, the first investigations into the nature of the intersubband transitions within these structures were being carried out.

Intersubband absorption in a semiconductor quantum well was first observed by West and Eglash[10] in 1985, who used an infrared laser incident on a 50-period GaAs/AlGaAs superlattice to probe the absorption due to the quantised conduction band states corresponding to energies of 152meV and 121meV (8.2μm and 10.2μm). Observation of intersubband emission followed soon after, when Helm and co-workers reported infrared emission from three conduction band energy levels of a GaAs/AlGaAs superlattice at 50μm, 69μm and 113μm[11]. Sandwiched between these two important observations was the first report, by Capasso et al, of resonant tunnelling of electrons through an InGaAs/AlInAs semiconductor superlattice[12]. With the superlattice placed

under an appropriate electric field, several peaks in photocurrent were observed corresponding to the alignment of the confined quantum well ground state with an excited state of the adjacent well. Under these conditions, electrons can resonantly tunnel between the wells from ground to excited state through the intervening AlInAs barriers. Electrons can then transition (non-radiatively in this case) to the ground state before tunnelling into the next well. This process of resonant electron tunnelling, whereby electrons 'cascade' through a superlattice structure, is key to the operation of the QCL.

In parallel with these experimental breakthroughs, theoretical work was being published that forwarded various proposals for infrared lasers that would utilise the very same intersubband transitions and resonant tunnelling processes. In 1986 Yuh and Wang[13] proposed an intersubband laser consisting of a semiconductor superlattice divided into three distinct sections; an active region in which electrons would make optical transitions between an upper and lower miniband of electronic states within the conduction band, and two regions either side of this from which electrons would be injected into, and extracted from the active region via appropriately aligned minibands. Population inversion would be maintained via the current injected into the upper miniband of the injection region, while the wavelength of the device would be tailored by altering the energy spacing of the upper and lower active region minibands. A second proposal, presented by Liu[14], suggested a GaAs/AlGaAs superlattice in which optical transitions would be made by electrons transitioning between the confined states within the quantum wells, rather than the minibands proposed by Yuh and Wang. As had been experimentally demonstrated by Capasso et al, once a transition had been made between the upper level and the ground state - and provided the states were suitably aligned - electrons could resonantly tunnel between wells into the next excited state before making another optical transition. This process would be repeated along the entire superlattice structure, with the requisite population inversion being achieved by ensuring that the tunnelling time through the barriers was shorter than the lifetime of the radiative transitions within the quantum wells.

Much of this experimental and theoretical work would be brought together when, in 1994, Faist et al[15] reported the first demonstration of working laser based on intersubband transitions within the conduction band of a semiconductor superlattice. This device - christened the quantum cascade laser - would kick-start a new field of

infrared laser physics and lead to a burgeoning interest in such devices. The laser itself was based on the InGaAs/AlInAs/InP material system, with a core comprising of 25 repeated periods of a 3-quantum well active region followed by a superlattice of wells and barriers forming an injection region. The core was surrounded by a waveguide formed by an upper layer of AlInAs, while the InP substrate acted as the lower portion of the waveguide. A perceived stumbling block to the experimental realisation of the QCL had been the notion that laser action would be severely compromised by the rate of non-radiative optical phonon scattering of electrons - which occurs on a picosecond scale - being much faster than the nanosecond-scale rate of radiative spontaneous emission. It was assumed that this would make device operation prohibitively inefficient, and also limit any emission that may be possible to energies below that of the LO phonon energy (~34meV for InGaAs), i.e. the far infrared. Faist and co-workers however, were the first to realise that once lasing had been achieved, the rate of *stimulated* photon emission would approach that of the non-radiative LO phonon scattering, thereby greatly increasing the efficiency of the device active region[16]. Their new laser generated photons via the optical electronic transitions between a confined upper and lower state within the active region quantum wells, which had an energy separation such that emission was observed at λ=4.2μm. Electrons would then transition from the lower state to a closely spaced ground-state via non-radiative LO phonon-assisted scattering, before resonantly tunnelling into an adjacent injector region. Population inversion within the active region was enhanced by tailoring the energy spacing of the lower and ground state to be similar to that of the LO phonon energy, ensuring the rate at which the lower electronic states were depopulated was significantly faster than the non-radiative scattering between the two laser levels - ~0.5ps compared to ~4.3ps. The QCL was operational up to a temperature of 88K, with output power approaching 10mW at 10K.

While the performance levels of this groundbreaking device were low by the standards of modern QCLs, the Faist group soon made rapid inroads in the quest for improved performance levels. Only twelve months would pass before continuous wave operation was reported[17], with room-temperature pulsed operation following shortly after[18,19]. Lower device threshold currents and higher output powers were an inevitable consequence of this research drive, as was the milestone that was the realisation of a QCL capable of CW operation at room temperature in 2001[20]. The large interest in

QCLs that this pioneering work inspired means that QCLs can now be designed to operate at a wide range of wavelengths varying from ~3μm at the short-end of the mid-IR[21], up to the far-infrared THz regime[22]. Devices operating in the range $4\mu m \lesssim \lambda \lesssim 5\mu m$ in the mid-IR now routinely achieve room-temperature CW operation at output powers greater than 1W[23-25], while spectroscopic applications are well provided for by lasers that have a broad gain spectrum (in some cases up to $400cm^{-1}$), and whose output can be tuned over a large wavelength range using an external cavity system[26]. Other areas in which QCLs now find an application include non-linear optics[27,28], in which effects such as second harmonic generation can be utilised to further enhance the wavelength range offered by devices.

1.4 Basic Principles of the Quantum Cascade Laser

The core region of a QCL consists of multiple quauntum wells and barriers formed from two semiconductor materials with a differing bandgap - the material with the smaller bandgap constituting the well, and the larger gap material forming the barriers either side. The height of the quantum well is determined by the way in which the two bands align themselves - i.e. the conduction band offset - and varies between material systems, being around 390meV for GaAs/AlGaAs and 520meV for InGaAs/AlInAs[29]. Shown in figure 1.1 is part of the biased conduction band offset for the core region of a GaAs/AlGaAs QCL, encompassing an active region followed by an injection region - which together constitute one core region period - followed by a second active region. A complete QCL core region can be comprised of up to around fifty repeats of these periods.

The active region on the left of the figure is made up of three quantum wells (although active regions featuring four wells are also common), and the moduli squared of the first three confined electronic states associated with these wells at energy levels E_3, E_2 and E_1 are shown in red. Assuming an electron is injected into the upper state E_3 from the preceding injector region, an optical transition can take place between $E_3 \rightarrow E_2$ resulting in the emission of a photon (represented by the green arrow), where the emission wavelength is determined by the energy separation of E_3 and E_2. The electron then quickly scatters to the lower state E_1 where it can tunnel into the injector region. The

states within the injector form a miniband (encompassed by the hatched area in figure 1.1) allowing the electron to traverse this region before tunnelling through the injection barrier and into the upper state E_3 of the next active region, via the injector state E_i. It can be seen that there are no injector region states resonant with the upper level E_3 in the direction of electron travel, and this so-called minigap reduces the probability of the non-radiative escape of electrons from this level. The process of optical transition, followed by injection into the next active region is then repeated over the length of the device core region. In this way, it is possible for a single electron to emit photons at each active region, and thus QCLs tend to have a large optical gain in comparison to conventional semiconductor lasers. This 'recycling' of electrons also leads to large optical output powers - often measured in Watts[30] - as output power is proportional to the number of core region periods within a device.

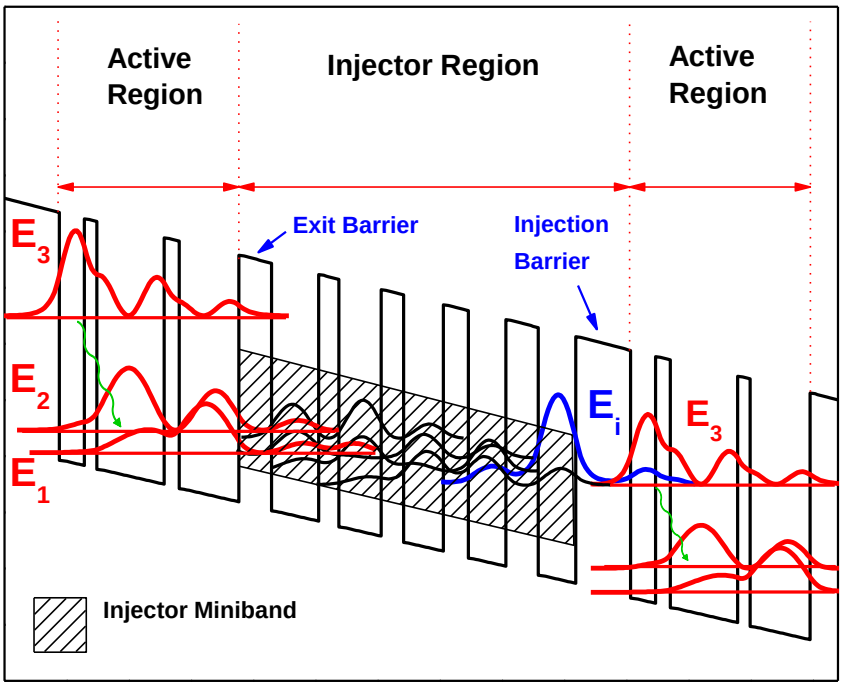

Figure 1.1: Schematic diagram showing a QCL core divided into its constituent active and injection regions. The optical transition between upper and lower laser levels ($E_3 \rightarrow E_2$ in red) is denoted by the green wavy arrow.

Population inversion between the upper and lower states is achieved by ensuring that the electron lifetime in the upper state E_3 is greater than that of the lower states E_2 and E_1. A detailed analysis of QCL scattering times and population inversion is presented in chapter two.

The device emission wavelength can be controlled by adjusting the position of the electronic states within the active region, primarily through variation in the width of the quantum wells and barriers. This is in direct contrast to interband lasers in which the wavelength is determined by the band gap - a property of the material system itself - and means that for a QCL, a wide range of wavelengths can be achieved for a particular material. GaAs QCLs for example, have exhibited emission over wavelengths spanning λ~7μm on the shorter side[31], up to λ>100μm in the case of modern THz devices[22].

1.5 Active Region Design

Three and four-well active regions

The large scope for variation in the sequence of quantum wells and barriers that constitute the core region of a QCL structure has led to a range of differing active region designs. Through systematic adjustment to the number and width of the active region wells and barriers, parameters such as emission wavelength, injection efficiency and electron scattering rates can all be controlled. One of the most common active region configurations currently utilised consists of either three or four quantum wells[32,33], bounded by an injection and exit barrier through which electrons enter and exit the active region respectively (see figure 1.1). As demonstrated by Faist et al, the population inversion attainable between the upper and lower laser levels can be dramatically increased by ensuring the energy spacing between the two (or more) lower levels is approximately equal to that of an LO phonon in the well material - $\hbar\omega_{LO}$~36meV for GaAs - which allows the electron scattering lifetime between these levels to be significantly reduced through resonance with LO phonon emission. Lifetimes of the order of 0.4ps in the case of three-well designs, and 0.25ps for four-well active regions have been demonstrated, in comparison to over 1ps for electron scattering from the upper laser level to lower levels. These short lower level lifetimes aid rapid depopulation of the lower laser level and increase both the overall population inversion within the active region, and the optical gain required for lasing.

A further benefit of the three and four-well active regions is the control they allow over the coupling between the upper laser level and the injector level, which can be enhanced through adjustment to the width of the thin quantum well adjacent to the injection

barrier. This allows electrons to be injected into the active region with increased efficiency, and reduces the probability of direct non-radiative transitions from the injector region to the lower laser levels. As well as controlling electron lifetimes at particular energy levels within the active region, the spatial nature of the optical transition itself can also be engineered. As will be expanded upon in chapter two, the active region can be tailored such that upper state electron wavefunction primarily occupies either the first or second active region quantum well. In the case of the former, transitions will occur between wells and across the well-barrier interface in a so-called diagonal transition, whereas in the latter the transition will be vertical, taking place between confined states within the same quantum well. Whether optical transitions are diagonal or vertical has consequences for the transition probability, upper laser level lifetime and ultimately the population inversion within the active region.

Bound-to-continuum and continuum-to-continuum active regions:

The bound-to-continuum (BTC) active region design[34], shown in figure 1.2, aims to reproduce the good injection efficiency associated with three and four-well active regions, whilst increasing the efficiency with which electrons are typically extracted from the lower laser levels into the injector. In the case of the four-well design, the rate at which electrons resonantly tunnel through the exit barrier from the lowest laser levels into the injector region is around 10 times slower than the rate of electron scattering between the lower levels themselves (1ps compared to 0.1ps respectively). This discrepancy can lead to a reduction in population inversion through the build-up of electrons in the lower levels[29], particularly at higher temperatures where electrons are able to repopulate these levels through thermal backfilling. The BTC active region addresses this issue by replacing the discrete lower levels with a continuum of electronic states similar to that found within the injector of standard QCL active region designs.

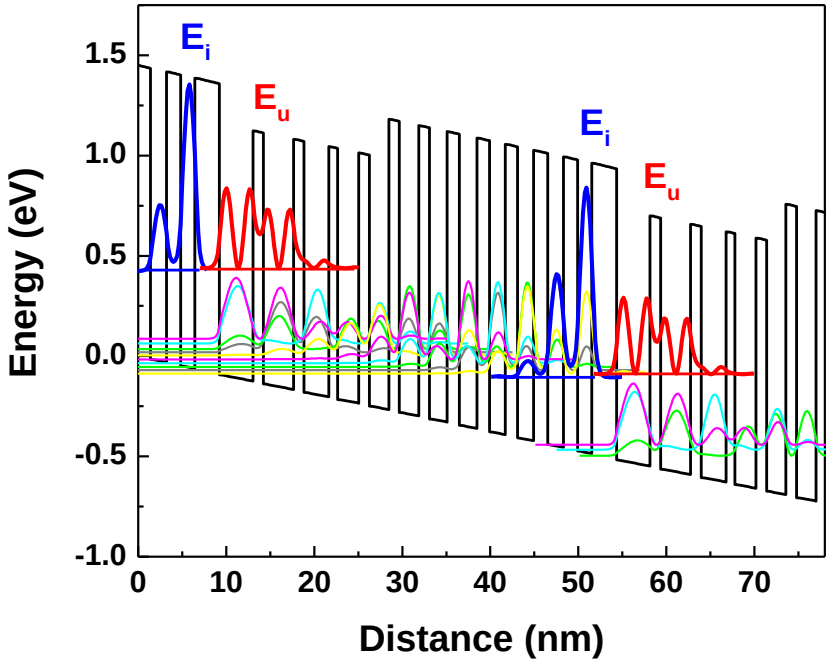

Figure 1.2: QCL Γ-point conduction band profile illustrating the bound-to-continuum active region concept. Optical transitions take place between the upper laser level E_u (shown in red) and a lower continuum of electronic states (multicoloured), before electrons relax along the injector region and are re-injected into the next active region via the state E_i (blue).

This arrangement is achieved by incorporating into the core region a superlattice structure comprising of a series of quantum wells that decrease in width in the direction of electron travel. Rather than the discrete active and injector regions that comprise the core of QCLs featuring three and four-well designs, this structure results in a core with less differentiation between active and injector regions, and a configuration of electronic states in which optical transitions occur between a single discrete upper state, and a lower continuum of states. The advantage of this continuum lies in the fact that electrons scatter through the lower states on a sub-picosecond timescale, avoiding the potential build-up of electrons that can occur in the lower laser levels of the three and four-well designs. Injection efficiency is maintained since electrons continue to be injected from the miniband into the next upper laser level via resonant tunnelling, as is the case with three and four-well active regions.

A further consequence of the BTC design is the broad gain spectrum that arises from the optical transitions between the upper laser level and the large number of states within the lower miniband. This is beneficial for spectroscopic application in which a degree of

wavelength tuning of the laser output is required, for example when analysing gases containing multiple molecule types which would be expected to have several absorption lines at different wavelengths. The gain spectrum can be further widened by extending the concept of the bound to continuum active region to a continuum to continuum design, in which optical transitions are made between an upper and lower continuum, rather than the discrete upper level as for the BTC design. The increase in the number and energy range of states from which optical transitions take place can result in a suitably broadened gain spectrum, with widths of up to 430cm^{-1} being recently reported[35].

1.6 Material Systems for QCL Fabrication: Benefits and Disadvantages of GaAs

To-date, QCL research has primarily focussed on two particular III-V semiconductor compounds as a basis for the fabrication of device structures; namely indium-phosphide (InP) and gallium-arsenide (GaAs). Historically, InP-based devices have attracted a far greater proportion of research, due mainly to the superior device performance that can be achieved when compared to QCLs based on the GaAs material system. It was a QCL featuring an InGaAs/AlInAs active region, grown lattice matched to an InP substrate that first demonstrated lasing in 1994, and since that time the range of materials from which InP-based QCLs have been fabricated has increased to include systems such as InGaAs/AlAsSb[36] and InGaAs/AlAs[37,38]. The first devices developed using the GaAs material system appeared in 1998[39], four years after the emergence of the first InP-based QCLs. Although Page and co-workers reported achievements such as room temperature pulsed operation[40], and low-temperature (150K) continuous wave operation[41] a relatively short time after this, subsequent progress has become somewhat sporadic, with the result being that the CW performance reported by Page et al over a decade ago has yet to be surpassed. The reasons for the lack of progress in relation to GaAs devices can mainly be attributed to its intrinsic material properties, and the kind of performance levels that these properties afford QCLs. For example, the shallow conduction band offset of ΔE_c=0.39eV afforded by GaAs/AlGaAs active regions limits device emission wavelengths to $\lambda \approx 8\mu m$ and above, while also increasing the probability of electron

escape from the upper laser level into the continuum states that exist above the top of the conduction band. This non-radiative escape channel can act to reduce the population inversion between upper and lower laser levels and thus restrict device performance. Also, since the LO phonon-mediated electron scattering lifetime within the QCL active region is essentially inversely proportional to the electron effective mass (m^*)[42], the comparatively large $m^*=0.067m_0$ possessed by GaAs leads to reduced scattering lifetimes in comparison to InP-based devices ($m^*=0.043m_0$ for InGaAs), and thus lower levels of population inversion and gain. A detailed description of the physics of QCL active regions, including a comprehensive analysis of electron lifetimes, scattering rates and population inversion is presented in chapter two.

This seeming inferiority inherent in the material characteristics of GaAs does not necessarily preclude it as a viable QCL material however, and indeed there are certain advantages to utilising this material system over the more commonly used InP. GaAs is one of the most widely studied of all the III-V semiconductor compounds and its production has been successfully implemented on the industrial scale. This has obvious economical benefits for any attempt to mass-produce GaAs-based devices. The fact that $Al_xGa_{1-x}As$ is lattice matched to GaAs for all values of x allows for flexibility in active region design without the need for strain compensation, while also easing the growth constraints for the GaAs/AlGaAs active regions since only the Al source needs to be switched during growth. Nevertheless, the material properties of GaAs can still be regarded as something of a drawback when compared to InP and its associated material systems. One strategy for overcoming these limitations is to focus less on fundamental material properties and more on areas of overall device design in an effort to improve performance. In this respect, a promising area of investigation involves improvements to the QCL waveguide used to confine the optical mode within the device active region. In the case of GaAs-based devices, the waveguide is usually formed using either highly-doped GaAs or high aluminium content $Al_{0.9}Ga_{0.1}As$, both of which have drawbacks associated with their use. In the case of highly-doped GaAs, optical losses can be very high due to free-carrier absorption, while $Al_{0.9}Ga_{0.1}As$ can exhibit poor electrical characteristics. A detailed discussion of the disadvantages of conventional GaAs QCL waveguides is presented in chapter four, while the use of alternative semiconductor materials as QCL waveguides - in an attempt to overcome the limitations of GaAs and AlGaAs, and improve device performance - will form a major part of this thesis.

1. A. A. Kosterev and F. K. Tittel, *Chemical sensors based on quantum cascade lasers*, IEEE Journal of Quantum Electronics, **38**, 582-591, (2002).

2. A. Kosterev, G. Wysocki, Y. Bakhirkin, S. So, R. Lewicki, M. Fraser, F. Tittel and R. F. Curl, *Application of quantum cascade lasers to trace gas analysis*, Applied Physics B-Lasers and Optics, **90**, 165-176, (2008).

3. *Pranalytica [Online]*, Available at: http://www.pranalytica.com/index.php, (2013).

4. *Quantum cascade lasers, mid infrared spectroscopy gas analysers from Cascade Technolgies [Online]*, Available at: http://www.cascade-technologies.com, (2013).

5. *QuantaRed Technologies - Oil in Water Analyzers [Online]*, Available at: http://quantared.com, (2013).

6. R. Maulini, A. Lyakh, A. G. Tsekoun, R. Go, M. Lane, T. Macdonald and C. K. N. Patel, *High power, high efficiency quantum cascade laser systems for directional infrared countermeasures and other defense and security applications*, Proceedings of the SPIE, **7483**, 74830D, (2009).

7. C. Bauer, A. K. Sharma, U. Willer, J. Burgmeier, B. Braunschweig, W. Schade, S. Blaser, L. Hvozdara, A. Müller and G. Holl, *Potentials and limits of mid-infrared laser spectroscopy for the detection of explosives*, Applied Physics B, **92**, 327-333, (2008).

8. J. H. Shorter, D. D. Nelson, J. B. McManus, M. S. Zahniser and D. K. Milton, *Multicomponent Breath Analysis With Infrared Absorption Using Room-Temperature Quantum Cascade Lasers*, IEEE Sensors Journal, **10**, 76-84, (2010).

9. R. F. Kazarinov and R. A. Suris, *Possibility of amplification of electromagnetic waves in a semiconductor with a superlattice*, Soviet Physics: Semiconductors, **5**, 707, (1971).

10. L. C. West and S. J. Eglash, *First observation of an extremely large dipole infrared transition within the conduction band of a GaAs quauntum well*, Applied Physics Letters, **46**, 1156-1158, (1985).

11. M. Helm, P. England, E. Colas, F. Derosa and S. J. Allen, *Intersubband emission from semiconductor superlattices excited by sequential resonant tunneling*, Physical Review Letters, **63**, 74-77, (1989).

12. F. Capasso, K. Mohammed and A. Y. Cho, *Sequential resonant tuneling through a multiquantum well superlattice*, Applied Physics Letters, **48**, 478-480, (1986).

13. P. F. Yuh and K. L. Wang, *Novel infrared band-aligned superlattice laser*, Applied Physics Letters, **51**, 1404-1406, (1987).

14. H. C. Liu, *A novel superlattice infrared source*, Journal of Applied Physics, **63**, 2856-2858, (1988).

15. J. Faist, F. Capasso, D. L. Sivco, C. Sirtori, A. L. Hutchinson and A. Y. Cho, *Quantum Cascade Laser*, Science, **264**, 553-556, (1994).

16. C. Gmachl, F. Capasso, D. L. Sivco and A. Y. Cho, *Recent progress in quantum cascade lasers and applications*, Reports on Progress in Physics, **64**, 1533-1601, (2001).

17. J. Faist, F. Capasso, C. Sirtori, D. L. Sivco, A. L. Hutchinson and A. Y. Cho, *Continuous-wave operation of a vertical transition quantum cascade laser above T=80K*, Applied Physics Letters, **67**, 3057-3059, (1995).

18. J. Faist, F. Capasso, C. Sirtori, D. L. Sivco, A. L. Hutchinson and A. Y. Cho, *Room temperature mid-infrared quantum cascade lasers*, Electronics Letters, **32**, 560-561, (1996).

19. J. Faist, F. Capasso, C. Sirtori, D. L. Sivco, J. N. Baillargeon, A. L. Hutchinson, S. N. G. Chu and A. Y. Cho, *High power mid-infrared (l~5mm) quantum cascade lasers operating above room temperature*, Applied Physics Letters, **68**, 3680-3682, (1996).

20. M. Beck, D. Hofstetter, T. Aellen, J. Faist, U. Oesterle, M. Ilegems, E. Gini and H. Melchior, *Continuous wave operation of a mid-infrared semiconductor laser at room temperature*, Science, **295**, 301-305, (2002).

21. O. Cathabard, R. Teissier, J. Devenson, J. C. Moreno and A. N. Baranov, *Quantum cascade lasers emitting near 2.6mm*, Applied Physics Letters, **96**, 141110, (2010).

22. B. S. Williams, *Terahertz quantum-cascade lasers*, Nature Photonics, **1**, 517-525, (2007).

23. Y. Bai, N. Bandyopadhyay, S. Tsao, E. Selcuk, S. Slivken and M. Razeghi, *Highly temperature insensitive quantum cascade lasers*, Applied Physics Letters, **97**, 251104, (2010).

24. N. Bandyopadhyay, Y. Bai, B. Gokden, A. Myzaferi, S. Tsao, S. Slivken and M. Razeghi, *Watt level performance of quantum cascade lasers in room temperature continuous wave operation at λ~3.76 μm*, Applied Physics Letters, **97**, 131117, (2010).

25. Y. Bai, N. Bandyopadhyay, S. Tsao, S. Slivken and M. Razeghi, *Room temperature quantum cascade lasers with 27% wall plug efficiency*, Applied Physics Letters, **98**, 181102, (2011).

26. A. Hugi, R. Terazzi, Y. Bonetti, A. Wittmann, M. Fischer, M. Beck, J. Faist and E. Gini, *External cavity quantum cascade laser tunable from 7.6 to 11.4mm*, Applied Physics Letters, **95**, 061103, (2009).

27. N. Owschimikow, C. Gmachl, A. Belyanin, V. Kocharovsky, D. L. Sivco, R. Colombelli, F. Capasso and A. Y. Cho, *Resonant second-order nonlinear optical processes in quantum cascade lasers*, Physical Review Letters, **90**, 043902, (2003).

28. C. Gmachl, A. Belyanin, D. L. Sivco, M. L. Peabody, N. Owschimikow, A. M. Sergent, F. Capasso and A. Y. Cho, *Optimized second-harmonic generation in quantum cascade lasers*, IEEE Journal of Quantum Electronics, **39**, 1345-1355, (2003).

29. J. Cockburn, *Mid-infrared quantum cascade lasers*, Mid-Infrared Semiconductor Optoelectronics, 323-355, (Springer, 2006).

30. M. Razeghi, *High-Performance InP-Based Mid-IR Quantum Cascade Lasers*, IEEE Journal of Selected Topics in Quantum Electronics, **15**, 941-951, (2009).

31. L. R. Wilson, J. W. Cockburn, M. J. Steer, D. A. Carder, M. S. Skolnick, M. Hopkinson and G. Hill, *Decreasing the emission wavelength of GaAs-AlGaAs quantum cascade lasers by the incorporation of ultrathin InGaAs layers*, Applied Physics Letters, **78**, 413-415, (2001).

32. C. Sirtori, J. Faist, F. Capasso, D. L. Sivco, A. L. Hutchinson, S. N. G. Chu and A. Y. Cho, *Continuous wave operation of midinfrared (7.4-8.6mm) quantum cascade lasers up to 110 K temperature*, Applied Physics Letters, **68**, 1745-1747, (1996).

33. D. Hofstetter, M. Beck, T. Aellen and J. Faist, *High-temperature operation of distributed feedback quantum-cascade lasers at 5.3μm*, Applied Physics Letters, **78**, 396-398, (2001).

34. J. Faist, M. Beck, T. Aellen and E. Gini, *Quantum-cascade lasers based on a bound-to-continuum transition*, Applied Physics Letters, **78**, 147-149, (2001).

35. Y. Yao, X. J. Wang, J. Y. Fan and C. F. Gmachl, *High performance "continuum-to-continuum" quantum cascade lasers with a broad gain bandwidth of over 400 cm^{-1}*, Applied Physics Letters, **97**, 081115, (2010).

36. D. G. Revin, L. R. Wilson, E. A. Zibik, R. P. Green, J. W. Cockburn, M. J. Steer, R. J. Airey and M. Hopkinson, *InGaAs/AlAsSb quantum cascade lasers*, Applied Physics Letters, **85**, 3992-3994, (2004).

37. K. Ohtani and H. Ohno, *An InAs-based intersubband quantum cascade laser*, Japanese Journal of Applied Physics Part 2-Letters, **41**, L1279-L1280, (2002).

38. M. P. Semtsiv, M. Ziegler, S. Dressler, W. T. Masselink, N. Georgiev, T. Dekorsy and M. Helm, *Above room temperature operation of short wavelength (l=3.8mm) strain-compensated $In_{0.73}Ga_{0.27}As$-AlAs quantum-cascade lasers*, Applied Physics Letters, **85**, 1478-1480, (2004).

39. C. Sirtori, P. Kruck, S. Barbieri, P. Collot, J. Nagle, M. Beck, J. Faist and U. Oesterle, *GaAs/$Al_xGa_{1-x}As$ quantum cascade lasers*, Applied Physics Letters, **73**, 3486-3488, (1998).

40. H. Page, C. Becker, A. Robertson, G. Glastre, V. Ortiz and C. Sirtori, *300 K operation of a GaAs-based quantum-cascade laser at l ~ 9mm*, Applied Physics Letters, **78**, 3529-3531, (2001).

41. H. Page, S. Dhillon, M. Calligaro, C. Becker, V. Ortiz and C. Sirtori, *Improved CW operation of GaAs-Based QC lasers: T-max=150 K*, IEEE Journal of Quantum Electronics, **40**, 665-672, (2004).

42. J. Faist, F. Capasso, C. Sirtori, D. L. Sivco and A. Y. Cho, *Quantum Cascade Lasers*, Intersubband Transitions in Quantum Wells: Physics and Device Applications II, (Academic Press, 1999).

Chapter Two

Quantum Cascade Lasers: Theory and Principles of Operation

2.1 Introduction

The following sections present an overview of some of the basic theoretical concepts that are fundamental to the operation of the quantum cascade laser. As well as a mathematical treatment, the properties that can be derived from these concepts will be examined in relation to their effect on laser design. Firstly, the nature of photon generation within the laser active region will be discussed, in the context of the quantum mechanics of intersubband transitions - in particular the spontaneous transition of electrons between subbands. The intersubband gain will then be reviewed. By considering a simplified model of electronic transitions based upon a three-level system within the active region, rate equations will be used to derive several operating parameters of the QCL such as the population inversion between electron energy levels and the laser threshold current density. The chapter ends with a discussion of the methods used to model the confinement of the optical mode within the laser active region, necessary when evaluating the effectiveness of a particular waveguide design to be used within the laser structure.

2.2 Intersubband Transitions

The analysis of electronic transitions between the subbands of a semiconductor heterostructure begins by applying Fermi's golden rule, which describes the electron transition rate W_{if}, from an initial state i, to a final state f due to perturbation from an external electromagnetic field[1]:

$$W_{if} = \frac{2\pi}{\hbar}\left|\langle\psi_i|H'|\psi_f\rangle\right|^2\delta\left(E_f - E_i - \hbar\omega\right) \tag{2.1}$$

where ψ_i and ψ_f represent the initial and final electronic wavefunctions respectively, H' is the interaction Hamiltonian and $\delta(E_f - E_i - \hbar\omega)$ is the density of final states of the system. In the case of the external field being a linearly polarized plane wave, and provided its wavelength is greater than the scale over which electrons traverse the QCL active region, it can be shown that the transition rate is proportional to the square of the transition dipole matrix element, $z_{ij}=\langle\psi_i|\boldsymbol{e}\cdot\boldsymbol{p}|\psi_f\rangle$[1]:

$$W_{if} = \frac{2\pi}{\hbar}\frac{e^2E_0^2}{4m^{*2}\omega^2}\left|\langle\psi_i|\boldsymbol{e}\cdot\boldsymbol{p}|\psi_f\rangle\right|^2\delta\left(E_f - E_i - \hbar\omega\right) \tag{2.2}$$

where $\boldsymbol{e}$ is the polarisation vector of the electric field, $\boldsymbol{p}$ is the linear momentum operator, e the electronic charge, m^* the electron effective mass, E_0 the amplitude of the electric field, and ω the angular frequency of the EM radiation. The dipole matrix element can be tailored during the design of the active region by specifying the quantum wells in which the electronic wavefunctions associated with the laser transition have their maximum probability densities. Transitions that occur between states within the same quantum well (vertical transitions) have larger dipole moments that those that occur between adjacent wells (diagonal transitions), are therefore more probable and have a correspondingly higher transition rate.

Within the QCL active region there are several mechanisms by which an electron occupying the upper laser level can undergo a transition to a lower energy level, including non-radiative processes such as phonon and electron-electron scattering. It is the spontaneous radiative transition of electrons between subbands however, and the resultant emission of photons that provide the basis for further stimulated emission, gain and ultimately lasing. It can be shown that following on from equation 2.1, the spontaneous emission rate of photons W_{if}^{sp}, is given by[2]:

$$W_{if}^{sp} = \frac{e^2 n_{ref} z_{ij}^2 E_{ij}^3}{3\pi c^3 \varepsilon_0 \hbar^4} \tag{2.3}$$

where z_{ij} is the transition dipole matrix element, n_{ref} is the refractive index of the laser medium, c is the speed of light in a vacuum, ε_0 is the permittivity of free space and E_{ij} the energy of the transition; i.e. E_i-E_j. As well as demonstrating the same quadratic dependence on dipole matrix element seen in equation 2.2, it can be seen that the spontaneous radiative transition rate is also related to the emission wavelength, manifested in the energy term E_{ij}. This wavelength dependence is also quadratic if the transition rate is expressed as a product of the transition energy and the transition oscillator strength, and results in increasing transition lifetimes at longer wavelengths. For QCLs emitting in the mid-infrared, these lifetimes can be several orders of magnitude longer than some non-radiative processes such as LO phonon scattering which occur on a picosecond time scale[3], and lead to the low spontaneous radiative efficiencies observed for QCLs.

2.3 Intersubband Gain

As with any type of laser, the amount by which optical emission can be amplified within the laser medium - the gain - is a key indicator of QCL performance. The previous section detailed the emission of photons due to the spontaneous transition of electrons between two subbands of the conduction band. In order to achieve lasing however, it is necessary for these spontaneously emitted photons to themselves interact with electrons

in the upper laser level, triggering further electronic transitions to the lower level. The subsequent stimulated emission of photons that occurs as a result of these interactions leads to an increase in the photon density within the laser medium, and thus optical gain. For a QCL, the peak material gain G_p, that can be achieved between two subbands i and j is given by[4]:

$$G_p = \frac{4\pi e^2}{\varepsilon_0 n_{ref} \lambda} \frac{z_{ij}^2}{2\gamma_{ij} L_p} (n_j - n_i) \tag{2.4}$$

where n_{ref} is the refractive index associated with the laser mode, λ the emission wavelength, $2\gamma_{ij}$ the spontaneous emission full width at half-maximum, determined from electroluminescence measurements and n_j-n_i is the difference in electron sheet densities between subbands i and j. The term L_p contained in the denominator is a normalisation factor - normally taken to be the length of a single active region period. The terms on the right-hand side of equation 2.4 are commonly collected together and termed the gain cross-section, g_c - i.e. the peak modal gain per unit of upper state population:

$$g_c = \Gamma \frac{4\pi e^2}{\varepsilon_0 n_{ref} \lambda} \frac{z_{ij}^2}{2\gamma_{ij} L_p} \tag{2.5}$$

where Γ is the confinement factor of the optical mode, i.e. the fraction of the optical mode that is confined within the active region section of the complete QCL structure. The dependence of the gain on electronic population inversion will be expanded upon within the discussion of QCL rate equations in section 2.4. In terms of the relationship between the gain and the transition dipole matrix element z_{ij}, equation 2.4 shows that once more a quadratic dependence is predicted. It has been discussed above how it is possible to tailor the dipole matrix through the confinement of the electron wavefunctions within specific quantum wells of the active region; however, the dependence of gain on the optical dipole also influences the choice of material system to be used for device fabrication.

The energies of the quantised levels within a quantum well are inversely proportional to both the particle mass (or effective mass m^*, in the case of electrons in a semiconductor), and the square of the well width. Since the effective electron mass for GaAs is $m^*=0.067m_0$ - larger than, for example, InGaAs ($m^*=0.043m_0$) - for an equivalent energy separation GaAs-based QCLs require narrower quantum wells in the active region than their InP-based counterparts. The reduction in well width however, brings with it a concomitant decrease in dipole matrix element and gain, and as such represents one of the fundamental disadvantages of the GaAs/AlGaAs material system compared to InGaAs/AlInAs/InP.

2.4 QCL Rate Equations

Several important parameters that characterise the operation of a QCL can be derived through an analysis of a simplified, sub-threshold three-level active region, and the electronic transitions associated with it. By considering the rates at which these transitions occur, it is possible to determine the conditions for population inversion - essential for the operation of any laser - as well as an expression for the threshold current density. Shown in figure 2.1 is a schematic representation of a sub-threshold three-level active region, and the various current paths and electronic transitions possible within. From the perspective of maximising the population inversion between the upper and lower energy levels (E_3 and E_2 respectively), it is obviously desirable that the current injected into the active region from the preceding injector level - shown as the current density J_3 for dimensional consistency - populates E_3 with 100% efficiency. There is however the possibility of a parasitic current path J_2, from the injector level directly to E_2 which will act to reduce the population inversion.

Once electrons have been injected into the active region several possible transitions can then occur, each with an associated transition rate τ^{-1}, where τ is the lifetime for which an electron will remain at a particular energy level. For electrons that have been injected directly into level E_3, a transition can occur between E_3 and E_2 (which would be an optical transition above threshold) at a rate τ_{32}^{-1}. This can then be followed by a transition from E_2 to E_1 at a rate τ_{21}^{-1}, before electrons exit the active region via resonant tunnelling from E_1 to the adjacent injector level, again with associated rate τ_{1i}^{-1}. In

addition to this pathway, there also exist several other non-radiative transitions available to electrons which reduce the overall efficiency of the active region. For electrons occupying level E_3, rather than making the transition $E_3 \rightarrow E_2$, it is possible to transition directly to the lowest energy level E_1 (at rate τ_{31}^{-1}), or to escape directly into the continuum states above the injector miniband (at rate τ_{esc}^{-1}). For those electrons that have made the transition from $E_3 \rightarrow E_2$, escape directly from E_2 is also possible - signified by τ_{2i}^{-1}.

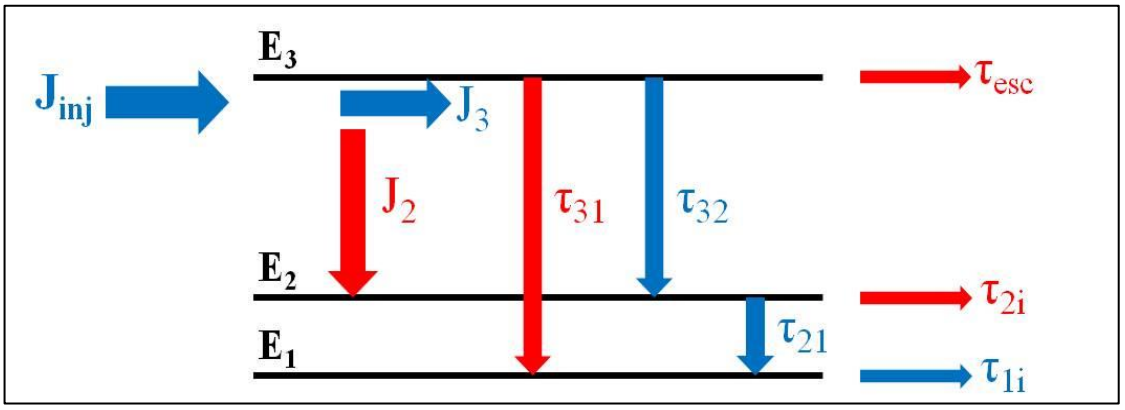

Figure 2.1: Schematic diagram illustrating a simplified three-level QCL active region, and the various electron pathways that exist within. This scheme forms the basis from which the rate equations presented in section 2.4.1 are derived.

2.4.1 Population Inversion

Derivation of the conditions for population inversion begins with a consideration of the relative sub-threshold electron sheet densities n_3 and n_2 (in cm^{-2}) of levels E_3 and E_2 respectively, and the rate at which electrons depopulate these levels via the mechanisms described above. With reference to figure 2.1 it can be seen that the rate of change dn/dt, of the population n_3 is given by the expression:

$$\frac{dn_3}{dt} = \frac{J_3}{e} - \frac{n_3}{\tau_{32}} - \frac{n_3}{\tau_{31}} - \frac{n_3}{\tau_{esc}} \tag{2.6}$$

and similarly for n_2:

$$\frac{dn_2}{dt} = \frac{J_2}{e} + \frac{n_3}{\tau_{32}} - \frac{n_2}{\tau_{21}} - \frac{n_2}{\tau_{2i}} \tag{2.7}$$

with all terms as previously defined. Below threshold it is assumed that the system is in the steady state, i.e:

$$\frac{dn_3}{dt} = \frac{dn_2}{dt} = 0 \tag{2.8}$$

By setting equations 2.6 and 2.7 equal to zero it can be shown that:

$$n_3 = \frac{\mathrm{J}_3}{\mathrm{e}}\left(\frac{1}{\tau_{32}} + \frac{1}{\tau_{31}} + \frac{1}{\tau_{esc}}\right)^{-1} \tag{2.9}$$

and

$$\frac{n_2}{n_3} = \frac{\mathrm{J}_2}{en_3}\left(\frac{1}{\tau_{21}} + \frac{1}{\tau_{2i}}\right)^{-1} + \frac{1}{\tau_{32}}\left(\frac{1}{\tau_{21}} + \frac{1}{\tau_{2i}}\right)^{-1} \tag{2.10}$$

By substituting equation 2.9 into equation 2.10 and assuming that the current that is injected into E_3 is very much greater than E_2 (i.e. that $J_2/J_3 \rightarrow 0$) we arrive at:

$$\frac{n_2}{n_3} \approx \frac{1}{\tau_{32}}\left(\frac{1}{\tau_{21}} + \frac{1}{\tau_{2i}}\right)^{-1} \tag{2.11}$$

The electron lifetimes τ_{21} and τ_{2i} (representing transitions from $E_2 \rightarrow E_1$ and from E_2 to the injector respectively) can be combined into a single lifetime τ_2, representing the total time for which electrons populate E_2.

We therefore now have the condition that the ratio of the electron populations n_3 and n_2 is directly proportional to the ratio of the lifetimes between the transition $E_3 \rightarrow E_2$ and that of level E_2, i.e:

$$\frac{n_3}{n_2} \approx \frac{\tau_{32}}{\tau_2} \tag{2.12}$$

Thus, as one would expect, in order to achieve a population inversion (i.e. $n_3/n_2 > 1$) we require that the transition lifetime τ_{32} is greater than the lifetime τ_2 for which electrons occupy level E_2.

The population difference $\Delta n = n_3 - n_2$, between level E_3 and E_2 can be calculated by following a similar exercise to that shown above. Starting with equations 2.6 and 2.7 and the steady state condition that $dn/dt = 0$, and assuming that both the rate of electron escape from E_3 directly into the continuum and the current injected directly into E_2 are very small (i.e. $1/\tau_{esc}$ and $J_2 \approx 0$), we arrive at expressions for the populations n_3 and n_2:

$$n_3 = \frac{J_3}{e}\tau_3 \qquad \text{and} \qquad n_2\left(\frac{\tau_{32}}{\tau_2}\right) = n_3 \tag{2.13a and 2.13b}$$

The population difference $n_3 - n_2$ can be expressed using equation 2.13b:

$$n_3 - n_2 = n_2\left(\frac{\tau_{32}}{\tau_2} - 1\right) \tag{2.14}$$

Combining equations 2.13a and 2.13b leads to:

$$n_2 = \frac{\tau_2}{\tau_{32}} \frac{\mathrm{J}_3}{\mathrm{e}} \tau_3 \tag{2.15}$$

which when combined with equation 2.14 results in a final expression for Δn:

$$\Delta n = \frac{J_3}{e} \tau_3 \left(1 - \frac{\tau_2}{\tau_{32}}\right) \tag{2.16}$$

In the same way that achieving population inversion requires a longer upper state lifetime in relation to the E_2 lifetime, it is seen that in order to subsequently maximise the difference between upper and lower level populations, the difference between these lifetimes must also be maximised. As is indicated by equation 2.4, any increase in the ratio τ_{32}/τ_2 will also have the corresponding effect of increasing the QCL gain, which is directly proportional to the population difference between E_3 and E_2. Increasing the upper state lifetime can be achieved in a similar manner to that previously described for the dipole matrix element, namely by tailoring the spatial position of the electronic wavefunctions to make transitions more or less probable.

It is generally found however that a reduction of the wavefunction overlap designed to increase the upper state lifetime, is accompanied by a reduction in the transition dipole matrix element on which QCL gain is also dependent. Thus a balance must be struck between these two factors when considering the amount of gain that may be achievable for any particular QCL design.

2.4.2 Threshold Current Density

A slightly modified set of arguments to those presented above may be used to derive an expression for the QCL threshold current density J_{th}. In this instance, a term describing the rate at which electrons re-occupy E_2 through thermal backfilling, n_2^{therm} is added to

the previous rate equation 2.7, while the electrons injected into the active region are assumed to occupy E_3 with 100% efficiency (i.e. J_2=0) giving:

$$\frac{dn_3}{dt} = \frac{J}{e} - \frac{n_3}{\tau_3} \tag{2.17}$$

and

$$\frac{dn_2}{dt} = \frac{n_3}{\tau_{32}} - \frac{\left(n_2 - n_2^{therm}\right)}{\tau_2} \tag{2.18}$$

where τ_3^{-1} and τ_2^{-1} represent the total scattering rates from E_3 and E_2 respectively. By again considering the steady state conditions below threshold ($dn_3/dt=dn_2/dt$=0), we arrive at:

$$n_3 = \frac{J\tau_3}{e} \quad \text{and} \quad n_2 = n_3\frac{\tau_2}{\tau_{32}} + n_2^{therm} \tag{2.19a and 2.19b}$$

which can be combined to give the population difference $\Delta n=n_3-n_2$ between E_3 and E_2:

$$\Delta n = \frac{J\tau_{eff}}{e} - n_2^{therm} \tag{2.20}$$

where the total electron effective lifetime τ_{eff} is defined as $\tau_{eff} =\tau_3(1-\tau_2/\tau_{32})$. Threshold current density is reached when the modal gain equals the total loss from the laser cavity i.e.:

$$G_{Mod} = \Gamma G_P = \alpha_{tot} \tag{2.21}$$

Substituting for G_p from equations 2.4 and 2.5 leads to:

$$g_c \Delta n = \alpha_{tot} \tag{2.22}$$

from which we arrive at:

$$g_c \left(\frac{J\tau_{eff}}{e} - n_2^{therm} \right) = \alpha_{tot} \tag{2.23}$$

Finally, rearranging for J gives the expression for the threshold current density:

$$J_{th} = e \frac{(\alpha_{tot}/g_c + n_2^{therm})}{\tau_{eff}} \tag{2.24}$$

The importance of a large upper state lifetime in comparison to the lifetimes of the lower laser levels is again apparent from equation 2.24, since for $\tau_{32} \gg \tau_2$, $\tau_{eff} \rightarrow \tau_3$ leading to lower threshold currents for larger τ_{32}/τ_2 ratios (and correspondingly larger population inversions). In addition to this, it is seen that the losses within the device must also be minimised in order to achieve smaller threshold currents. Since the total losses α_{tot} can be separated into those relating to the mirrors at each end of the laser cavity α_m, and the waveguide losses α_w (i.e. $\alpha_{tot}=\alpha_m+ \alpha_w$), it therefore follows that any reduction in waveguide loss that can be achieved should result in a lowering of the device threshold current density. Attempts to reduce α_w through the use of material systems not previously considered for incorporation in QCL waveguides will be one focus of the experimental chapters of this thesis.

2.4.3 Slope Efficiency

In order to derive the QCL slope efficiency *dP/dI*, the above-threshold dynamics of the active region must be considered, whereby the gain becomes fixed and the photon flux *S*, within the active region increases linearly with current density[2]. Modified forms of

the QCL rate equations, which now include a term for the photon flux *S*, per period, per unit active region width are given by:

$$\frac{dn_3}{dt} = \frac{J}{e} - \frac{n_3}{\tau_3} - Sg_c(n_3 - n_2) \tag{2.25}$$

and

$$\frac{dn_2}{dt} = \frac{n_3}{\tau_{32}} + Sg_c(n_3 - n_2) - \frac{n_2 - n_2^{therm}}{\tau_2} \tag{2.26}$$

An expression for the rate of change of *S* with current density can obtained by considering the situation at threshold where the optical gain becomes fixed, and is equal to the total optical loss i.e. $g_c\Delta n = \alpha_{tot.}$ By setting the derivatives in equations 2.25 and 2.26 to zero and substituting for $g_c\Delta n$, we arrive, at some length, at an expression for *dS/dJ*:

$$\frac{dS}{dJ} = \frac{\tau_{eff}}{e\alpha_{tot}(\tau_2 + \tau_{eff})} \tag{2.27}$$

where α_{tot} is the total loss from the laser cavity and τ_{eff} is as previously defined in equation 2.20. The slope efficiency is then found using the derivative of the photon flux:

$$\frac{dP}{dI} = N_p\hbar\omega\alpha_m\frac{dS}{dJ} \tag{2.28}$$

where N_p is the number of core region periods within the QCL structure and α_m the cavity mirror loss.

The slope efficiency can therefore be expressed as:

$$\frac{dP}{dI} = \frac{N_p \hbar \omega}{e} \frac{\alpha_m}{\alpha_{tot}} \frac{\tau_{eff}}{\tau_{eff} + \tau_2} \tag{2.29}$$

2.5 QCL Waveguides

In order to maximise the rate of stimulated emission of photons within the laser core, and to prevent unwanted losses to the QCL layers that surround it, a method of confining the optical mode within the QCL active region is needed. The most common approach is to form a dielectric slab waveguide by surrounding the core with two layers of semiconductor material that both posses a smaller refractive index than that of the active region. The refractive index contrast acts to limit the optical mode penetration from core to outer layers in the growth direction, while lateral confinement is provided by the walls of the ridge structure itself.

The confinement of the optical mode within the QCL structure can be modelled once various parameters relating to the materials to be used in the structure are known. It is generally necessary to first calculate the real and imaginary parts of the complex dielectric constant for each material layer. These two parameters - ε_1 and ε_2 respectively - are given by[5]:

$$\varepsilon_1 = \varepsilon_\infty - \frac{e^2}{\varepsilon_0 m^* \omega^2} N \tag{2.30}$$

and

$$\varepsilon_2 = \frac{e^2}{\varepsilon_0 m^* \omega^2} \frac{N}{\omega \tau} \tag{2.31}$$

where ε_∞ is the high-frequency dielectric constant, e is the electronic charge, N is the doping concentration per unit volume, ε_0 the permittivity of free space, m^* the electron effective mass, ω the angular frequency of emitted radiation and τ the electron scattering time. The quantities ε_∞, ε_0, m^* and τ for each material can be found in the relevant literature, allowing ε_1 and ε_2 to be calculated and subsequently used to determine the real and imaginary parts of the refractive index (n and k respectively) for each layer[6]:

$$n = \left[\frac{(\varepsilon_1^2 + \varepsilon_2^2)^{\frac{1}{2}}}{2} + \frac{\varepsilon_1}{2}\right]^{\frac{1}{2}} \tag{2.32}$$

and

$$k = \left[\frac{(\varepsilon_1^2 + \varepsilon_2^2)^{\frac{1}{2}}}{2} - \frac{\varepsilon_1}{2}\right]^{\frac{1}{2}} \tag{2.33}$$

Equations 2.30 through 2.33 enable the complex refractive index to be modelled as a function of doping concentration N, and thus N can be chosen such that it results in a desired value of n and k for each layer of the QCL structure. Once the parameters n, k and ε_0 are known for each layer, the optical mode profile for the complete structure can be simulated using specialist software. Since the dipole transitions that result in QCL emission take place in the plane of the direction of growth (conventionally taken as the z-direction), emission is in the x-y plane - i.e. edge-emitting - and is transverse-magnetic (TM) polarised. Optical mode profiles are therefore calculated for the TM rather than transverse electric (TE) mode. Of particular relevance to waveguide design is the mode confinement factor Γ, defined previously in equation 2.5, which can be calculated by integrating the profile over each separate layer (see appendix A.2). The waveguide losses α_w, can also be calculated in a similar manner. Several examples of optical mode profiles determined using this method are presented in chapter four, in figures 4.1 through 4.4.

1. M. Helm, *The Basic Physics of Intersubband Transitions*, Intersubband Transitions in Quantum Wells: Physics and Device Applications I, (Academic Press, 1999).

2. J. Faist, *Quantum Cascade Lasers*, (OUP, 2013).

3. R. Ferreira and G. Bastard, *Evaluation of some scattering times for electrons in unbiased and biased single- and multiple-quantum-well structures*, Physical Review B, **40**, 1074-1086, (1989).

4. J. Faist, F. Capasso, C. Sirtori, D. L. Sivco and A. Y. Cho, *Quantum Cascade Lasers*, Intersubband Transitions in Quantum Wells: Physics and Device Applications II, (Academic Press, 1999).

5. F. Capasso, A. Y. Cho, J. Faist, A. L. Hutchinson, C. Sirtori and D. L. Sivco, *Article Comprising a Semiconductor Waveguide Structure*, United States Patent 5502787, (1996).

6. A. M. Fox, *Optical Properties of Solids*, (OUP, 2001).

Chapter Three

Semiconductor Growth and Device Fabrication and Characterisation

3.1 Introduction

The transformation of a wafer of semiconductor material into a working QCL device, and the testing and measurement required to determine its optical and electrical characteristics involves numerous processes, many of which must be carried out in highly regulated clean-room environments. The chapter begins with a discussion of the epitaxy used to grow the semiconductor wafer structure from which lasers are subsequently fabricated, before describing details of the growth as it relates specifically to the GaAs-based wafers used in this work. The various lithographic, etching and bonding processes involved in the fabrication of the devices featured in the experimental chapters of this thesis are then considered, before ending with a presentation of the techniques employed to characterise devices such as Fourier Transform Infra-red Spectroscopy, current-voltage and current-power measurements, and determination of waveguide losses and characteristic temperature.

3.2 Metal-Organic Vapour Phase Epitaxy

Due to the nature of the QCL structure, a growth technique is required that on the one hand allows precise control of the nanometre-scale repeating layers of the active region, whilst on the other allows the rapid growth of the surrounding micron-thick cladding layers. The ability to grow a wide range of semiconductor materials to accommodate differing QCL designs is also required. In this respect, metal-organic vapour phase epitaxy (MOVPE) is an ideal choice for QCL growth, and all wafers presented in this thesis were grown using MOVPE at the National Centre for III-V Technologies in Sheffield[1].

In contrast to methods such as molecular beam epitaxy (MBE) which use solid sources as the basis for material deposition, MOVPE utilises gasses flowing over a heated substrate and the subsequent reactions that occur at the substrate surface to build up layers of semiconductor. In the general case of III-V semiconductors, metalorganic compounds of the group III elements are combined with hydrides of group V to produce the desired alloy[2]:

$$A^{III}R_3 + B^V X_3 \rightarrow A^{III}B^V + organic\ compounds \tag{3.1}$$

The particular gasses used are dependent on the material being grown; for example in the case of GaAs, a combination of trimethylgallium ($Ga(CH_3)_3$) and arsine (AsH_3) can be used to form GaAs plus various organic waste compounds. These so-called precursor gasses are transported via a carrier gas, usually hydrogen (H_2), into the main reaction chamber which can be held at a pressure between 150 and 750 Torr (atmospheric pressure). The precursor gasses diffuse toward the heated (typically between 500-800°C) substrate, whereby they decompose into their constituent components and the III-V atoms are adsorbed onto its surface at an appropriate point on the crystal lattice. The organic molecules are desorbed from the surface and diffuse away from the substrate before being carried out of the chamber as waste gasses[3]. Gasses can be switched during growth to allow the formation of different materials and thus the complete QCL wafer can be grown sequentially.

QCL growth by MOVPE offers a number of advantages over MBE. As already touched upon, growth rates of up to 5µm/hr are achievable compared to around 0.5µm/hr for MBE, making MOVPE particularly suitable for growth of the thick semiconductor layers that surround the QCL active region. The fact that an ultra-high vacuum is not required during growth also leads to less machine downtime in between growth runs and during maintenance. These factors combine to make MOVPE a more financially economical technique in comparison to MBE, especially when producing wafers on an industrial scale. One further benefit of MOVPE is its ability to grow materials from the phosphide group - for example InP - using the precursor gas phosphine (PH_3). Growth of phosphides using MBE is more problematic due to the unstable and potentially dangerous nature of solid-source phosphorus.

For the production of the QCL wafers presented in this work, a horizontal flow, low-pressure (150 Torr) MOVPE system was used, with growth taking place at 690°C to produce a series of 2" wafers in each growth run.

3.3 Device Fabrication

Due to the smaller, non-industrial scale of device production within the laboratory environment it is unusual to work with a complete 2" wafer in a single processing run. Wafers are therefore hand-cleaved at right-angles to the major and minor-flat (ensuring breaks are straight and clean), into smaller sections - generally between 1/4 and 1/8 of the original wafer area - before processing commences. The cleaved wafer section must then be cleaned to ensure that, along with any other particulate contaminants, no material fragments that may have been produced as a result of the cleaving process are present on the wafer surface. A three-stage clean using the solvents n-butyl acetate, acetone and isopropyl alcohol is used for this purpose. Despite processing taking place in ISO 6 and ISO 5 category clean rooms (which allow for no more than 8320 and 832 particles greater than 1µm in size per cubic metre respectively[4]), contaminants remain present during most stages of fabrication and so this cleaning process is repeated several times over the course of a processing run in order to maximise final device yield.

Figure 3.1 below shows the main processing steps involved in the fabrication of QCL devices once the wafer has been sufficiently cleaned. Firstly, a 500nm layer of silicon dioxide (SiO_2) is deposited over the surface of the wafer using plasma-enhanced chemical vapour deposition (PECVD), which forms the basis of the hard mask used to define the laser ridges during the subsequent dry-etching of the wafer. To this dielectric layer is added ~1µm of photoresist (SPR350 positive resist) deposited by spin-coating, which allows the transfer of the laser ridge pattern to the hard mask. The wafer is then placed in a mask-aligner (Karl Suss UV300) and positioned underneath a chrome-plated quartz mask patterned with the ridge structure. Due to the 10° miscut of the wafer substrate, the sample must be aligned such that the edges formed by the major-flat cleave are parallel to the laser ridges defined on the mask. This ensures that once cleaved, the laser facets are both vertical with respect to the top and bottom of the laser, and perpendicular to the side walls of the laser ridge. The sample is illuminated by ultra-violet light for approximately 10s, whereby areas of photoresist not shadowed by the chrome of the mask are exposed to the radiation and those that lie directly underneath the chrome remain unexposed.

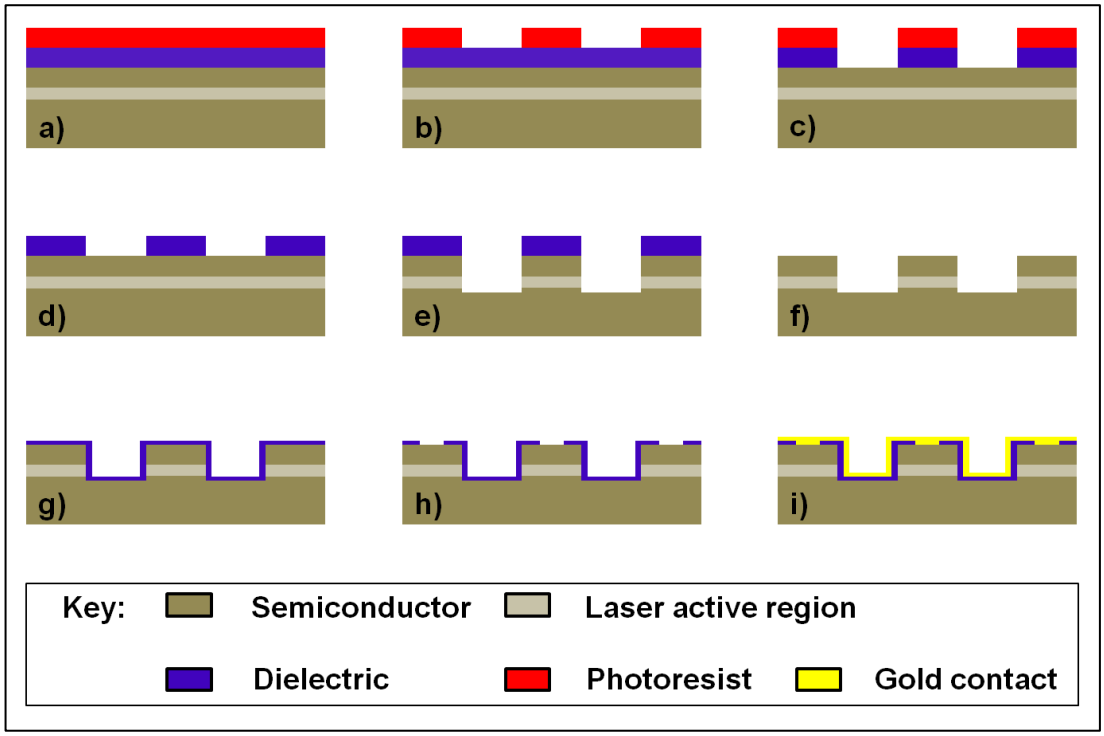

Figure 3.1: Key processing steps for the fabrication of QCL devices. (a) Hard mask and resist deposition. (b) Ridge photolithography. (c) Hard mask ICP etch. (d) Resist removal. (e) Semiconductor ICP etch. (f) Hard mask removal. (g) Dielectric deposition. (h) Contact window etch. (i) Gold contact deposition.

Following exposure, samples are immersed in a chemical developer (Microposit MF26A). UV exposure causes the formation of an acidic compound within the resist which renders it soluble in the alkaline developer, and thus exposed photoresist is dissolved and removed from the sample while unexposed resist remains on the sample surface[5]. In this way, the laser ridge pattern defined by the mask is imprinted in the photoresist forming a three-dimensional series of resist stripes. This pattern is then transferred to the SiO_2 layer underneath by inductively-coupled plasma (ICP) etching. In order to ensure that the resist layer is not removed before the SiO_2 etch is completed, the gasses used during the process must preferentially etch the SiO_2 at a faster rate than the resist. A combination of argon (Ar) and trifluoromethane (CHF_3) is used to etch through the areas of SiO_2 not covered by resist, down to the underlying semiconductor surface. Upon completion of the SiO_2 etch, a specialised solvent (Microposit 1165) is used to remove the remaining photoresist, followed by a secondary three-solvent clean, to leave the wafer covered only by the SiO_2 hard mask which is a copy of the original resist pattern.

In order to form laser ridges in the semiconductor itself, a second ICP etch is performed which selectively etches the semiconductor material over the SiO_2 of the hard mask. Different combinations of gasses can be used depending upon the particular material being etched. In the case of the GaAs-based wafers presented in the experimental section of this thesis, a mixture of silicon tetrachloride ($SiCl_4$) and argon were used for devices containing InGaP waveguides, while a two-stage process utilising $SiCl_4$ to etch the top GaAs layer followed by $SiCl_4$/Ar for the remaining structure was used for InAlP-containing wafers. In order to monitor the etch depth and ensure that the sample is not under or over-etched, the intensity of reflected light from λ=960nm laser incident on the sample surface is measured in-situ during the process and compared to a calculated model. After etching to the desired depth - usually just below the active region layer - the remaining SiO_2 is removed with the same CHF_3/Ar etch used in the formation of the hard mask to leave a sample that comprises of a series of parallel semiconductor ridges. These ridges then form the basis for the final QCL devices (see figure 3.2).

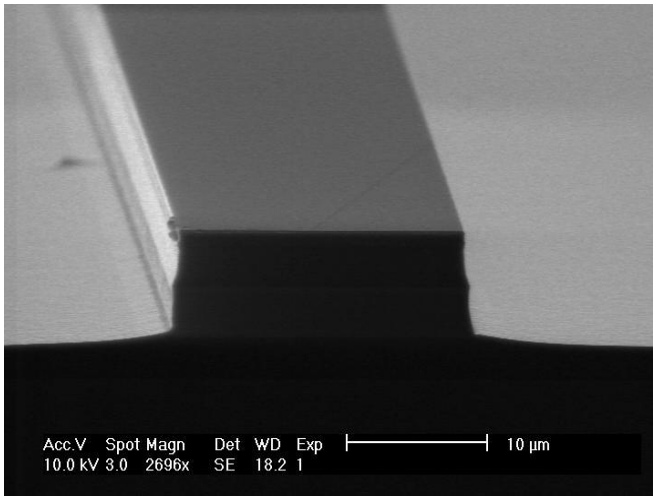

Figure 3.2: Scanning electron microscope image of an ICP etched QCL ridge. The GaAs/AlGaAs active region can be seen as the lighter coloured band in between the darker InGaP waveguide layers either side.

Electrical isolation of the semiconductor ridges is provided by a 500nm thick layer of insulating silicon nitride (Si_3N_4) deposited over the entire wafer by PECVD. Contact windows are then formed along the entire length of the laser ridges by etching through the central section of Si_3N_4 covering the top of the ridges to the semiconductor below, in order to provide a channel for electrical current once the metallic contacts have been added. The process of creating the contact windows follows the same lithography and ICP etch procedure as for the formation of the laser ridges described above, with the exception that alignment of the sample to the mask pattern is now achieved using micron-scale alignment keys on both wafer and mask. This ensures that the contact windows do not drift toward the edge of the ridges as they follow their length, which can result in the removal of insulator from the side walls of the laser ridges during the etch, in turn producing short-circuits during device operation. Once etching of the contact windows is complete, the wafer is stripped of any remaining photoresist and again three-solvent cleaned.

In preparation for the deposition of the top electrical contact, a further lithographic step is performed in order to add a series of thin photoresist channels in between each laser ridge. The sample is then placed inside a thermal evaporator and 10nm of titanium (Ti) followed by 200nm of gold (Au) are deposited on the top surface - the Ti acting as an adhesive layer for the Au. The resist channels act to partially shadow the gold as it is being evaporated, resulting in only partial coverage over these areas. After Au

deposition the sample is given an acetone soak, whereby the partially covered resist channels allow acetone to penetrate beneath the Au and dissolve the resist underneath. This removal of resist results in the 'lift-off' of the Au covering the resist, and leaves a series of Au-covered laser ridges that are separated by insulating Si_3N_4 and thus electrically isolated from one another. The top contact is finished with a 360°C anneal using a rapid thermal annealer (Mattson RTA).

By way of improving the heat extraction from the back of the wafer, as well as aiding the cleavage of the wafer into individual devices in the final stages of processing, the thickness of the GaAs substrate is mechanically thinned from 350µm to ~200µm using diamond paste with a successively fine grain size. A back contact consisting of 20nm In/Ge and 200nm Au is then evaporated onto the thinned surface and annealed as before. At this stage the wafer can be cleaved, mounted and wire-bonded to produce working devices. It is desirable in some cases however, to add several microns of electroplated gold to the top contact of the wafer. This additional gold has two purposes; firstly to increase the heat extraction from the laser ridges and so improve the high temperature performance of devices, and secondly to provide a planar surface with which to aid the mounting of devices epi-layer down, in the case where the wafer has been etched in a 'trench' configuration. Electroplating is achieved by immersing the sample in a solution of gold electrolyte and applying a small electrical current - the sample acting as the cathode and a platinum wire mesh as the anode - with gold deposition proceeding at a rate of approximately 1µm/hour. Gold thicknesses of 5µm and above are typically added during this stage. A final lithography step prior to electroplating results in a series of photoresist stripes that run perpendicularly to the laser ridges at intervals of between 1-4mm, (i.e. the length of a typical device), and prevents deposition of electroplated gold over these regions. Since cleavage through electroplated gold is generally non-uniform (if possible at all), these un-plated channels allow the cleavage of the wafer at right-angles to the ridges, and the subsequent formation of the laser facets.

With the metallisation of the sample complete, and depending upon the particular mounting requirements, devices can now be cleaved from the wafer either individually or in sections containing several lasers. A Loomis scribe and break system is used for this purpose which allows the choice of any device length for un-plated wafers, or in the case of plated wafers, to cleave in fixed lengths determined by the separation of the

electroplated sections. Newly cleaved devices are then mounted and indium-soldered onto either gold-coated nickel T05 headers, or for single devices that may also require epi-layer down mounting, soldered onto gold-coated aluminium-nitride ceramic tiles. Electrical contact to the devices is made with the addition of gold wiring between the device and the connection pins of the mount. The completed QCLs can then be characterised in a variety of ways, details of which follow in the next section.

3.4 Device Characterisation

3.4.1 Experimental Set-up

The characterisation of a QCL involves the measurement of several fundamental properties common to all semiconductor lasers including emission spectra, current-voltage curves and device power output as a function of drive current. Shown in figure 3.3 is the experimental apparatus employed in this process.

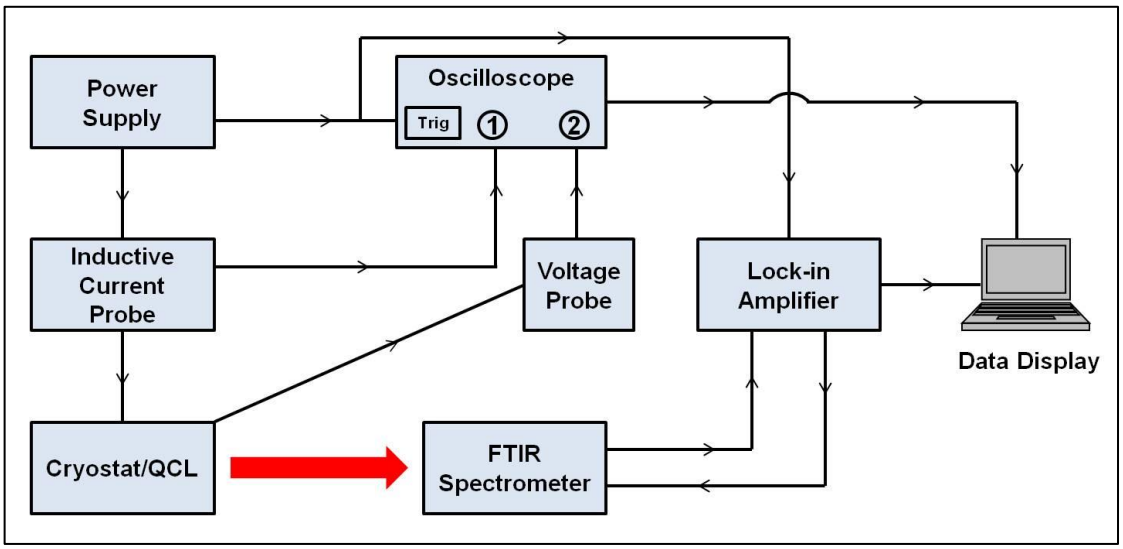

Figure 3.3: Schematic diagram showing the key components used to experimentally determine the optical and electrical characteristics of QCL devices.

Depending on the type of mount used in the fabrication process, devices can be sealed under high vacuum inside a continuous-flow cryostat (Janis Research Co), which allows variation of the operating temperature from ~10K (if using liquid helium as the cryogen), to over 400K. Access to the laser light is provided by a zinc-selenide window. Alternatively, if only room temperature measurements are required, lasers can be mounted on a simple translation stage in front of the spectrometer optics.

Devices are driven using one of several power supplies (Avtech AVL-2-C/AV-1101-C and TTi PL330P), the choice of which depends on the current required, whether lasers are to be operated in continuous wave (CW) or pulsed mode and - if operating in pulsed mode - the pulse lengths and repetition rates desired. For pulsed operation, a maximum drive current of 10A is available at pulse widths of up to 50ms and repetition rates of 10MHz. Above these limits, devices can be driven in the CW regime up to a maximum current of 3A. An inductive current probe calibrated such that a conversion of 1V/A is produced allows the drive current to be recorded on an oscilloscope. The light output from the QCL is analysed using an infrared spectrometer (Bruker IFS 66v/S), which houses a mercury-cadmium-telluride (MCT) detector. The resultant signal from the MCT is passed to a lock-in amplifier (LIA, EG&G Instruments), where it is combined with the original drive signal from the laser and converted to a D.C. output that can be read as a voltage from the LIA display, allowing power versus current characteristics to be measured.

3.4.2 Fourier Transform Infrared Spectroscopy

QCL spectra are recorded using the technique of Fourier transform infrared (FTIR) spectroscopy. Rather than directly measuring the laser output using the MCT detector, the emitted radiation is first modified by an interferometer within the spectrometer, before the resultant signal is analysed and mathematically manipulated in order to produce the IR spectrum. Figure 3.4 shows a schematic representation of the interferometer used to modify the QCL output.

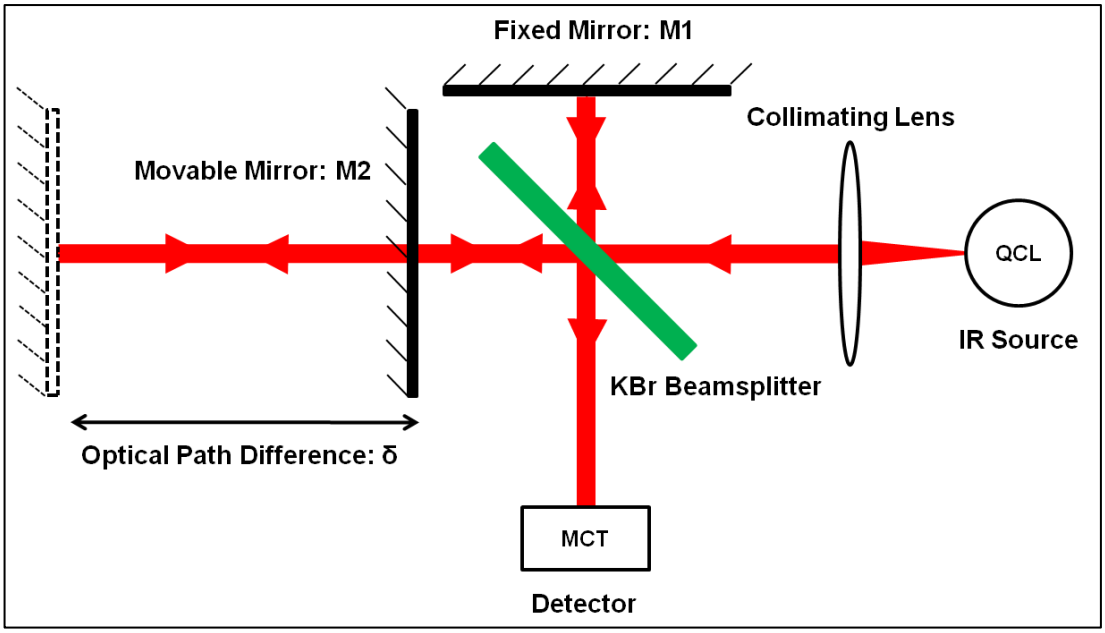

Figure 3.4: Schematic diagram detailing the interferometer system inside the FTIR spectrometer used to record QCL spectra.

The light output from the QCL is first collimated before it is incident on a potassium-bromide (KBr) beamsplitter, where it is either reflected towards a fixed mirror M1, positioned at 90° to the path of the incident beam, or else transmitted to a movable mirror M2 - the reflected and transmitted beams each having equal intensity. The beam incident on M1 is then reflected back towards the beamsplitter, where it undergoes either a second reflection back to the QCL source or is transmitted on to the MCT detector. The beam incident on M2 is also reflected back to the beamsplitter, however in this case the movement of the mirror results in a changing optical path difference δ, relative to the beam travelling to M1, inducing a phase shift between the two when they recombine at the beamsplitter. Depending on the position of M2 and the corresponding phase shift, the two beams will interfere constructively, destructively or somewhere in between, thus producing a resultant beam with an intensity that varies as a function of optical path difference, $I(\delta)$. It is this varying IR beam which is transmitted to the MCT detector and recorded by the spectrometer as an interferogram (see figure 3.5). Furthermore, since the QCL output will generally be multi-mode consisting of emission over a range of wavenumbers ν, the interferogram will represent the sum of this emission at each particular wavenumber.

This interferogram measured by the spectrometer can be represented by[6]:

$$I(\delta) = \int_{-\infty}^{+\infty} B(\nu) cos 2\pi\nu\delta d\nu \tag{3.2}$$

where *B(ν)* is the individual intensities of radiation measured as a function of wavenumber. In order to recover the total QCL spectra - i.e. the total light intensity as a function of wavenumber - the interferogram data can be converted using the Fourier transform:

$$B(\nu) = \int_{-\infty}^{+\infty} I(\delta) cos 2\pi\nu\delta d\delta \tag{3.3}$$

This transform is performed automatically by the spectrometer software once data acquisition is complete. The majority of laser spectra presented in this work were measured with devices operating in pulsed mode. In this instance, the mirror M2 within the interferometer is moved sequentially along its path, pausing at set intervals to allow measurements to be made. This method of data capture is referred to as step-scan FTIR spectroscopy, and is designed to resolve the issue of spectra being modified due to the pulsed nature of the output itself. If the mirror were to move continuously at a constant velocity (as it does in so-called rapid-scan mode when measuring CW output), the laser output would be modulated with a characteristic Fourier frequency proportional to both the velocity of the mirror and the wavenumber of the radiation[7]. This Fourier modulation can combine with the already modulated radiation from the pulsed operation of the QCL to artificially alter the resulting spectrum. By moving the mirror sequentially, the Fourier frequency is eliminated (since the mirror velocity is zero when measurements are taken) and the true spectrum can be recovered.

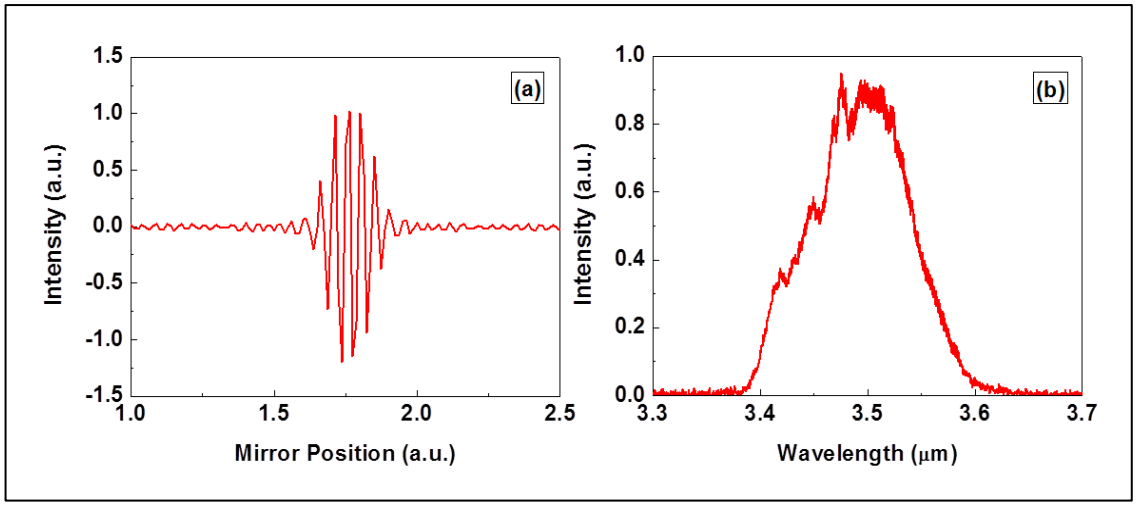

Figure 3.5: (a) Interferogram produced by the FTIR spectrometer showing the intensity of QCL output as a function of the moving mirror's position. (b) The QCL spectra obtained from applying a Fourier transform to the interferogram data shown in (a).

The ability of the FTIR spectrometer to measure all wavelengths simultaneously during a single scan represents a major advantage when compared to techniques that utilise gratings or prisms to separate light into its component wavelengths, as it allows spectra to be obtained more rapidly. Other benefits of the Fourier transform method include the ability to perform and average multiple scans over a short period of time, which leads to an improved signal to noise ratio in comparison to dispersive spectroscopy methods[8].

3.4.3 I-V and L-I Measurements

QCL current-voltage (I-V) characteristics are recorded using a high-impedance voltage probe to measure the voltage applied across the device, while the changing current is displayed by the oscilloscope via the inductive probe. The resultant data can be recorded remotely as an I-V curve. I-Vs can be measured either at room or liquid nitrogen temperatures (~293K and 77K). Output power as a function of drive current (L-I) is recorded by calibrating the LIA output against the maximum device output power collected from a single facet, as measured using a thermopile detector (Molectron EPM1000). This allows power versus current curves to be recorded from zero current to beyond rollover of the laser output. Depending on the coolant used in the cryostat, L-Is can be measured at operating temperatures ranging from ~10K up to 300K and beyond in the case of the best performing devices. This temperature dependant data allows

calculation of a device's characteristic temperature T_0, which describes the rate of increase of threshold current density with temperature.

3.4.4 Waveguide Losses

The waveguide losses α_w, associated with a particular wafer design can be determined experimentally by measurement of the threshold current density J_{th}, of a series of devices of differing length. The threshold current density expressed in terms of the device losses is given by[9]:

$$J_{th} = \frac{\alpha_m + \alpha_w}{g\Gamma} \tag{3.4}$$

where α_m and α_w are the mirror and waveguide losses respectively, Γ is the waveguide confinement factor and g is the gain coefficient - defined as the peak material gain per unit threshold current density i.e. $g=G_p/J_{th}$. The mirror losses are dependent both upon the reflectivities R_1 and R_2 of the laser facets and the length L, of the laser cavity:

$$\alpha_m = -\frac{ln(R_1R_2)}{2L} \tag{3.5}$$

Substitution of equation 3.5 into 3.4 allows the threshold current density to be expressed as a function of device length:

$$J_{th} = \frac{\alpha_w}{g\Gamma} - \frac{ln(R_1R_2)}{2g\Gamma}\frac{1}{L} \tag{3.6}$$

It can be seen therefore that measuring the threshold current of devices of different length and plotting J_{th} against *1/L* should yield a linear relationship with:

$$gradient = -\frac{ln(R_1 R_2)}{2g\Gamma} \qquad \text{and} \qquad intercept = \frac{\alpha_w}{g\Gamma} \qquad \text{(3.7a and 3.7b)}$$

The facet reflectivities R_1 and R_2 are both assumed to be approximately 30%, and so an estimate of the quantity $g\Gamma$ can be made from the gradient. This can then in turn be used in equation 3.7b to calculate α_w.

3.4.5 Characteristic Temperature - T_0

The evolution of a device's threshold current density with increasing temperature can be conveniently described by the parameter T_0 - its characteristic temperature. It is generally found that J_{th} increases exponentially over a well-defined temperature range which can be described by the relationship[10]:

$$J_{th}(T) = J_0 exp\left(\frac{T}{T_0}\right) \qquad (3.8)$$

It can be seen from equation 3.8 that T_0 can be extracted from a linear fit of the natural logarithm of J_{th} plotted against T, over the temperature range for which the relationship holds. Higher values of T_0 are indicative of a threshold current density that increases more slowly with temperature, and vice versa for low T_0. For devices that operate at high temperatures and/or in the CW regime, a low initial J_{th} coupled with a high T_0 is desirable in order to minimise the high operating temperatures associated with large drive currents. Characteristic temperatures of the order of 100K are typical for the GaAs-based devices presented in this thesis.

1. *National Centre for III-V Technologies [Online]*, Availiable at: http://www.epsrciii-vcentre.com/Home.aspx, (2013).

2. M. A. Herman, W. Richter and H. Sitter, *Epitaxy: Physical Principles and Technical Implementation*, (Springer, 2004).

3. G. B. Stringfellow, *A critical appraisal of growth mechanisms in MOVPE*, Journal of Crystal Growth, **68**, 111-122, (1984).

4. *Clean Rooms - ISO Standard 14644 [Online]*, Availiable at: http://www.engineeringtoolbox.com/clean-rooms-iso-d_933.html, (2013).

5. S. Franssila, *Introduction to Microfabrication*, (Wiley, 2010).

6. E. Huys, *A Short Introduction to FTIR*, (Bruker Optik).

7. T. J. Johnson and G. Zachmann, *Introduction to Step-scan FTIR*, (Bruker Optik).

8. J. F. James, *A Student's Guide to Fourier Transforms: With Applications in Physics and Engineering*, (Cambridge University Press, 1995).

9. J. Faist, F. Capasso, D. L. Sivco, C. Sirtori, A. L. Hutchinson and A. Y. Cho, *Quantum Cascade Laser*, Science, **264**, 553-556, (1994).

10. C. Gmachl, F. Capasso, D. L. Sivco and A. Y. Cho, *Recent progress in quantum cascade lasers and applications*, Reports on Progress in Physics, **64**, 1533-1601, (2001).

Chapter Four

GaAs-based QCLs with InGaP and InAlP Waveguides

4.1 Introduction

The chapter begins with a brief review of the work carried out at the University of Sheffield on GaAs-based QCLs that is directly relevant to the studies presented in the experimental chapters of this thesis. Following on from this, several new GaAs-based QCL wafer designs are presented, into which both InGaP and InAlP have been incorporated as a waveguide material. These designs represent a continuation of the work previously undertaken at Sheffield, as well as an attempt to further enhance the performance levels achievable from GaAs QCLs. The operating characteristics of devices fabricated from these wafers are then presented and analysed, with comparisons made to previous GaAs-based lasers.

4.2 GaAs-based QCLs: Sheffield Progress

The study of GaAs-based QCLs at the University of Sheffield spans a timeframe of over a decade and has touched upon several different areas of development, from fundamental studies of the electron distribution within the QCL core region[1] to more applied areas such as the development of MOVPE growth of GaAs-based devices[2]. Of particular relevance to the work presented in this thesis, are the investigations that were carried out by physicists at Sheffield that sought to optimise device performance through adaptation of the laser waveguide. As will be discussed in more detail shortly, GaAs-based QCLs generally make use of either highly doped GaAs or high aluminium

content AlGaAs layers to form the device waveguide, both of which have their relative merits and limitations.

As an alternative to these materials, Green and co-workers designed and fabricated a $GaAs/Al_{0.45}Ga_{0.55}As$ QCL that incorporated an $In_{0.49}Ga_{0.51}P$ waveguide[3], which it was hoped would improved device performance through both the increased confinement of the optical mode within the core region, and lower waveguide losses. When characterised, this device was seen to operate up to 305K - the first time room-temperature operation of a GaAs-based QCL had been observed at Sheffield, and a considerable improvement in the 190K maximum operating temperature measured for previous GaAs/AlGaAs devices[4]. Although the threshold current density of ~6kA/cm^2 at 77K represented an increase of ~1.5kA/cm^2 in comparison to earlier lasers[5], operating voltages were found to be near identical to previous devices. These encouraging results appeared to confirm the potential of InGaP waveguides for enhancing GaAs-based QCL performance.

Following on from this work, Krysa et al grew a similar GaAs/AlGaAs QCL structure with InGaP waveguide, but using MOVPE rather than MBE which had been used for all previous QCL growth[6]. The structure itself was modified somewhat in an attempt to optimise performance and further reduce optical losses within the device core, with the design changes including a doubling of the waveguide thickness to 3μm and a reduction in doping to N=5x10^{16}cm^{-3}. An additional GaAs cladding layer was also inserted between the lower waveguide and GaAs substrate. These refinements resulted in devices that again demonstrated operation at room temperature, but with greatly enhanced optical and electrical characteristics than those observed previously. Room-temperature threshold current density and peak output power from a 4mm-long, high-reflection coated device were found to be 6.5kA/cm^2 and 220mW respectively, with an emission wavelength of λ~9μm. In comparison, the previous InGaP laser could only achieve a room-temperature J_{th} of ~32kA/cm^2 and peak output power of the order of several milliwatts.

These results represented excellent progress in improving GaAs QCL performance in terms of the threshold currents that could be achieved from devices, which were the lowest J_{th} observed at room-temperature at the time. However, as a conclusion to the study it was suggested that performance might be further enhanced through the use of

InAlP as a waveguide material, due to its lower refractive index compared to InGaP and therefore greater potential for optical confinement. It is this juncture that marks the starting point for the work presented in these experimental chapters.

4.3 Phosphide Materials as QCL Waveguides

QCL performance is strongly dependent upon the efficiency with which the optical mode can be confined to the device core region. For example, as was seen in chapter two, the threshold current density is inversely proportional to the device modal gain (defined as the material gain multiplied by the mode confinement factor Γ), and directly proportional to the waveguide loss α_w (expressed within the total cavity losses α_{tot}). Maximising the overlap of the optical mode with the device core allows the modal gain to be increased, while decreasing α_w by reducing the proportion of the optical mode that reaches the material layers that constitute the rest of the structure. As with the majority of semiconductor lasers, QCL devices achieve this overlap by utilising waveguide layers that have a lower refractive index than the core region they surround, with the refractive index contrast providing the mechanism for confinement of the light generated within the active region.

In the case of the earliest GaAs-based QCLs, the waveguide layers were provided by high-Al fraction $Al_{0.9}Ga_{0.1}As$[7], which possessed a relatively high refractive index contrast with the GaAs/AlGaAs core region and exhibited low optical losses at the emission wavelength of λ=9.4μm. Additionally, the waveguide layer thicknesses of $\lesssim$1μm meant the overall thickness of the device structure was minimised. Several drawbacks to the use of $Al_{0.9}Ga_{0.1}As$ were soon discovered however, including a large variation in device threshold current and output power under illumination with white light at low temperature[8]. This behaviour was found to result from the release of electrons from DX centres within the waveguide layers causing a subsequent increase in waveguide losses. The low electron mobility and electrical conductivity were also cited as potential drawbacks associated with this material system. In an attempt to overcome these limitations, later GaAs devices employed a waveguide consisting of layers of highly doped GaAs[9], which utilised the large drop in refractive index that occurs at wavelengths corresponding to the material's plasma frequency. The plasma frequency

and refractive index of the waveguide layer can be tailored through changes to its doping level, which can be of the order of $N \sim 10^{18}\text{cm}^{-3}$ at infrared wavelengths. Other advantages of using GaAs over AlGaAs include the lower demands placed on wafer growth[6] and the lower thermal conductivity of the binary compound compared to the ternary AlGaAs alloy.

The use of GaAs as a waveguide material has to-date proven sufficient to enable GaAs-based devices to achieve performance levels ranging from low-temperature CW[10,11] to room-temperature pulsed[12] operation. There are however, several perceived disadvantages to the use of GaAs that make the investigation of new waveguide materials a worthwhile endeavour. For example, the high doping levels required must be precisely controlled during growth in order to achieve the required refractive index, with small fluctuations able to cause a large shift from the desired index. The highly doped layers can also lead to increased free-carrier absorption of the optical mode, and so thick low-doped GaAs layers are grown surrounding the core in order to spatially separate the mode from the waveguide. This can substantially increase the total thickness of the device structure.

As a response to these shortcomings, the idea of using phosphide-containing alloys as a waveguide material in GaAs-based QCLs has been suggested[3,6], and studies of the performance of such devices make up the majority of the work presented in this thesis. The two alloys in question - InGaP and InAlP - have various characteristics that make them promising candidates for such an application. Both have a refractive index contrast with GaAs/AlGaAs sufficient for a large confinement of the optical mode at infrared wavelengths, while the lack of need for high doping to achieve their low refractive indices means InGaP and InAlP do not suffer from the large free-carrier losses associated with GaAs waveguides. This removes the need to have thick spacer layers surrounding the core region and allows the thickness of the device structure to be kept comparatively low. Additionally - for InGaP at least - good electrical characteristics should be facilitated by the InGaP/GaAs conduction band offset of 0.16eV[13], a point that will be discussed in detail later in this thesis.

In order to compare the levels of optical confinement and loss that these different waveguide materials might provide, figures 4.1 to 4.4 show a series of TM optical mode profiles for four different waveguide structures surrounding an identical GaAs/AlGaAs

core region, calculated for emission at a wavelength of 9µm. The method used to produce the profiles is described in detail in chapter two and appendix A.2. Figures 4.1 and 4.2 detail QCL structures with waveguides comprising of $Al_{0.9}Ga_{0.1}As$ and highly-doped GaAs respectively, and are based on designs presented in references [7] and [9]. Although these structures are not optimised for the core region in question, the emission wavelength is close enough to that of the original design that the calculated confinement and losses are very similar. Figures 4.3 and 4.4 show the same core region, but the AlGaAs and GaAs waveguide layers have been replaced with InGaP and InAlP respectively.

Starting with the $Al_{0.9}Ga_{0.1}As$ waveguide structure below in figure 4.1, it can be seen that for a refractive index contrast of Δn_{ref}=0.4, an optical confinement of Γ=63% could be expected for a wavelength of λ=9µm. Despite the GaAs spacer layers surrounding the core region, approximately 4% of the optical mode penetrates into the waveguide layers resulting in a waveguide loss of α_w=13cm^{-1}.

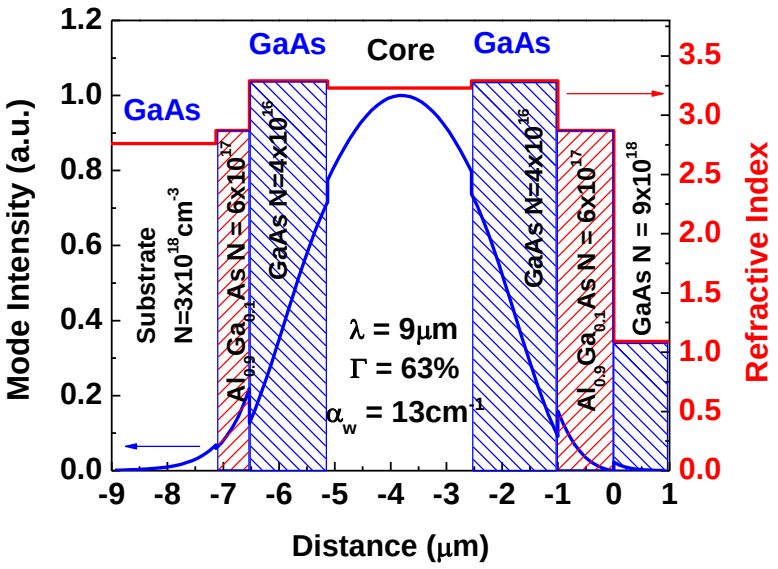

Figure 4.1: TM optical mode profile detailing the calculated mode intensity (left-hand axis) and waveguide refractive index (right-hand axis) for a QCL device operating at 9µm and featuring an $Al_{0.9}Ga_{0.1}As$ waveguide structure taken from reference [7]. Doping levels for all profiles are given in cm^{-3}.

In figure 4.2 the $Al_{0.9}Ga_{0.1}As$ layers have been replaced with highly-doped (N=6x10^{18}cm^{-3}) GaAs. Although there is a large refractive index contrast between the

high-doped GaAs layers and the core region (Δn_{ref}~1.2), the optical confinement of Γ=42% afforded by the GaAs waveguide is relatively low in comparison to the AlGaAs design. This is mainly due to the comparatively thick (3.5μm) GaAs spacer layers that are required to spatially separate the optical mode from the highly-doped (and thus highly lossy) GaAs waveguide layers. Although optical confinement within the core is lower, the spacer layers ensure very little of the mode penetrates the waveguide (~0.5%) and thus losses are reduced to α_w=11cm^{-1}.

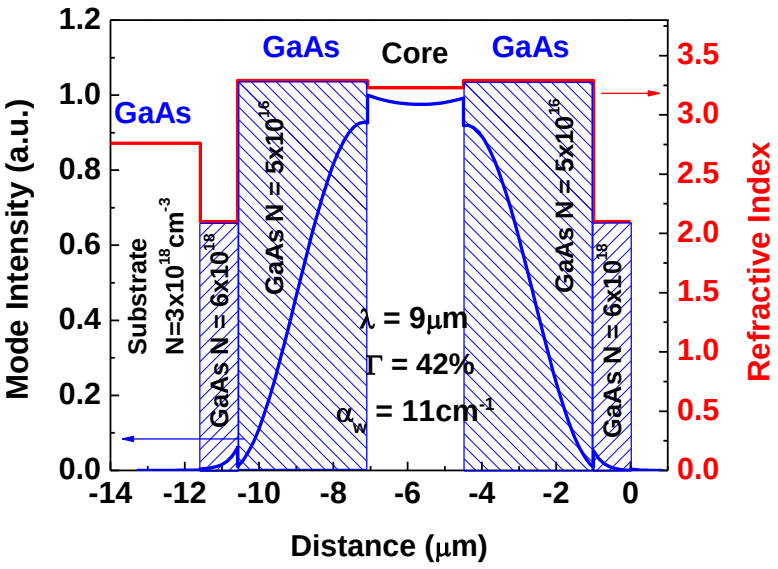

Figure 4.2: TM mode profile for the same core region as featured in figure 4.1, but with a highly-doped (N=6x10^{18}cm^{-3}) GaAs waveguide taken from reference [9].

By replacing the GaAs waveguide layers with $In_{0.49}Ga_{0.51}P$, a large increase in optical confinement can be attained, illustrated by the mode profile shown in figure 4.3. The GaAs spacer layers (shown as the blue hatched areas surrounding the core) are primarily included to increase the refractive index contrast with the waveguide (Δn_{ref}=0.25), rather than to separate the mode from the InGaP layers which are low-doped, and so not expected to contribute to free-carrier loss. The refractive index contrast combined with the thin GaAs spacer means optical confinement is increased to Γ=62%, while only ~0.2% of the mode is able to reach the outer layers of the structure. This results in a correspondingly low waveguide loss of α_w=6cm^{-1}.

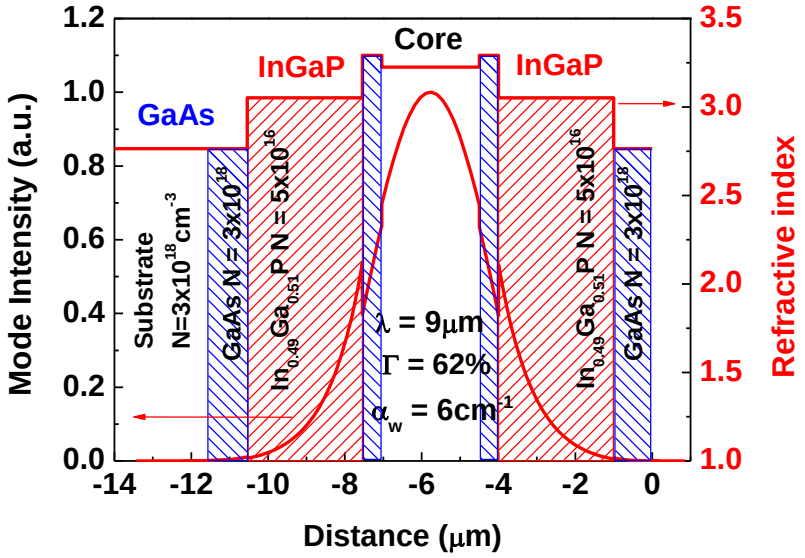

Figure 4.3: TM mode profile showing the calculated mode intensity provided by an $In_{0.49}Ga_{0.51}P$ waveguide structure surrounding the same core as that featured in figure 4.1.

Substitution of the InGaP layers with $In_{0.47}Al_{0.53}P$ leads to a doubling of the index contrast to Δn_{ref}=0.5, and with it a corresponding enhancement of the modal overlap to Γ=72%, while waveguide losses remain similar to the InGaP waveguide at α_w=5cm^{-1} (figure 4.4).

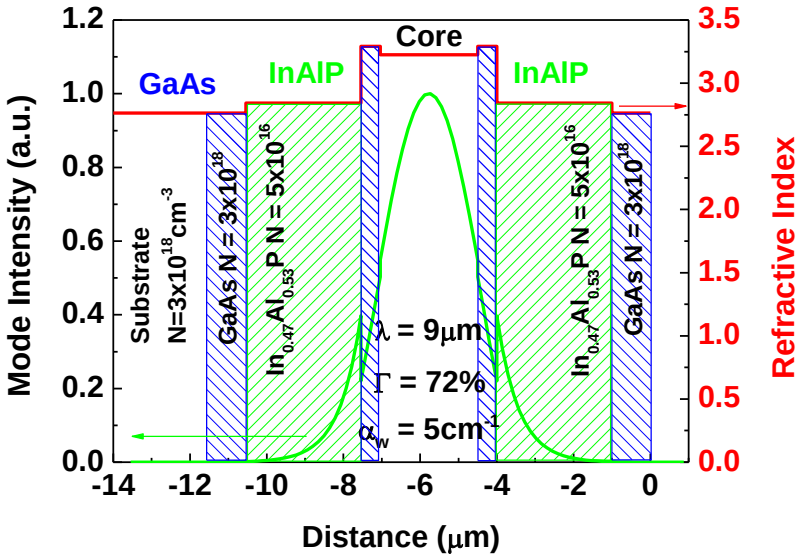

Figure 4.4: TM mode profile showing the confinement provided by an $In_{0.47}Al_{0.53}P$ waveguide structure surrounding the core detailed in figure 4.1.

These calculations demonstrate the potential that both InGaP and InAlP have for use as low-loss QCL waveguides that offer high optical confinement at infra-red wavelengths. The materials are lattice matched to GaAs for the compositions $In_{0.49}Ga_{0.51}P$ and $In_{0.47}Al_{0.53}P$, and can be easily incorporated into typical GaAs-based QCL structures using MOVPE. The experimental results detailed in the following sections will demonstrate this potential by showing the performance enhancements, particularly in regard to threshold current, that can be achieved in devices that utilise these two materials as waveguide layers.

4.4 GaAs/AlGaAs QCLs with InGaP and InAlP Waveguides

Following on from the work by Krysa et al, a series of four QCL wafers incorporating either InGaP or InAlP waveguide layers were grown in order to investigate whether the performance of GaAs QCLs could indeed be enhanced via further modification to the waveguide. The wafers are given the designations MR2784, MR2785, MR2789 and MR2790, with the general layer structure of each wafer shown in figure 4.8. By producing a series of wafers with differing designs, it is possible to investigate the effect that changes in either the active region or waveguide (or in some cases both) have on laser performance. For example, wafer MR2784 is essentially a copy of the design of the laser with InGaP waveguide presented in section 4.2, with minor alterations to the core region. Wafer MR2789 on the other hand incorporates a completely new InAlP waveguide whilst keeping unchanged the core region design of MR2785 (which has an InGaP waveguide) allowing for comparison between the two material systems. A detailed discussion of the design approach for each wafer is given in the following section, which includes descriptions of the complete wafer structure, core region design and the electronic wavefunctions associated with device operation.

4.5 Wafer Design

In common with wafers grown for the previous work on GaAs lasers with InGaP waveguides (described in section 4.2), all QCL structures were grown on an N^+ (100) GaAs substrate (N=3x10^{18}cm^{-3}) with a 10° miscut toward the (111) plane. These non-standard substrates are necessary to mitigate the effects of Cu-type atomic ordering in the InGaP and InAlP layers[3]. A low-pressure, horizontal-flow MOPVE reactor operating at 690°C for InGaP growth and 710°C for InAlP growth was used, and each structure was grown in a single run.

MR2784

By way of acting as a reference to our group's previous QCLs with InGaP waveguides, wafer MR2784 incorporated a GaAs/$Al_{0.45}Ga_{0.55}As$ core region identical to that featured in the device detailed in section 4.2, designed to emit at λ~9µm. The number of core region repeat periods however, was increased from 36 to 55 in order to increase the overlap of the optical mode with the core region and thus also the optical gain. By increasing this core region overlap it was also hoped that the optical mode would penetrate less into the highly doped outer cladding layers of the wafer, leading to an overall decrease in the waveguide losses. Calculations of these parameters for MR2784 show that an optical confinement of Γ~62% may be expected, an increase from the Γ~42% estimated for the previous device with its narrower core region, while waveguide losses are also decreased - α_w=5.7cm^{-1} compared to α_w=9.5cm^{-1}. All other wafers described in this section have 55 repeat periods of their respective core regions.

Starting from the GaAs substrate, the layer sequence for MR2784 was: 1µm highly-doped (N=3x10^{18}cm^{-3}) GaAs, 3µm $In_{0.49}Ga_{0.51}P$ (N=5x10^{16}cm^{-3}) waveguide and 0.5µm GaAs spacer layer (N=5x10^{16}cm^{-3}). The 55 period (2.54µm) core region follows, and the layer sequence then continues with a repeat of the 0.5µm GaAs spacer, 3µm InGaP waveguide and 1µm GaAs layer to complete the structure. The Γ-point conduction band profile for the core region of MR2784, including the moduli squared of the electronic wavefunctions is shown in figure 4.5, where the wavefunction E_u corresponds to the upper laser level, E_l to the lower laser levels and E_i to the injection level. The dipole

matrix element for the diagonal optical transition between E_u and E_l was calculated to be z_{ij}=2.4nm.

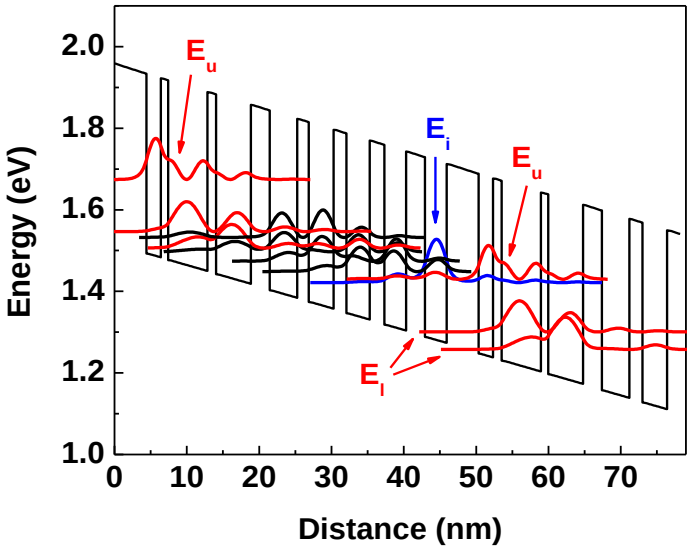

Figure 4.5: Γ-point conduction band profile for the core region of sample MR2784 under a bias of 48kV/cm^2. The profile includes the moduli-squared of the electronic wavefunctions associated with the optical transition (E_u and E_l in red), the injector level (E_l in blue) and the injector miniband (black).

The sequence of wells and barriers that constitutes one complete period of core region (i.e. one active and one injector region) is as follows (where thicknesses are given in nm and begin at the injection barrier): **4.5**/2.0/**1.1**/5.4/**1.1**/4.8/**2.6**/3.8/**1.7**/3.4/**1.8**/3.2/**2.0**/3.0/**2.6**/3.0. Normal font represents the GaAs quantum wells, bold font the $Al_{0.45}Ga_{0.55}As$ barriers and underlined layers are Si-doped (N=4x10^{17}cm^{-3}).

MR2785

Wafer MR2785 follows the same general layer structure as MR2784, but with an altered core region design that attempts to increase gain by shifting from the diagonal optical transition used previously, to a more vertical transition within the second active region quantum well.

The layer sequence that makes up the active and injector regions is as follows: **4.2**/1.7/**1.0**/5.8/**1.0**/5.2/**2.6**/4.0/**1.7**/3.7/**1.8**/3.3/**2.0**/3.1/**2.6**/3.0, where the character formatting follows the convention described previously. Comparing this core region sequence to that of wafer MR2784, several modifications can be observed. Firstly, the width of the first quantum well has been reduced from 2.0nm to 1.7nm, while the surrounding barriers have also been slightly reduced in thickness. Additionally, the second and third quantum wells that make up the remainder of the active region have been widened to 5.8nm and 5.2nm, from 5.4nm and 4.8nm respectively, with only minor alterations to the associated barriers. Modifications to the injector section of the core region include a widening of the first four quantum wells by 0.2nm, 0.3nm, 0.1nm and 0.1nm respectively, while all injector region barriers remain unchanged.

Figure 4.6 shows the conduction band profile for the core region of MR2785. It can be seen that the primary effect of narrowing the first active region quantum well is to allow the wavefunction associated with the upper laser level E_u, to penetrate further into the second well, reducing the resonance with the injector level E_i but increasing the resonance with the lower laser level E_l. As described in chapter two, this more vertical transition is expected to have a larger dipole matrix element than the previous diagonal transition, which can result in a larger associated intersubband gain. Calculations show that the matrix element for the optical transition associated with this active region design is z_{ij}=2.7nm, an increase from z_{ij}=2.4nm calculated for MR2784. It is possible therefore that several enhancements in device performance may result, such as a lower threshold current and increased output power[14]. As was discussed in chapter 2 however, vertical transitions also result in a lower population inversion between subbands and can thus act to reduce the intersubband gain and subsequently lower device performance. The success or otherwise of this vertical transition design will be discussed in the section detailing device performance.

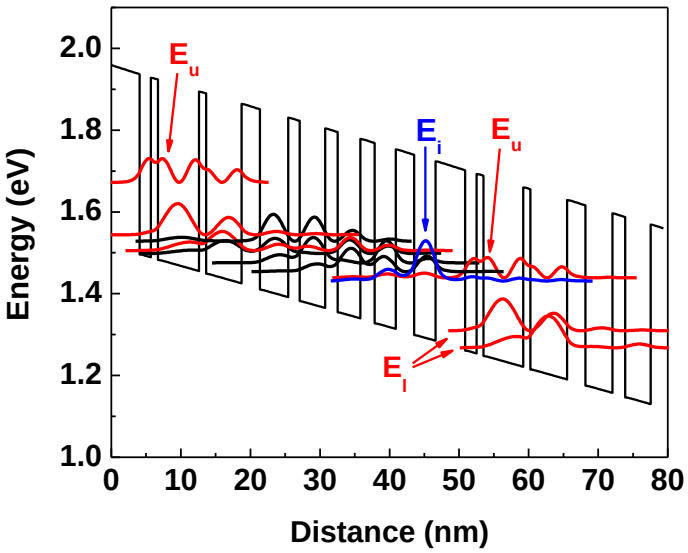

Figure 4.6: Γ-point conduction band profile for the core region of sample MR2785 under a bias of 48kV/cm^2, including the electronic wavefunctions relevant to the optical transition.

MR2789

Wafer MR2789 features the same core region design as that of MR2785 above, but with an InAlP waveguide replacing the previous InGaP layer. Calculations suggest that the optical confinement afforded by the InAlP should increase to ~74% compared to 63% for the InGaP waveguide, while the waveguide loss decreases from 5.7cm^{-1} previously to 4.8cm^{-1}. A summary of the confinement factor and waveguide losses expected for each individual device is presented in table 4.1. The effect of this theoretical increase in confinement, along with the corresponding changes in performance of lasers fabricated from the two wafers is outlined in section 4.6 which presents individual laser characteristics.

Beginning from the N^+ GaAs substrate, the complete wafer structure of MR2789 was: 1µm of highly-doped (N=3x10^{18}cm^{-3}) GaAs, 3µm $In_{0.47}Al_{0.53}P$ waveguide layer (N=5x10^{16}cm^{-3}), 0.2µm GaAs spacer layer (N=5x10^{16}cm^{-3}) followed by the 55-period GaAs/$Al_{0.45}Ga_{0.55}As$ core region. The cladding layer sequence is then repeated in reverse to complete the structure. With the InAlP waveguide effectively acting as an electronic barrier with a height of ~0.31eV[15], a 'transitional layer' (TL) was positioned between each GaAs/InAlP interface (see figure 4.8) in order to reduce the abruptness of

the barrier at these points and aid electron flow through the structure. This layer consisted of 25nm of $In_{0.49}Ga_{0.51}P$ followed by 16nm of $In(Ga_{0.5}Al_{0.5})_{0.5}P$ ($5x10^{16}cm^{-3} \leq N \leq 1x10^{17}cm^{-3}$) when transitioning from GaAs to the InAlP waveguide, while the sequence was reversed when transitioning from InAlP to GaAs.

MR2790

Finally, wafer MR2790 duplicates the cladding structure of MR2789 while modifying the active region to incorporate an extra quantum well, thus resulting in a double-phonon relaxation design. One complete period incorporating the active and injector region (beginning from the injection barrier) is as follows: **4.2**/1.8/**0.9**/5.2/**0.9**/5.0/**0.9**/4.7/**2.2**/3.6/**1.7**/3.5/**1.7**/3.3/**1.8**/3.1/**2.1**/2.9/**2.7**/2.9, with the numbering following the usual convention. The conduction band profile for MR2790 is shown below in figure 4.7, and illustrates the additional lower laser level that results from the addition of the fourth active region quantum well. These three lower levels constitute the double-LO-phonon relaxation design discussed in chapter one. The calculated optical matrix element of z_{ij}=3.3nm for this particular active region design represents an increase in comparison to MR2785 and MR2789.

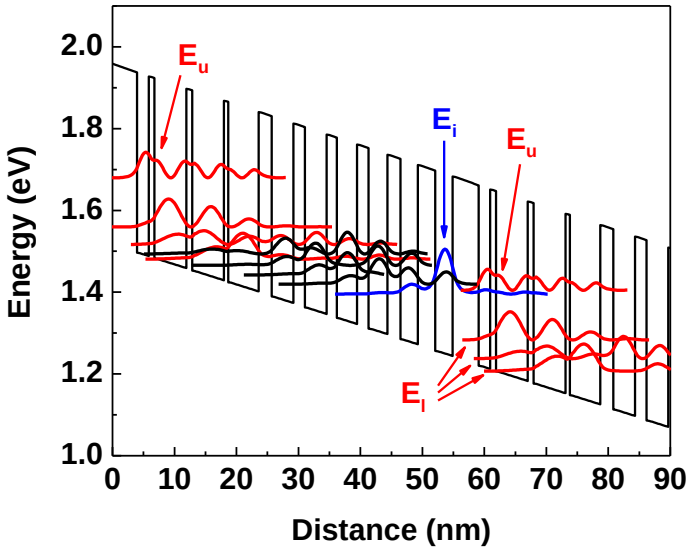

Figure 4.7: Γ-point conduction band profile for the core region of sample MR2790 under a bias of 48kV/cm^2. The profile illustrates the extra lower laser level (E_l in red) that results from the inclusion of a fourth quantum well in the active region.

As with wafer MR2789, 25/16nm InGaP/InGaAlP transitional layers were positioned between each GaAs/InAlP interface in order to aid electron flow through devices.

Design Summary

Shown in table 4.1 is a summary of the design features of each wafer, while table 4.2 lists the bandgap and conduction band offset with respect to GaAs for each waveguide material. Overleaf, figure 4.8 features a schematic diagram showing the layer structure for wafers featuring the InGaP (MR2784/85) and InAlP (MR2789/90) waveguides.

Sample	Active Region Design	Waveguide Material	Confinement Factor - Γ (%)	Waveguide Loss - α_w (cm^{-1})
MR2784	Single-phonon Diagonal transition	$In_{0.49}Ga_{0.51}P$	62	5.7
MR2785	Single-phonon 'Vertical' transition	$In_{0.49}Ga_{0.51}P$	63	5.7
MR2789	Single-phonon 'Vertical' transition	$In_{0.47}Al_{0.53}P$	74	4.8
MR2790	Double-phonon 'Vertical' transition	$In_{0.47}Al_{0.53}P$	81	4.8

Table 4.1: Design summary outlining the features of each sample described in the preceding sections, highlighting the differing optical confinement and waveguide losses expected for each waveguide design at an emission wavelength of λ=9μm.

Waveguide Material	Bandgap (eV)	Conduction Band Offset With Respect To GaAs (eV)
$In_{0.49}Ga_{0.51}P$	1.91 (Direct)[13]	0.16[13]
$In_{0.47}Al_{0.53}P$	2.38 (Indirect)[13]	0.31[15]

Table 4.2: Key band parameters for the InGaP and InAlP waveguides featured in the QCL designs presented in this, and subsequent chapters.

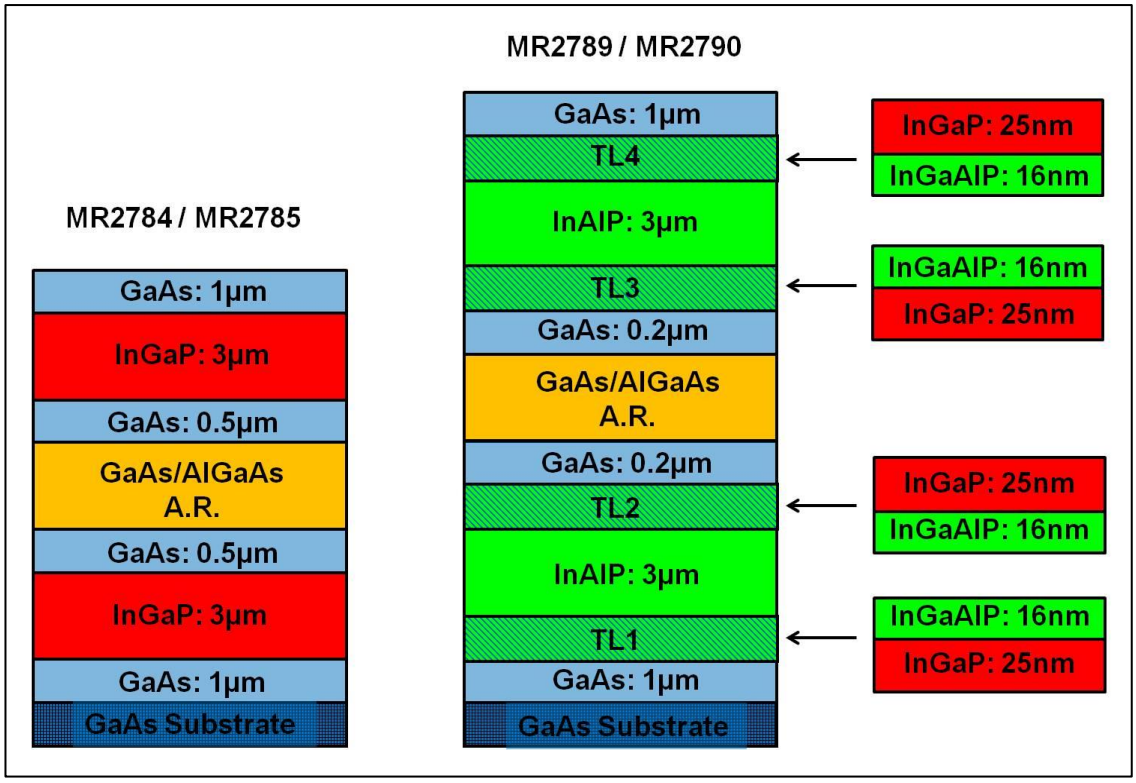

Figure 4.8: Schematic illustration of the semiconductor structure for each wafer, including transitional layers.

4.6 Device Performance

4.6.1 Spectra

Shown in figure 4.9 are the emission spectra obtained from 2mm as-cleaved lasers, taken at 300K using a Fourier transform infrared spectrometer at a resolution of $1cm^{-1}$. Device MR2784 is observed to lase at a wavelength of λ=9.08µm, close to the intended λ~9µm design wavelength of this sample as well as that of the InGaP laser presented previously in section 4.2. This is as expected, considering the identical active region design (albeit with an increased number of core region repeat periods) shared by the two devices. The active regions of devices MR2785 and MR2789 are also identical - sharing the same vertical transition design outlined previously - and as such exhibit operating wavelengths of λ=8.82µm and λ=8.63µm respectively. Finally MR2790, which employs a modified double-phonon active region, displays emission at λ=9.72 µm.

The similarity of emission wavelength between samples with the same active region design, combined with the ability to accurately reproduce the performance of historical devices (i.e. MR2784 and the device presented by Krysa et al) gives confidence in the overall quality and calibration accuracy of the MOVPE growth used to fabricate individual wafers. The wavelength discrepancy between the samples with the longest and shortest emission wavelengths (MR2789 and MR2790), corresponds to an energy of E_λ~16meV, which of the order of a typical GaAs QCL gain spectrum.

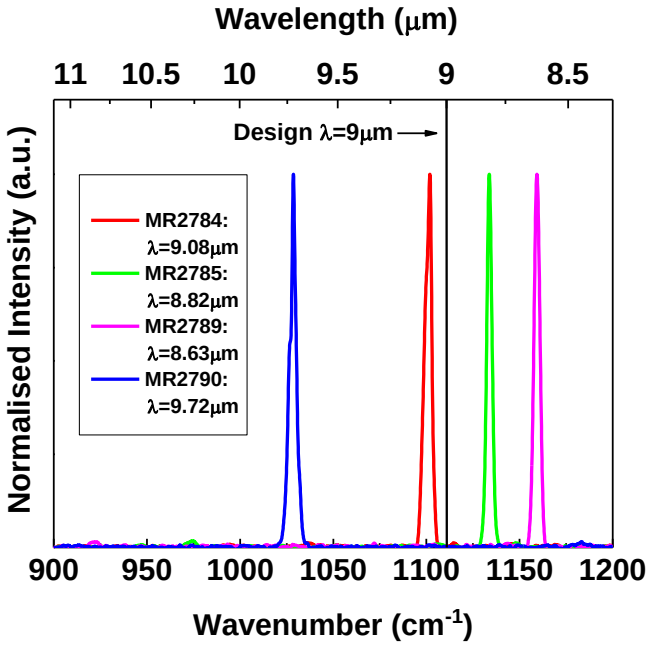

Figure 4.9: Combined spectra showing the room-temperature emission wavelength for 2mm-long, 20μm-wide devices fabricated from each wafer.

4.6.2 Optical and Electrical Performance

A series of 2mm and 3mm-long as-cleaved lasers were characterised under pulsed operation, at a repetition rate of 5kHz and pulse width of 50ns using the techniques described in chapter 3. Due to the high incidence of device failure in some of the samples, the performance data quoted in this and subsequent experimental chapters represents the best performance from a single device rather than an average of several. The threshold current densities quoted throughout the following chapters have an associated uncertainty of ~ ±10%, due to the uncertainties in the width of the laser ridges (which showed evidence of undercutting of the ridge pattern during the etching

process), and the variations in the current pulse shape and position of the oscilloscope gate during measurement. Results are presented below for each individual wafer design.

MR2784

Figure 4.10 shows the typical light-current characteristics for a 2mm-long, 20μm-wide laser fabricated from wafer MR2784. This data, along with the majority of L-I curves presented in this work are typical of most QCL devices. As the bias across the device is increased, the electronic states associated with the optical transition align with the injector miniband enabling efficient electron flow through the device and eventual lasing. Subsequent increases in electrical current result in a concomitant rise in optical output power, as the rate at which electrons are injected into the device core increases along with the active region population inversion. After a time however, the continued increase in bias across the laser core causes the electronic states to become misaligned, resulting in a significant reduction in injection efficiency into the upper laser level and thus a decrease in optical output power - referred to as rollover.

As expected, since the active region designs of MR2784 and the InGaP laser of Krysa et al are nominally identical, the performance of MR2784 shares common characteristics with this device. It has already been noted that the room-temperature emission wavelength of both is similar - 9.08μm (MR2784) compared to 9.2μm previously, however both the temperature range over which the devices operate, and their threshold current densities also display similar values. At 240K, a threshold current density of 4.4kA/cm^2 is observed for device MR2784, rising to 8.2kA/cm^2 at 300K. This is in comparison to 4.5kA/cm^2 and 8.0kA/cm^2 at 240K and 300K respectively for the previous InGaP device. The maximum temperature of operation increases slightly to 340K, up from 320K previously.

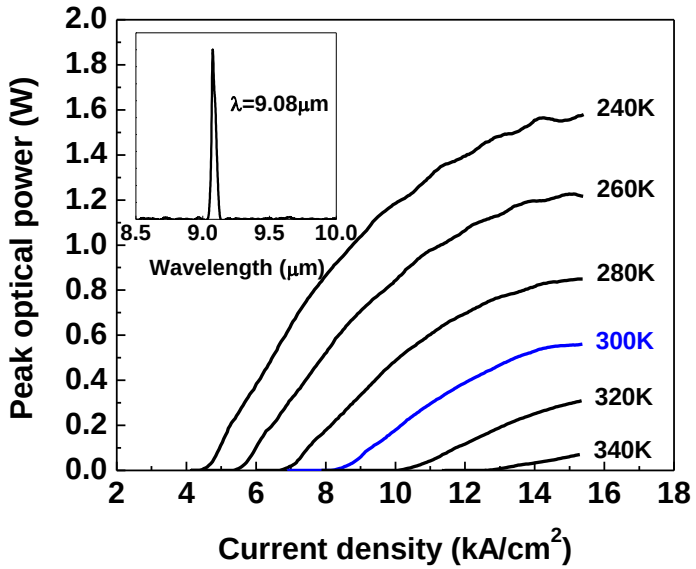

Figure 4.10: Peak output power vs. drive current for a 2mm-long 20μm-wide device fabricated from wafer MR2784. Inset: High-resolution (0.5cm^{-1}) FTIR spectra showing emission at 9.08μm for the same device.

While the threshold currents for MR2784 and the previous InGaP laser are comparable over the entire operating temperature range, a large increase in peak optical output power (as measured from a single facet) is observed for the new device. At 240K, a maximum output power of 1.58W is observed - an increase of over 1W compared to that reported by Krysa et al at the same temperature. At 300K, MR2784 continued to deliver 0.56W of power, compared to 0.11W previously. A second 3mm-long, 20μm-wide device fabricated from wafer MR2784 exhibited similar threshold current densities, with J_{th}=4.3kA/cm^2 at 240K and 8.0kA/cm^2 at 300K, however the output power, particularly at 240K, was substantially lower compared to the 2mm laser. Powers of 0.73W and 0.32W at 240K and 300K respectively were observed, although it should be noted that the maximum current with which the 3mm device was driven was reduced to ~11kA/cm^2 to prevent premature device failure. The greater observed output power seen for MR2784, when compared to the previous InGaP QCL, could be attributed to the increase in the number of active region periods from 36 to 55. The negligible reduction in threshold current density that is observed between the devices however, lends uncertainty to this conclusion since (from equation 3.4) we would expected a lowering of J_{th} due to the increased modal overlap in the wider core region of MR2784.

Shown in figure 4.11 below is an exponential fit of the threshold current density versus temperature data for the 2mm device, with the associated value for the characteristic temperature T_0. It is found that this fit can be applied to both 2mm and 3mm lasers over the entire temperature range of operation, resulting in T_0=95±11K and T_0=99±13K respectively.

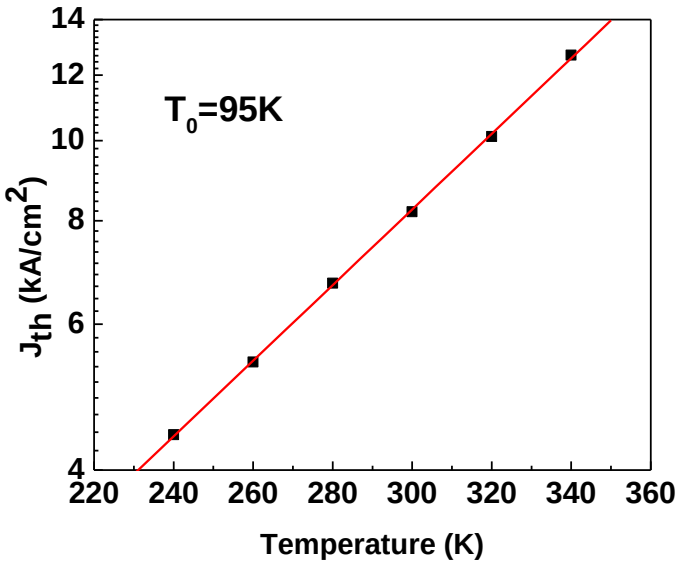

Figure 4.11: Threshold current density vs. operating temperature for a 2mm-long, 20µm-wide device fabricated from MR2784. The linear fit yields a value for the characteristic temerature, T_0 of 95K.

MR2785

As discussed in section 4.4.1, MR2785 retains the cladding layer structure of MR2784 but has a modified active region, the details of which were also described earlier in the chapter. L-I curves for a 3mm-long 20µm-wide laser are shown in figure 4.12, with the associated dependence of threshold current density on operating temperature presented in figure 4.13.

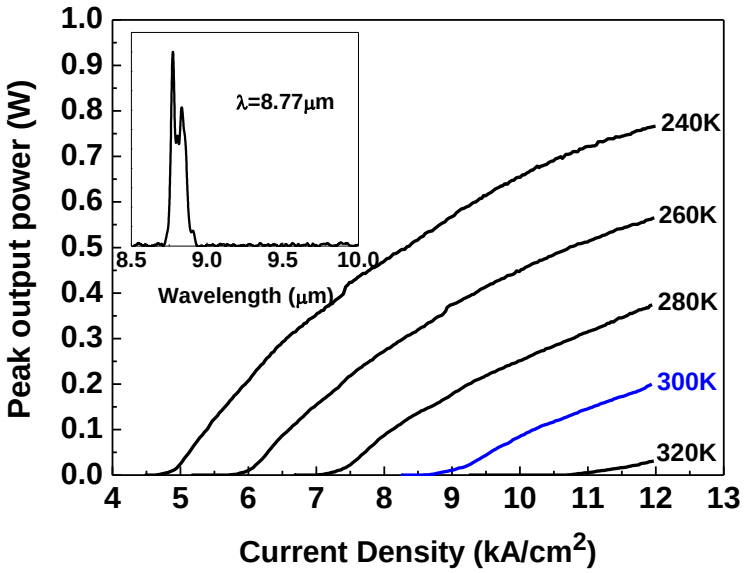

Figure 4.12: Peak output power vs. drive current for a 3mm-long 20μm-wide device fabricated from wafer MR2785. Inset: High-resolution (0.5cm^{-1}) spectra showing emission at 8.77μm.

Despite the redesigned active region of MR2785, no performance enhancements are observed when compared to devices fabricated from wafer MR2784. Threshold current densities of 4.7kA/cm^2 and 8.6kA/cm^2 are observed at 240K and 300K respectively - consistent within experimental uncertainty to those observed for MR2784 at the same temperatures. A 2mm-long device exhibits similar threshold currents of 4.9kA/cm^2 and 9.2kA/cm^2 at 240K and 300K respectively. Optical output powers are reduced - the maximum peak power observed being 1.23W at 240K for a 2mm-long device, which decreased to 0.36W at 300K. As seen in figure 4.12 above, this reduction in power is also observed in the longer laser. It would appear from this general reduction in device performance that the redesigned active region has resulted in a decreased electron population inversion that outweighs the larger dipole matrix element associated with the more vertical optical transition. This reduced population inversion has subsequently led to a reduction in intersubband gain and the observed performance reductions for MR2785. Characteristic temperatures extracted from J_{th} vs. T data yield T_0=96±15K for the 3mm laser and T_0=93±14K for the 2mm device (see figure 4.13).

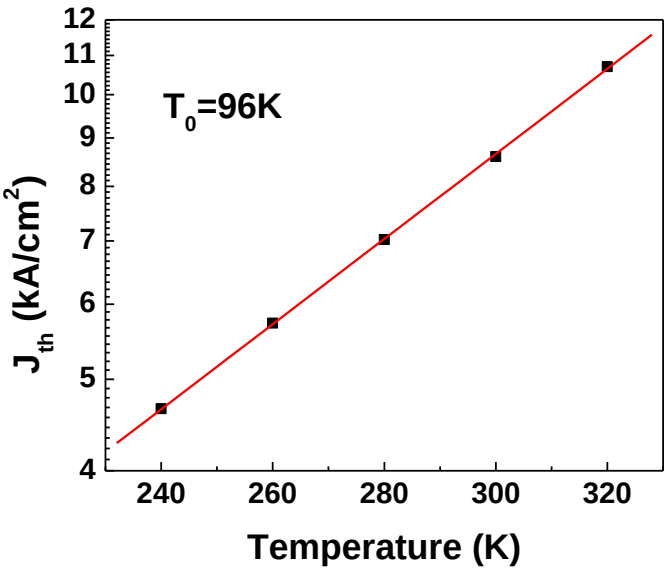

Figure 4.13: Threshold current density vs. operating temperature for a 3mm-long, 20µm-wide device fabricated from wafer MR2785 showing a characteristic temerature, T_0 of 96K.

MR2789

The performance data presented for devices fabricated from wafers MR2784 and MR2785 illustrates the effect that a redesigned active region can have on the operation of QCLs that share a common waveguide structure. However as has been discussed, an additional approach to performance enhancement involves altering the waveguide design itself, in order to increase optical confinement and decrease losses. As discussed above, wafer MR2789 reproduces the core region design outlined for MR2785, but replaces the InGaP waveguide with an InAlP layer in an attempt to exploit the potential increase in optical confinement that is theoretically possible with this material system.

Optical characteristics for a 3mm-long, 20µm-wide device can be seen in figure 4.14. As expected, the emission wavelength is close to that observed for MR2785 - 8.68µm compared to 8.77µm previously. The threshold current densities however, show a marked reduction when compared to devices fabricated from wafer MR2785. At 240K a threshold current density of J_{th}=3.8kA/cm^2 is observed, rising to J_{th}=7.3kA/cm^2 at 300K, while a 2mm-long device displayed threshold currents of J_{th}=3.6kA/cm^2 and J_{th}=7.2kA/cm^2 at 240K and 300K respectively.

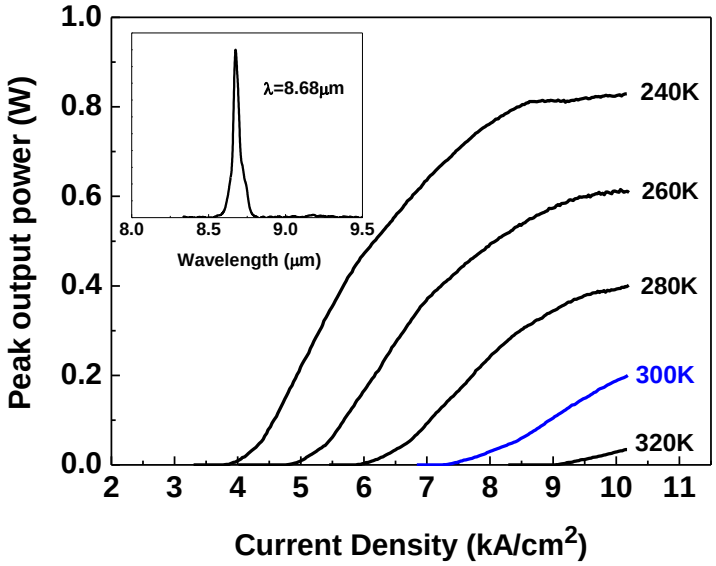

Figure 4.14: Peak output power vs. drive current for a 3mm-long 20μm-wide device based on wafer MR2789. Inset: High-resolution spectra showing emission at 8.68μm.

A peak optical output power of 0.83W was measured for the 3mm-long device at 240K, falling to 0.20W at 300K, with the 2mm device displaying powers of 0.77W and 0.22W at 240K and 300K respectively. A direct comparison of the output powers for MR2785 and MR2789 is difficult due to the lower maximum current density at which the devices based on MR2789 were run - ~10kA/cm^2 compared to ~15kA/cm^2 in the case of 2mm-long lasers. This reduction was an attempt to mitigate the strong heating effects produced by abnormally high operating voltages that resulted in a very high incidence of device failure (see discussion later in this chapter). It can be seen however that in the case of 2mm-long devices, an approximately 40% reduction in maximum drive current results in a corresponding 40% reduction in peak output power, while a smaller ~15% decrease for the 3mm-long laser leads to an almost identical power to its 3mm counterpart from wafer MR2785. It can be surmised therefore that output powers are at least unaffected by the introduction of the InAlP waveguide, and may be enhanced in comparison. The maximum temperature of operation was 320K for both devices, similar to MR2785, while characteristic temperatures of 93±14K and 87±12K for the 3mm and 2mm laser respectively were calculated from the usual exponential fit of J_{th} vs. T (see figure 4.15).

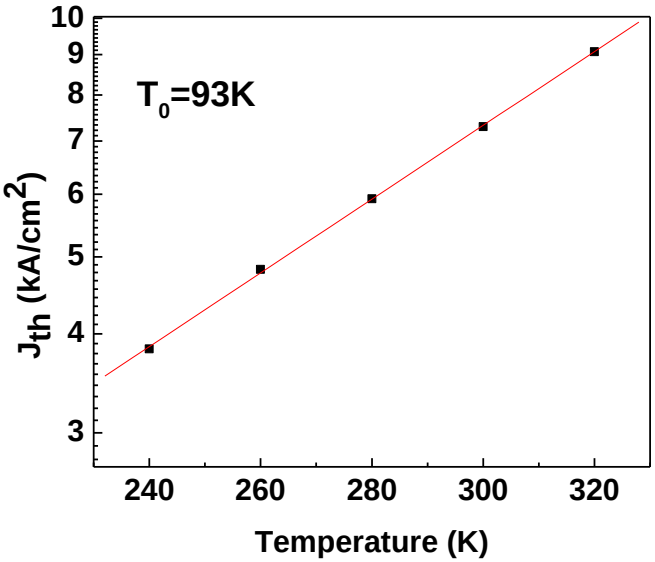

Figure 4.15: Threshold current density vs. operating temperature for a 3mm-long, 20µm-wide device based on wafer MR2789, yielding a characteristic temerature, T_0 of 93K.

It is clear that the addition of the InAlP waveguide with this particular core region design results in significant improvements in device threshold current density. Assuming that the material gain G_p remains unchanged between the two designs, this is consistent with the modified waveguide introducing both lower waveguide losses and a greater confinement of the optical mode within the active region, upon both of which J_{th} is dependent (see equation 3.4). Other performance characteristics of MR2789 - for example the peak output power - are at least comparable with the devices incorporating InGaP waveguides, and would suggest there is scope for further improvements in device design, especially in relation to the vertical transition active region, the disadvantages of which were evident in the performance of devices based on sample MR2785.

MR2790

With the InAlP waveguide of MR2789 proving effective at reducing device threshold current, the double-phonon active region incorporated into wafer MR2790 would allow a comparison in performance to be made between devices with an identical waveguide structure but differing core regions, as was the case with MR2784 and MR2785. Optical performance data for a 20µm-wide, 2mm-long device is shown in figure 4.16. It is seen immediately that the threshold current density has been further reduced compared to devices based upon wafer MR2789, which has a single phonon resonance active region. At 240K and 300K respectively, a threshold current density of J_{th}=2.2kA/cm^2 and J_{th}=4.4kA/cm^2 is observed, which is extremely low for a GaAs/AlGaAs QCL regardless of waveguide or core region design[16]. A room temperature peak output power of 0.16W increases to 0.57W as the temperature is lowered to 240K, while the maximum temperature of operation is found to be 330K. In addition to the double-phonon relaxation afforded by the extra quantum well of the active region, the larger dipole matrix element of the optical transition (z_{ij}=3.3nm) may also contribute to the improved performance seen for this device. Unlike devices based on MR2785, the decreased population inversion that would normally accompany the more vertical transition used in the active region of device MR2790, may be offset by the shorter electron lifetimes of the lower laser levels provided by the double phonon active region.

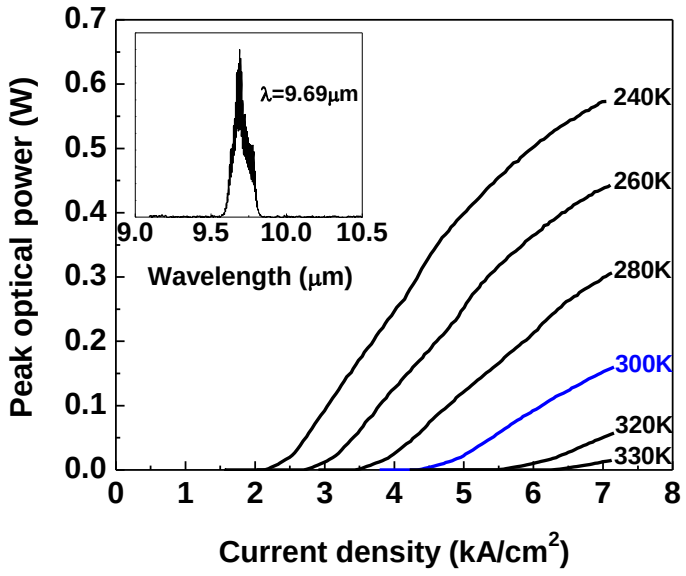

Figure 4.16: Peak output power vs. drive current for a 2mm-long 20µm-wide device based on wafer MR2790. Inset: High-resolution spectra showing emission at 9.69µm.

A device with a 3mm cavity length displayed threshold current densities of J_{th}=2.1kA/cm^2 at 240K and J_{th}=4.0kA/cm^2 at 300K. These threshold currents observed for sample MR2790 represent the lowest reported to-date for a GaAs-based QCL, and enhance the prospects of eventual room-temperature CW operation.

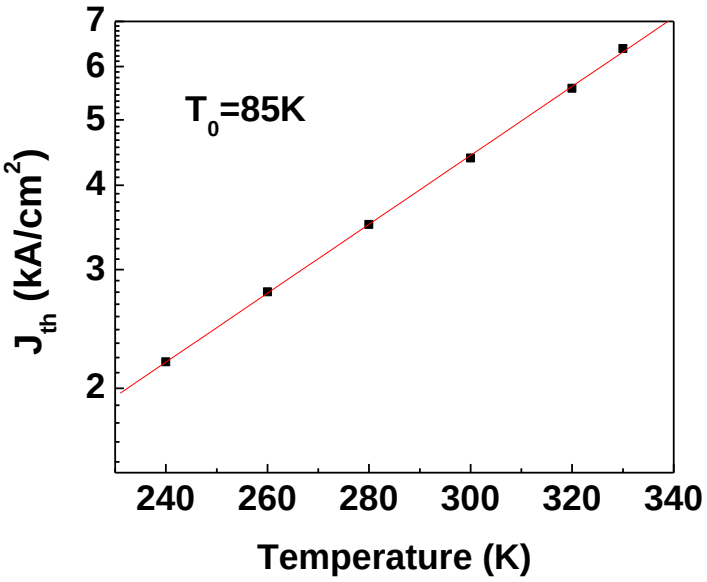

Figure 4.17: Threshold current density vs. operating temperature for a 2mm-long, 20µm-wide device based on wafer MR2790, with corresponding characteristic temerature, T_0= 85K.

The J_{th} vs. T fit for the 2mm device yields T_0=85±9K (figure 4.17), while the waveguide losses, α_w for wafer MR2790 were estimated from a linear fit of the threshold current density versus reciprocal cavity length data as outlined by equations 3.6 and 3.7 in chapter three. Figure 4.18 shows data for a series of devices of length 1mm, 2mm and 3mm, which results in a calculated waveguide loss of α_w=7.9±1.8cm^{-1} at 240K and α_w=9.6±1.2cm^{-1} at room temperature. The inconsistency between the measured waveguide loss at 300K, and the theoretical value estimated for this structure from the optical mode profile (see table 4.1) could be due to variations in the doping of the wafer layers or the parameters used in the calculation being generally applicable to lower temperatures. The data presented in figure 4.18 also allows the calculation of the modal gain coefficient $g\Gamma$, i.e. the gain coefficient g, multiplied by the waveguide confinement factor Γ (see section 3.4.4). The value of Γ for the waveguide structure of MR2790 at a wavelength of λ=9.69µm was calculated to be Γ=0.78, resulting in an

estimate of g=7.7±1.2cmkA^{-1} and g=4.4±0.4cmkA^{-1} at 240K and 300K respectively for this sample. The peak material gain at threshold G_p, can also be calculated for these devices from the relationship $G_p=gJ_{th}$ (see equation 3.4), resulting in G_p=17±3cm^{-1} and G_p=16±3cm^{-1} for the 2mm and 3mm devices respectively at 240K, while at 300K G_p=19±3cm^{-1} and G_p=18±2cm^{-1} for 2mm and 3mm lasers.

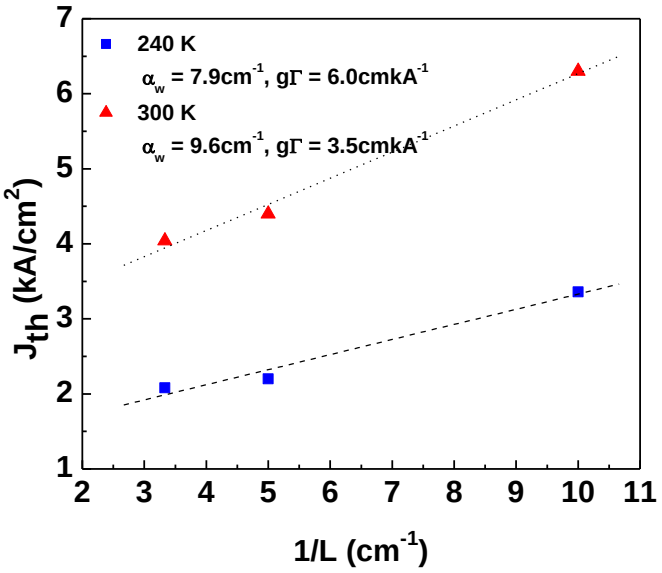

Figure 4.18: Threshold current density vs. reciprocal cavity length for 1, 2 and 3mm-long devices at an operating temperature of 240K and 300K. The linear fit yields values for the waveguide loss α_w for devices fabricated from wafer MR2790.

The measured gain coefficients can be compared to those determined for other GaAs-based devices operating at λ~9µm. Barbieri et al[17] and Sirtori et al[7] studied devices with a three-well GaAs/$Al_{0.33}Ga_{0.67}As$ active region utilising a diagonal electronic transition, and reported coefficients of g=6.7cmkA^{-1} and g=8.7cmkA^{-1} respectively. A second study by Sirtori et al[9] observed an increased gain coefficient of g=15.8cmkA^{-1} for a similar GaAs/$Al_{0.33}Ga_{0.67}As$ device with a highly-doped GaAs waveguide. In all these cases the optical confinement afforded by the device waveguides (either $Al_{0.9}Ga_{0.1}As$ or GaAs) was considerably lower than the Γ=0.78 calculated for MR2790, with confinement factors ranging between $0.31 \leq \Gamma \leq 0.42$. Higher optical confinement would have naturally lead to an increased gain coefficient. Reported waveguide losses were also correspondingly larger than those calculated here, with α_w≈20cm^{-1} being measured in all cases. The gain coefficient measured for MR2790 is consistent with

those measured in references [7] and [17], but is approximately half that reported by Sirtori et al in reference [9]. It should be noted however, that the temperature at which *g* was determined was 77K in the case of the Sirtori studies and 200K for Barbieri et al, in comparison to 240K and 300K for sample MR2790.

Since the optical confinement afforded by the InAlP waveguide of MR2790 is already considerably larger than that provided by either $Al_{0.9}Ga_{0.1}As$ or highly-doped GaAs waveguides (with correspondingly lower losses), the results of Sirtori et al suggest that there may be scope for increasing the gain of the GaAs devices presented in this chapter through alterations to the device active region. For example, the fact that there were observed reductions in performance when moving from the diagonal transition of MR2784 to the more vertical design of MR2785, means it may be possible to reduce the spatial overlap of the optical transition of MR2790 and still experience the benefit of increased gain due to the larger population inversion between upper and lower states that would result (see equation 2.4). As shown by equation 3.4, any increase in *g* that could be achieved would lead to further reductions in the threshold current density of devices (assuming waveguide losses remain the same), and would enhance the prospect of operation at high duty cycles and in the CW regime.

4.6.3 Current -Voltage Characteristics

In addition to the optical characteristics of devices fabricated from each wafer design, electrical performance, in the form of voltage-current curves were also measured for each laser. Shown in figure 4.19 is the I-V data for 3mm-long, 20µm-wide devices at liquid nitrogen (~77K) and room temperature. Upon inspection, a marked difference between the electrical performance of devices utilising either InGaP or InAlP waveguides is immediately apparent. Devices with the InGaP waveguide structure show I-V characteristics which are fairly typical for a GaAs-based QCL at both room and low temperature, where voltages approach ~13.5V and ~16V at 293K and 77K respectively. This is consistent with the expected operating voltage V_{op}, which can be estimated simply by multiplying the total transition energy of the device active region by the number of periods within in the core i.e.:

$$V_{op} \sim \left[N_p(E_\lambda + \Delta E_V)\right]/e \tag{4.1}$$

where N_P is the number of core region periods, E_λ is the emission energy in eV, and ΔE_V is the voltage defect, i.e. the energy separation between the lower laser level of one active region and the upper laser level of the next active region[18].

For devices containing InAlP waveguides however, the situation is very different. Operating voltages are dramatically increased compared to InGaP lasers, with voltages reaching in excess of 55V for devices from both wafers MR2789 and MR2790 at 77K. At room temperature, voltages are approximately double that of InGaP devices where they approach ~30V and 25V for MR2789 and MR2790 respectively. These voltages invariably lead to an excessive amount of heating within devices, and thus contributed to a high incidence of device failure.

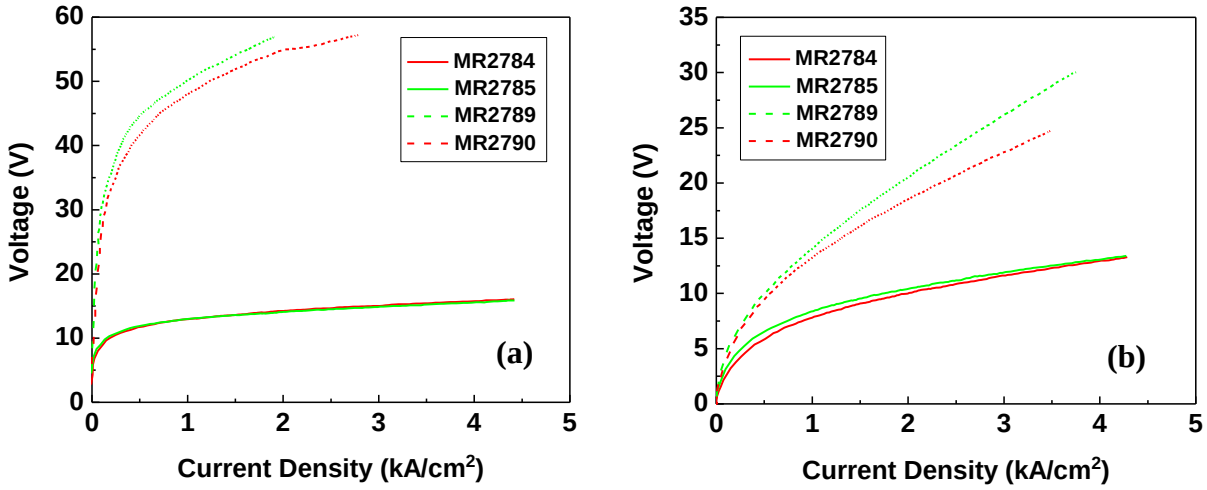

Figure 4.19: I-V characteristics for devices MR2784 through MR2790 at (a) 80K and (b) room-temperature.

The large operating voltages observed imply that either the InAlP layer itself represents a fundamental obstacle to the current flow in these devices, or that the transitional layers inserted at the GaAs/InAlP interfaces were not sufficiently optimised for efficient electron transport across the interfaces. In order to test the latter suggestion, a wafer was grown in which the transitional layer was modified by excluding the

$In_{0.49}(Ga_{0.5}Al_{0.5})_{0.51}P$ section and replacing it with InGaP, resulting in a single layer of $In_{0.49}Ga_{0.51}P$ 42nm in thickness. The remainder of the structure was identical to MR2790, including the double-phonon active region. A comparison of the I-V characteristics for a 2mm-long, 20µm-wide device fabricated from wafer MR2790 and a 2mm, 30µm-wide laser fabricated from the modified wafer can be seen in figure 4.20.

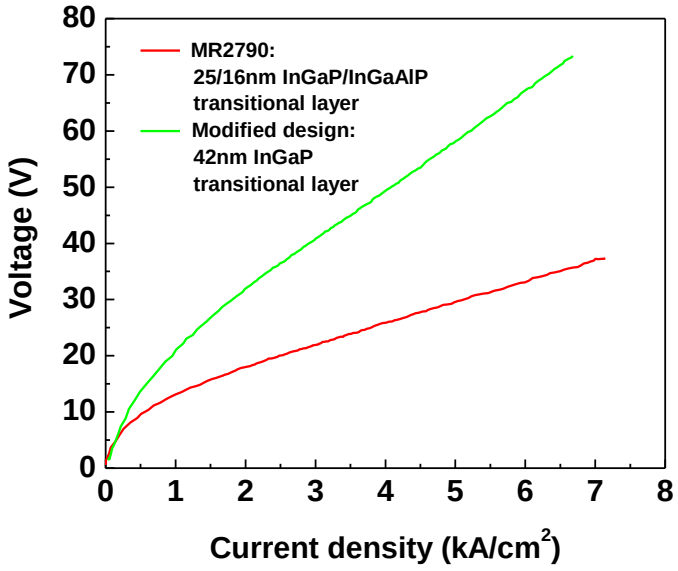

Figure 4.20: Room-temperature I-V characteristics comparing the electrical performance of device MR2790 with that of a device with a modified transitional layer (TL) at the GaAs/InAlP interface. The modification consists of removing the InGaAlP part of the TL in MR2790 and replacing it with InGaP, resulting in a TL comprising of 42nm of InGaP.

It is apparent that the removal of $In_{0.49}(Ga_{0.5}Al_{0.5})_{0.51}P$ from the transitional layer has an adverse affect on the operating voltage of this device, where at threshold (~4.4kA/cm^2) a voltage of 53V is observed, rising to over 70V at 6.7kA/cm^2. This is approximately double the voltage observed for MR2790 which includes $In_{0.49}(Ga_{0.5}Al_{0.5})_{0.51}P$ in the transitional layer at the GaAs/InAlP interface. It is not possible to state how optimised the previous structure was in terms of device operating voltage, but the result does suggest that at the least there is considerable scope for further tailoring of the layers at the GaAs/InAlP interfaces, along with the possibility of reducing operating voltages.

Despite the large operating voltages, the optical performance of lasers fabricated from the modified wafer was found to be largely comparable to that of MR2790. The characteristic temperature for the modified device was found to be T_0=82K - slightly lower than the 85K of MR2790 - while higher threshold current densities of 2.7kA/cm^2 and 5.4kA/cm^2 were observed at 240K and 300K respectively. Peak output powers of 0.72W at 240K and 0.24W at 300K were also measured, a slight increase to those recorded for MR2790.

Shown below in table 4.3 is a summary of the key performance parameters for devices fabricated from each wafer:

Sample	λ_{300K} **(μm)**	J_{th} **(kA/cm^2)**	**Peak Power (W)**	V_{max} **(V)**	T_0 **(K)**	T_{max} **(K)**
MR2784 2mm	9.08	4.4 (240K) 8.2 (300K)	1.58 (240K) 0.56 (300K)	13.5 (300K) 16 (80K)	95	340
MR2785 3mm	8.77	4.7 (240K) 8.6 (300K)	0.77 (240K) 0.20 (300K)	13.5 (300K) 16 (80K)	96	320
MR2789 3mm	8.68	3.8 (240K) 7.3 (300K)	0.83 (240K) 0.20 (300K)	30 (300K) 57 (80K)	93	320
MR2790 2mm	9.69	2.2 (240K) 4.4 (300K)	0.57 (240K) 0.16 (300K)	25 (300K) 57 (80K)	85	330

Table 4.3: Performance summary of key characteristics for devices MR2784 through MR2790.

4.7 Conclusions

This chapter has presented the optical and electrical characteristics of several GaAs-based QCLs each with differing designs, in order to ascertain the performance benefits (or otherwise) of each design strategy. It has been shown – in the case of QCLs utilising InGaP waveguides – how an increase in the number of active region periods may beneficially affect the interaction of the optical mode with the laser core and lead to an increase in device output power. It is also seen how in some cases, altering the active region to change the spatial characteristics of the optical transitions - in this case from the diagonal transition of MR2784 to the more vertical of MR2785 - can have an adverse effect on laser performance if the correct balance is not found between the increased dipole matrix element and the reduced population inversion that results. The performance reductions that were observed for sample MR2785 however, can be mitigated by the substitution of a waveguide material that has the potential for greater optical confinement and lower optical losses than that offered by InGaP. The enhancements in performance observed for MR2789 can be attributed to the introduction of the InAlP waveguide since the design is otherwise identical to MR2785. The benefit of a double-phonon active region has also been demonstrated, with threshold current densities as low as 2kA/cm^2 and 4kA/cm^2 having been observed at 240K and 300K respectively for MR2790 – the lowest J_{th} for a GaAs-based QCL at these temperatures reported to-date. Other performance characteristics such as peak output power are at least comparable with other GaAs-based devices, confirming the potential for further performance enhancements of QCLs that incorporate InAlP as the waveguide material.

Despite these successes, it has also been shown that InAlP can introduce characteristics detrimental to device performance. The high operating voltages observed in lasers with InAlP waveguides are a major cause of device failure, and will almost certainly inhibit any attempt to run devices at higher duty cycles. Optimisation of the transitional layers at the GaAs/InAlP interfaces is one strategy that may reduce these voltages, and this approach will form the main focus of the next chapter. If the low threshold current densities that are characteristic of devices with InAlP waveguides, can be combined with the lower operating voltages and improved characteristic temperatures associated with devices with InGaP waveguides, it may enhance the prospects for CW operation of

GaAs-based QCLs at higher temperatures than have previously been achieved – 150K at the time of writing[11].

1. L. R. Wilson, P. T. Keightley, J. W. Cockburn, J. P. Duck, M. S. Skolnick, J. C. Clark, G. Hill, M. Moran and R. Grey, *Spectroscopic determination of the electron distribution in a quantum cascade structure*, Applied Physics Letters, **75**, 2079-2081, (1999).

2. J. S. Roberts, R. P. Green, L. R. Wilson, E. A. Zibik, D. G. Revin, J. W. Cockburn and R. J. Airey, *Quantum cascade lasers grown by metalorganic vapor phase epitaxy*, Applied Physics Letters, **82**, 4221-4223, (2003).

3. R. P. Green, L. R. Wilson, D. A. Carder, J. W. Cockburn, M. Hopkinson, M. J. Steer, R. J. Airey and G. Hill, *Room temperature GaAs-based quantum cascade laser with GaInP waveguide cladding*, Electronics Letters, **38**, 1539-1541, (2002).

4. L. R. Wilson, P. T. Keightley, J. W. Cockburn, J. P. Duck, M. S. Skolnick, J. C. Clark, G. Hill, M. Moran and R. Grey, *Mid-infrared spectroscopic studies and lasing in GaAs-AlGaAs quantum cascade devices*, Physica E, **7**, 713-717, (2000).

5. L. R. Wilson, P. T. Keightley, J. W. Cockburn, M. S. Skolnick, J. C. Clark, R. Grey and G. Hill, *Controlling the performance of GaAs-AlGaAs quantum-cascade lasers via barrier height modifications*, Applied Physics Letters, **76**, 801-803, (2000).

6. A. B. Krysa, D. G. Revin, J. P. Commin, C. N. Atkins, K. Kennedy, Y. Qiu, T. Walther and J. W. Cockburn, *Room-Temperature GaAs/AlGaAs Quantum Cascade Lasers Grown by Metal-Organic Vapor Phase Epitaxy*, Ieee Photonics Technology Letters, **23**, 774-776, (2011).

7. C. Sirtori, P. Kruck, S. Barbieri, P. Collot, J. Nagle, M. Beck, J. Faist and U. Oesterle, *GaAs/$Al_xGa_{1-x}As$ quantum cascade lasers*, Applied Physics Letters, **73**, 3486-3488, (1998).

8. C. Sirtori, S. Barbieri, P. Kruck, V. Piazza, M. Beck, J. Faist, U. Oesterle, P. Collot and J. Nagle, *Influence of DX centers on the performance of unipolar semiconductor lasers based on GaAs-$Al_xGa_{1-x}As$*, IEEE Photonics Technology Letters, **11**, 1090-1092, (1999).

9. C. Sirtori, P. Kruck, S. Barbieri, H. Page, J. Nagle, M. Beck, J. Faist and U. Oesterle, *Low-loss Al-free waveguides for unipolar semiconductor lasers*, Applied Physics Letters, **75**, 3911-3913, (1999).

10. H. Page, S. Dhillon, M. Calligaro, V. Ortiz and C. Sirtori, *Optimised device processing for continuous-wave operation in GaAs-based quantum cascade lasers*, Electronics Letters, **39**, 1053-1055, (2003).

11. H. Page, S. Dhillon, M. Calligaro, C. Becker, V. Ortiz and C. Sirtori, *Improved CW operation of GaAs-Based QC lasers: T-max=150 K*, Ieee Journal of Quantum Electronics, **40**, 665-672, (2004).

12. H. Page, C. Becker, A. Robertson, G. Glastre, V. Ortiz and C. Sirtori, *300 K operation of a GaAs-based quantum-cascade laser at $\lambda \sim 9\mu m$*, Applied Physics Letters, **78**, 3529-3531, (2001).

13. S. Adachi, *Properties of Semiconductor Alloys*, (Wiley, 2009).

14. Q. Yang, R. Losch, W. Bronner, S. Hugger, F. Fuchs, R. Aidam and J. Wagner, *High-peak-power strain-compensated GaInAs/AlInAs quantum cascade lasers (λ~4.6μm) based on a slightly diagonal active region design*, Applied Physics Letters, **93**, 251110, (2008).

15. M. O. Watanabe and Y. Ohba, *Interface properties for GaAs/InGaAlP heterojunctions by the capacitance-voltage profiling technique*, Applied Physics Letters, **50**, 906-908, (1987).

16. C. N. Atkins, A. B. Krysa, D. G. Revin, K. Kennedy, J. P. Commin and J. W. Cockburn, *Low threshold room temperature GaAs/AlGaAs quantum cascade laser with InAlP waveguide*, Electronics Letters, **47**, 1193-1194, (2011).

17. S. Barbieri, C. Sirtori, H. Page, M. Beck, J. Faist and J. Nagle, *Gain measurements on GaAs-based quantum cascade lasers using a two-section cavity technique*, IEEE Journal of Quantum Electronics, **36**, 736-741, (2000).

18. R. Maulini, A. Lyakh, A. Tsekoun and C. K. N. Patel, *λ~7.1μm quantum cascade lasers with 19% wall-plug efficiency at room temperature*, Optics Express, **19**, 17203-17211, (2011).

Chapter Five

Design Optimisation for GaAs-based QCLs with InAlP Waveguides

5.1 Introduction

Chapter four included a discussion of the excessive operating voltages measured for QCLs incorporating InAlP waveguides, and how these voltages led to a high incidence of device failure - partly negating the performance gains otherwise observed. It was suggested that the source of these high voltages was the comparatively large conduction-band offset at the GaAs/InAlP interfaces within the device structure, which would inhibit electron flow through devices at these points. This challenge had, to some extent, been anticipated when designing the QCLs presented in chapter four, and led to the introduction of the InGaP/InGaAlP transitional layers between the GaAs/InAlP interfaces. For the next iteration of wafer design it was decided that a more sophisticated approach to managing the GaAs/InAlP interfaces should be taken in an attempt to further reduce operating voltages.

This chapter will consist of a discussion of two new designs for the transitional layers that bridge the GaAs/InAlP interfaces within a series of four GaAs-based QCL wafers with InAlP waveguides. These new designs increase the complexity of the layer structure at the GaAs/InAlP interfaces and are detailed in section 5.2. Two of the wafers reproduce the cladding layer and core-region structure of wafer MR2790 from chapter four, but incorporate one or other of the new transitional layers in order to observe their effect on device operating voltage. The remaining two wafers also include one of the transitional layers, but have a modified core region which includes several high-

aluminium $Al_{0.75}Ga_{0.25}As$ barriers in the injector region, the addition of which represent an attempt to reduce the probability of electron escape from the upper laser level into the electronic states that exist above the injector region barriers. This non-radiative electron pathway can act to decrease population inversion within the device active region and thus compromise device performance - especially at higher temperatures. This strategy of selectively including high-Al fraction barriers within the QCL core region has been implemented in several previous studies[1-3]. For example, Yang and co-workers[4] replaced the standard AlInAs exit barrier of an InGaAs/AlInAs QCL active region with an AlAs 'blocking barrier' in order to increase the conduction band offset relative to the preceding quantum well. Consequent improvements in device performance included a 30K increase in maximum operating temperature and threefold increase in output power, both of which were attributed to the increased confinement of electrons in the upper energy level and subsequent reduction of non-radiative tunnelling into continuum states. As well as the addition of high-Al barriers, various changes to well and barrier widths throughout the core region have been made. The full design details of each wafer are given in the next section. Following the discussion of wafer design, the electrical and optical characteristics of devices fabricated from each wafer are presented, and the effects on device performance produced by the various different design strategies will be compared.

5.2 Wafer Design

MR3066

The layer sequence for wafer MR3066 (shown schematically in figure 5.1) closely follows that of MR2790 outlined in chapter four, with the exception of the modified transitional layers that now occupy the GaAs/InAlP interfaces. Rather than the InGaP/InGaAlP layer that was used at each interface in wafers MR2789 and MR2790, the layer sequence is now dependent upon which GaAs/InAlP interface is being considered. In the case of MR3066, there are four relevant interfaces, which starting from the GaAs substrate and working in the direction of growth can be numbered 1 through 4, and the transitional layer associated with each termed TL1, TL2, TL3 and TL4 as shown in figure 5.1. TL1 comprises of 40nm InGaP (N=1x10^{18}cm^{-3}) followed by

60nm InAlP (graded N=1x10^{18} → 1x10^{17}cm^{-3}), while TL3 consists of a single 40nm thick layer of $In_{0.49}Ga_{0.51}P$ (N=1x10^{17}cm^{-3}). TL2 and TL4 are formed by a superlattice of alternating InGaP and InAlP layers, the thicknesses of which are graded so that the width of the InGaP layers increases in the growth direction, whilst the InAlP decreases in width in the same direction.

Starting from the InAlP waveguide and working in the direction of growth, the structure of the superlattice TL2 and TL4, also shown schematically in figure 5.1, is as follows: 0.6/**4.0**/0.8/**4.0**/1.0/**3.5**/1.3/**3.5**/1.5/**3.0**/2/**2.0**/2.5/**1.5**/3/**1.5**/4/**1.5**/5/**1.5**/6/**1.5**/10/**1.5**/20/*10*/ 40, where thicknesses are in nm, normal font represents $In_{0.49}Ga_{0.51}P$ layers, and bold font $In_{0.47}Al_{0.53}P$ layers. For TL2 the penultimate 10nm InGaP layer at the end of the sequence (shown in red italicised font) is omitted and all layers are Si-doped to N=1x10^{17}cm^{-3}, while for TL4 the final two layers are both doped to N=1x10^{18}cm^{-3}.

The complete layer sequence for wafer MR3066, starting from the GaAs substrate (N=3x10^{18}cm^{-3}) and including transitional layers is as follows: 1µm GaAs bottom cladding (N=3x10^{18}cm^{-3}), TL1, 3µm $In_{0.47}Al_{0.53}P$ waveguide layer (N=1x10^{17}cm^{-3}), superlattice TL2, 0.2µm GaAs spacer layer (N=5x10^{16}cm^{-3}), GaAs/$Al_{0.45}Ga_{0.55}As$ core region (55 periods, 3.041µm), 0.2µm GaAs spacer, TL3, 3µm $In_{0.47}Al_{0.53}P$ waveguide, superlattice TL4 and finally 1µm GaAs top cladding. The core region structure is a copy of the double-phonon design used in wafer MR2790, details of which are given in section 4.5 of chapter four along with the corresponding conduction band profile (figure 4.7).

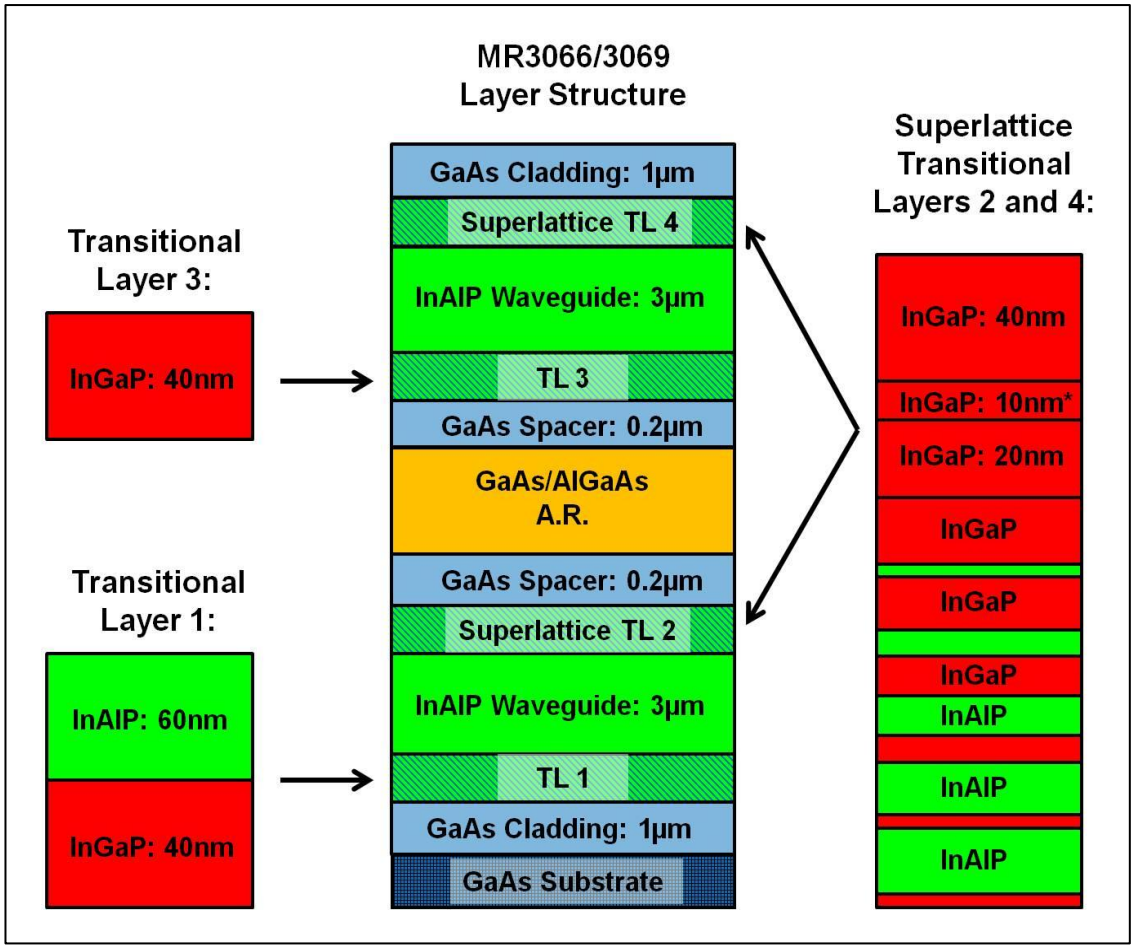

Figure 5.1: Schematic illustration of the layer structure for wafers MR3066 and MR3069, including transitional layers at the GaAs/InAlP interfaces.

MR3069

Wafer MR3069 replicates the layer sequence of MR3066, except for the inclusion of three high-aluminium $Al_{0.75}Ga_{0.25}As$ barriers in the injector region. As mentioned in the introduction above, these barriers represent an attempt to increase the high-temperature performance of devices by reducing the probability of electron escape from the upper laser level (E_u) into the higher-lying states above the injector region. For the composition x=0.75, $Al_{0.75}Ga_{0.25}As$ barriers provide an increase in conduction band offset of ~0.32eV relative to the GaAs/$Al_{0.45}Ga_{0.55}As$ offset in the remainder of the core region, while still remaining lattice matched with the GaAs quantum wells. Beginning from the injection barrier, this new core region design has the following structure:

4.2/2.1/**1.0**/5.0/**1.0**/4.9/**1.0**/4.6/**1.0**/***1.0***/3.9/***1.6***/3.7/***1.6***/3.5/**1.8**/3.2/**2.1**/2.9/**2.7**/2.9,
where normal font represents the GaAs wells, bold font the $Al_{0.45}Ga_{0.55}As$ barriers and red italicised font the $Al_{0.75}Ga_{0.25}As$ barriers. Underlined layers are Si-doped to N=4x10^{17}cm^{-3}.

In addition to the $Al_{0.75}Ga_{0.25}As$ barriers in the injector region, the core has undergone several other changes including a widening of the first active region quantum well and a narrowing of the succeeding three wells that constitute the remainder of the active region. The barriers associated with these wells have been correspondingly widened. The injector region has seen similar alterations to well and barrier thicknesses, with the majority of the quantum wells being increased in thickness, while barriers preceding the doped region of the injector have been slightly narrowed. In common with wafer MR3066, MR3069 contains the graded superlattice transitional layer detailed above. The core region conduction band profile, showing the moduli squared of the electronic wavefunctions associated with both the laser transition and the injector miniband is given in figure 5.2, where the increased conduction band offset provided by the $Al_{0.75}Ga_{0.25}As$ barriers is clearly illustrated. The alterations to the active region have also resulted in a reduction in dipole matrix element for the optical transition of z_{ij}=2.8nm, compared to z_{ij}=3.3nm for MR3066.

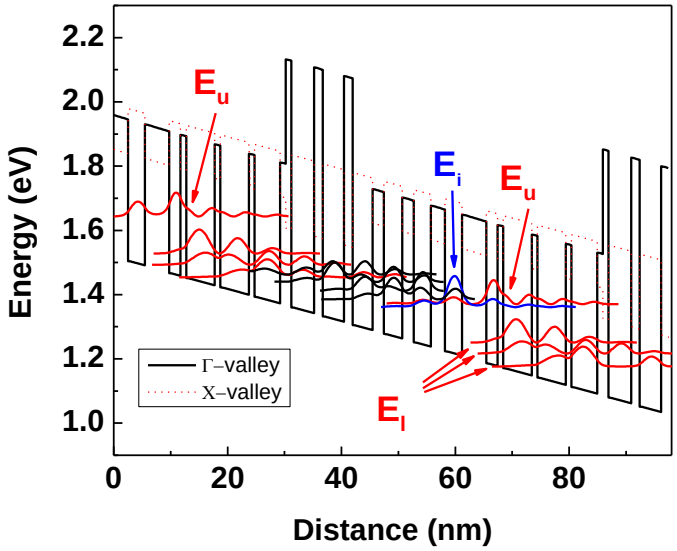

Figure 5.2: Γ-point conduction band profile for the core region of MR3069 and MR3082 under a bias of 48kV/cm^2. Also shown for reference in the X-valley profile (see discussion in section 5.3.2). The Γ-profile includes the moduli-squared of the electronic wavefunctions associated with the optical transition (shown in red), and the injector level (blue). The effect of the high-Al barriers on the conduction band offset is clearly illustrated.

MR3076

The layer structure and core region design of wafer MR3076 is a copy of MR3066, with the exception of the transitional layers 1 → 4 that appear the GaAs/InAlP interfaces. The graded superlattice design that constituted TL2 and TL4 in wafers MR3066 and MR3069, has been replaced by a 'stepped' transitional layer containing three 20nm thick sub-layers of $In_{0.49}(Ga_{1-x}Al_x)_{0.51}P$ in which the Al-fraction is sequentially reduced from $0.7 \leq x \leq 0.3$ in the direction of growth, and a final layer consisting of 40nm of $In_{0.49}Ga_{0.51}P$. The full transitional layer sequence is as follows: $In_{0.49}(Ga_{0.3}Al_{0.7})_{0.51}P/In_{0.49}(Ga_{0.5}Al_{0.5})_{0.51}P/In_{0.49}(Ga_{0.7}Al_{0.3})_{0.51}P/In_{0.49}Ga_{0.51}P$,
with layers doped to N=1x10^{17}cm^{-3} at TL2 and N=1x10^{18}cm^{-3} at TL4. Transitional layer 1 comprises of 40nm of $In_{0.49}Ga_{0.51}P$ (N=1x10^{18}cm^{-3}), 20nm of $In_{0.49}(Ga_{0.5}Al_{0.5})_{0.51}P$ (N=1x10^{18}cm^{-3}) and 60nm of $In_{0.47}Al_{0.53}P$ (graded N=1x10^{18}cm^{-3} → N=1x10^{17}cm^{-3}). Finally, transitional layer 3 is formed by a 40nm layer of $In_{0.49}Ga_{0.51}P$ followed by 20nm of $In_{0.49}(Ga_{0.5}Al_{0.5})_{0.51}P$ (both N=1x10^{17}cm^{-3}). A schematic of the layer structure for MR3076 and its associated TLs are shown in figure 5.3.

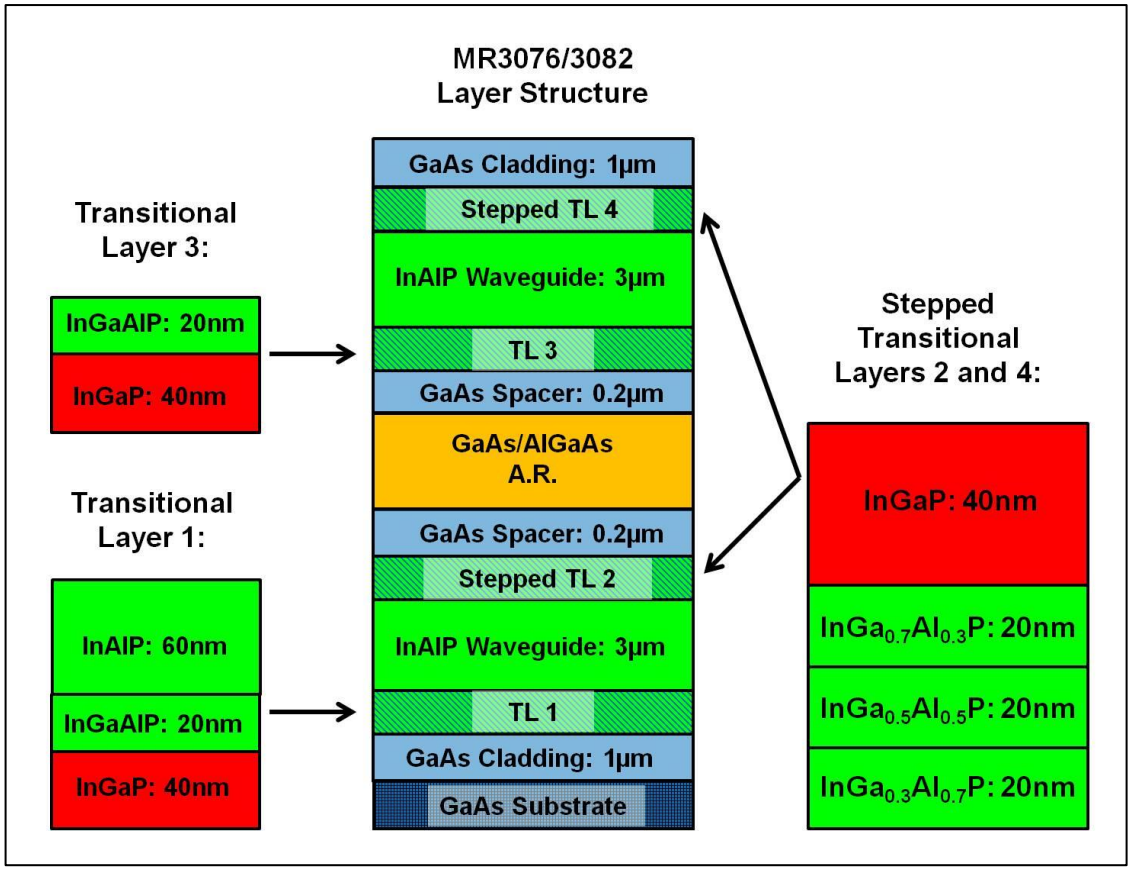

Figure 5.3: Schematic illustration of the layer structure for wafers MR3076 and MR3082, including transitional layers.

MR3082

Finally, wafer MR3082 reproduces the layer structure and transitional layers of MR3076 (see figure 5.3), while incorporating the high-aluminium core region used in MR3069, details of which can be found in the relevant section above.

In common with the previous series of wafers presented in chapter four, all wafers described above were grown using MOVPE on GaAs substrates with a 10° miscut toward the (111) plane. The growth conditions were identical throughout the run and are detailed in section 4.5 of chapter 4.

Design Summary

Table 5.1 provides a summary of the key design features of each wafer for comparison:

Wafer	Active Region Design	Transitional Layer	Waveguide Material	Γ (%) / α_w (cm^{-1})
MR3066	Double-phonon 'Vertical' transition	Superlattice InGaP/InAlP	InAlP	81 / 4.8
MR3069	Double-phonon Diagonal transition 75% Al Barriers	Superlattice InGaP/InAlP	InAlP	81 / 4.8
MR3076	Double-phonon 'Vertical' transition	Stepped InGaP/InGaAlP	InAlP	81 / 4.8
MR3082	Double-phonon Diagonal transition 75% Al Barriers	Stepped InGaP/InGaAlP	InAlP	81 / 4.8

Table 5.1: Summary outlining the main design features of each wafer.

5.3 Device Performance

After processing, wafers were cleaved into a series of 3mm-long devices with ridge widths of either 16μm or 21μm, and mounted onto T05 headers for characterisation. As with the previous series of devices presented in chapter four, all measurements were made in pulsed mode with a pulse width of 50ns and repetition rate of 5kHz.

5.3.1 Electrical Characteristics

Inclusion of the superlattice and stepped transitional layers in the new wafer designs represented an attempt to reduce the excessive operating voltages observed in the previous set of QCLs with InAlP waveguides. A series of room and low-temperature current-voltage measurements are shown in figure 5.4, contrasting the operating voltages of devices incorporating the superlattice and stepped transitional layers. Data for device MR2790 (from the previous series of lasers) is also presented for comparison.

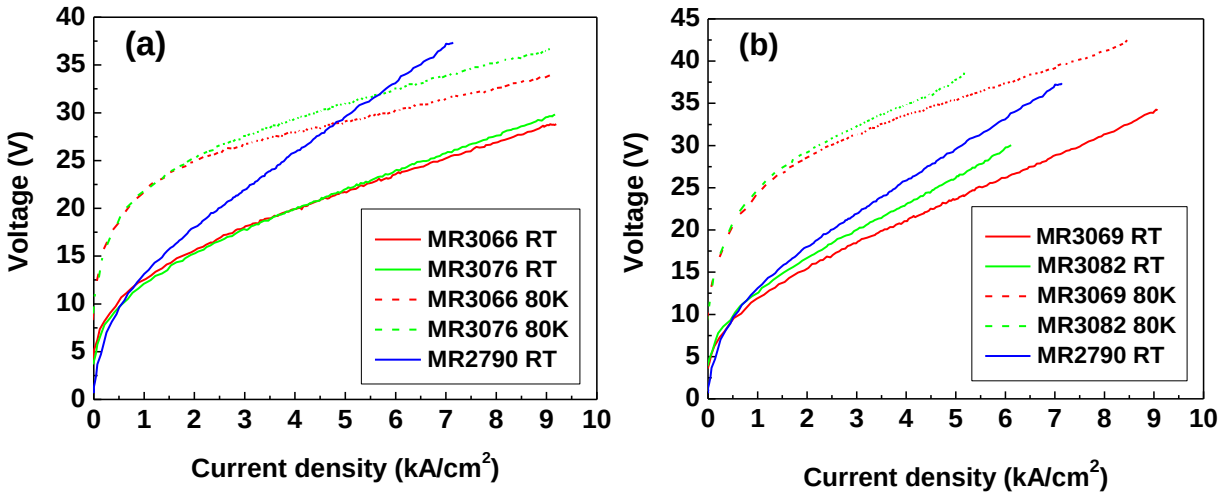

Figure 5.4: I-V characteristics for (a) devices MR3066 and MR3076 and (b) MR3069 and MR3082, at 80K and room-temperature. Shown for comparison in blue is the room-temperature I-V for device MR2790 featured in chapter four.

Figure 5.4 (a) compares the I-V characteristics for a set of 3mm-long, 16um-wide devices fabricated from wafers MR3066 (superlattice TL) and MR3076 (stepped TL) which, besides the differing TLs, have an identical layer structure and core region. It can be seen that at room temperature, only a small difference in operating voltage is observed between the two devices over the entire current range, where the voltage for MR3076 begins to diverge from MR3066 at approximately 5kA/cm^2. At threshold, both devices run at ~22V, while at maximum current density (J_{max}~9kA/cm^2) a difference of only 1V exists between the two - 29V and 30V for MR3066 and MR3076 respectively. At liquid nitrogen temperatures, the difference in operating voltage becomes slightly more pronounced, with MR3066 and MR3076 running at ~34V and ~36.5V respectively at maximum drive current.

In comparison to device MR2790 (shown in blue in figure 5.4), these voltages represent a reduction in operating voltage at room temperature of ~12V (at a comparable current of 7kA/cm^2), while at 80K reductions are even more marked. As shown in chapter four (figure 4.19), a maximum low temperature voltage of V_{max}~57V at 2.8kA/cm^2 was observed for MR2790, resulting in a significant incidence of device failure. By comparison, a V_{max} of ~35V at the same low temperature but much higher current density (~9kA/cm^2) for MR3066 and MR3076 represents a significant reduction. These voltages are still high however, when contrasted with devices MR2784 and MR2785 which incorporated InGaP waveguides and operated at ~12-15V at room and low-temperature.

The small voltage differences observed between devices with the superlattice and stepped TLs seen above, are somewhat enhanced when measuring lasers based upon wafers MR3069 and MR3082 (superlattice and stepped TLs respectively), which include $Al_{0.75}Ga_{0.55}As$ barriers in the core region. As seen in figure 5.4 (b), the room-temperature operating voltage of MR3082 shows a greater divergence from MR3069 than was observed between MR3066 and MR30776, and results in a disparity of ~4V at 6kA/cm^2 (the maximum drive current for device MR3082). At this point voltages of 30V and ~26V are measured for MR2782 and MR3069 respectively. The maximum voltage observed for device MR3069 is V_{max}~34V at 9kA/cm^2, larger than either MR3066 or MR3076 (29V and 30V respectively). Voltage at threshold is 26V for both devices, despite MR3082 having a lower threshold current density (~5kA/cm^2 compared to ~6kA/cm^2). At 80K device MR3069 is observed to run at 42V at maximum current (9kA/cm^2), compared to ~40V for MR3082 (maximum current 5kA/cm^2).

Contrasting the electrical characteristics of each device allows for certain behaviours and trends to be discerned. Firstly, at room temperature there is very little difference in the operating voltages of devices with $Al_{0.45}Ga_{0.55}As$ barriers that contain either the superlattice or stepped TLs (MR3066 and MR3076), over their entire working current range. At 80K a more obvious difference in voltage is observed between the two devices, which is more pronounced at larger currents. This disparity however, remains a relatively small 2.5V at maximum current. Any further increase in this voltage difference at higher currents is unlikely to affect the comparison since this would exceed the rollover in power output of both devices. A greater difference in room-temperature operating voltage is observed when comparing devices with $Al_{0.75}Ga_{0.25}As$

barriers, i.e. MR3069 (superlattice TL) and MR3082 (stepped TL), which at its largest reaches 3.5V at a current density of J=6kA/cm^2.

It is clear that a more marked difference in operating voltage exists if comparing devices with the same transitional layer, but either $Al_{0.45}Ga_{0.55}As$ or the higher-aluminium $Al_{0.75}Ga_{0.25}As$ barriers in the core region – i.e. MR3066 vs. MR3069 or MR3076 vs. MR3082. The largest observed voltage difference observed is ~5V at J=9kA/cm^2 between MR3066 and MR3069, although by extrapolating the voltage for MR3082 to a drive current of J=9kA/cm^2 a difference of ~10V can be estimated between this device and MR3076. If device MR3066 (superlattice TL and $Al_{0.45}Ga_{0.55}As$ barriers) is taken as the starting point for comparison, the addition of the stepped TL (MR3076) appears to introduce an additional component to the voltage drop of within the structure - a trend which is replicated between MR3069 and MR3082. An additional unexpected voltage drop then appears for the lasers with the $Al_{0.75}Ga_{0.25}As$ barriers in the core region, resulting in MR3082 (stepped TL and $Al_{0.75}Ga_{0.25}As$ barriers) running at the highest voltage. It is unclear at present why devices with high-Al barriers in the injector region should display this additional voltage. It is possible that variations in the MOVPE growth conditions have led to fluctuations in the doping, which would be particularly sensitive near the transitional layer interfaces and could affect the voltage drop across the device.

5.3.2 Optical Characteristics

MR3066

As discussed above, wafer MR3066 copies the double-phonon active region design of MR2790, while incorporating the new superlattice transitional layer. Figure 5.5 shows the light power vs. current data for a 3mm-long, 21µm-wide device, while the inset contains a high-resolution (0.25cm^{-1}) room temperature FTIR spectra showing emission at λ=10.43µm. The threshold current density for this device at 240K is 2.9kA/cm^2 rising to 5.4kA/cm^2 at 300K, while a narrower 16µm laser demonstrated threshold currents of 3.0kA/cm^2 and 5.3kA/cm^2 at 240K and 300K respectively. Peak optical output powers are found to reduce from a maximum of 0.34W at 240K to 0.08W at 300K, while the narrower device has a peak power of 0.21W at 240K and 0.08W at 300K.

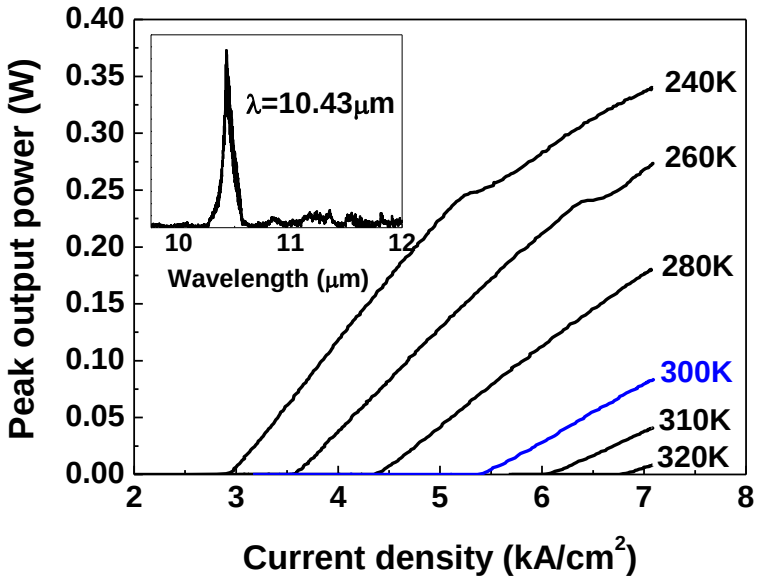

Figure 5.5: Peak output power vs. current density for a 3mm-long 21μm-wide device fabricated from wafer MR3066. Inset: High-resolution (0.25cm^{-1}) FTIR spectra showing emission at 10.43μm.

The temperature range over which devices operate is comparable with the previous series of GaAs lasers, with the 21μm and 16μm wide devices having maximum operating temperatures of 320K and 340K respectively. An exponential fit of the threshold current density versus temperature data for the 21μm device is shown in figure 5.6, and reveals a characteristic temperature of T_0=94±13K, while the 16μm wide laser exhibited T_0=102±18K.

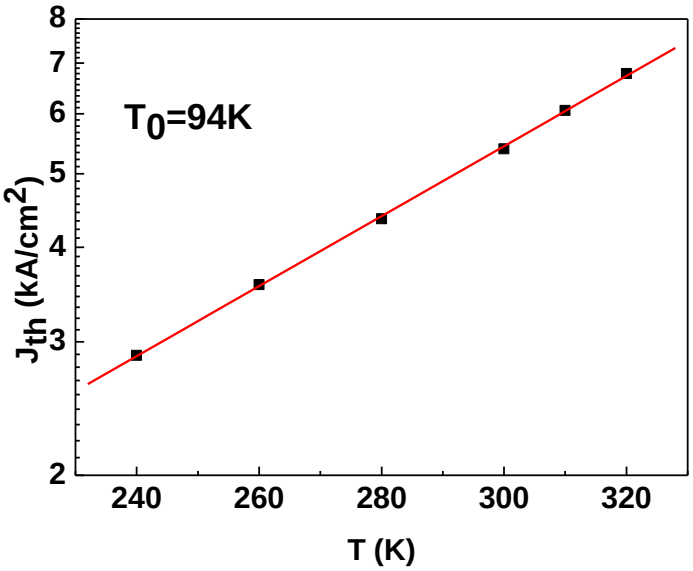

Figure 5.6: Threshold current density vs. operating temperature for a 3mm-long, 21µm-wide device fabricated from MR3066, yielding a characteristic temperature T_0=94K.

Comparing the performance of MR3066 with that of MR2790, it can be seen that the threshold current density of the former does not reach the low levels of the latter despite the retention of the InAlP waveguide. Output power is also reduced in comparison to MR2790. It is possible that the longer emission wavelength observed for device MR3066 has resulted in an increase in the optical losses associated with the waveguide structure and caused a subsequent reduction in device performance. A calculation of Γ and α_w for MR3066 at the emission wavelength of λ=10.43µm results in Γ=76% and α_w=7.5cm^{-1}, which represents a slight reduction in modal overlap compared to MR2790 (Γ=78% at λ=9.69µm) along with an increased waveguide loss (α_w=5.7cm^{-1}).

MR3076

Wafer MR3076 retains the core region and cladding design of MR3066, but replaces the superlattice transitional layer with the stepped InGaP/InGaAlP design outlined above. As expected, the emission wavelength of λ=10.40µm (inset to figure 5.7) is almost identical to that of MR3066. Other performance characteristics are detailed in figures 5.7 and 5.8, and show several variations when compared to devices based on MR3066.

A 3mm-long, 16µm-wide device demonstrated a threshold current density of J_{th}=2.7kA/cm^2 at 240K, while a 21µm device exhibited an almost identical J_{th}=2.8kA/cm^2. At 300K, the threshold current density rises to 5.1kA/cm^2 and 5.2kA/cm^2 for 16µm and 21µm-wide lasers respectively. As was the case for MR3066, these current densities fail to match the low J_{th} observed for MR2790; J_{th}=2.1kA/cm^2 and 4.0kA/cm^2 at 240K and 300K respectively.

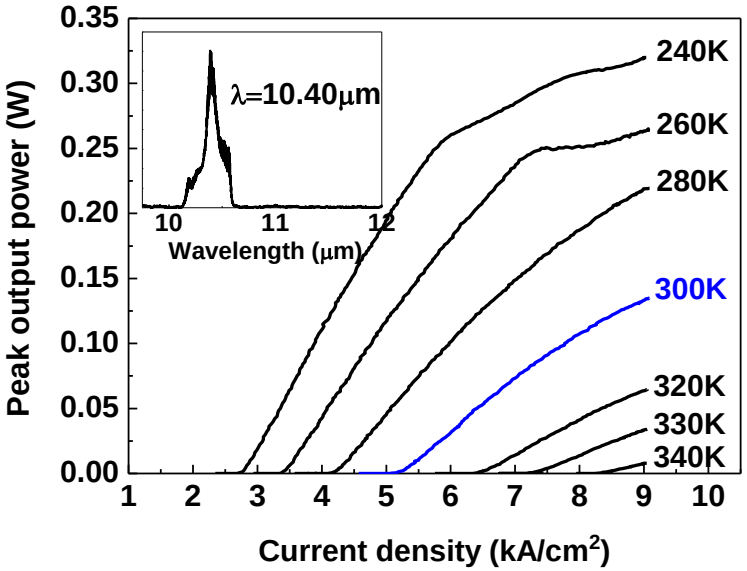

Figure 5.7: Peak output power vs. current density for a 3mm-long, 16µm-wide device fabricated from wafer MR3076. Inset: High-resolution spectra.

Peak optical output powers for the 16µm-wide device were found to be 0.32W at 240K, falling to 0.13W at 300K, while the wider 21µm laser produced almost identical powers at these temperatures. As was observed for MR3066, maximum operating temperatures of 340K and 320K for 16µm and 21µm devices respectively were measured. The characteristic temperatures of T_0=95±16K (figure 5.8) and T_0=93±15K for 16µm and 21µm devices respectively are consistent with those measured for MR3066.

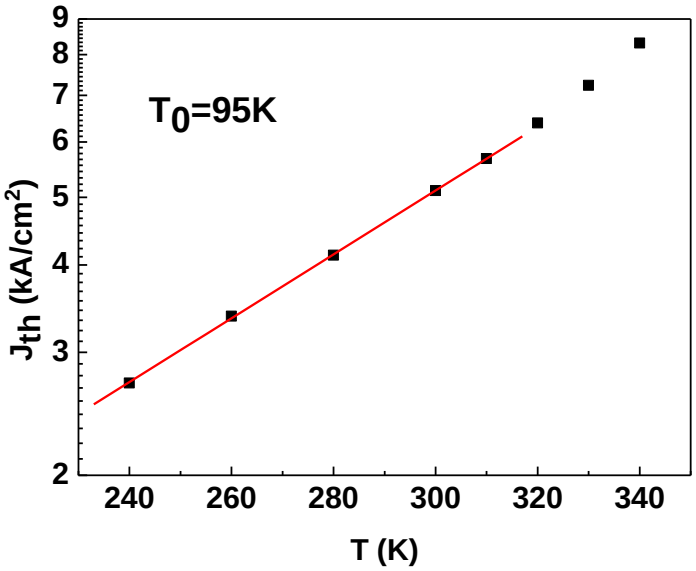

Figure 5.8: Threshold current density vs. operating temperature for a 3mm-long, 16µm-wide device fabricated from MR3076, yielding T_0=95K.

MR3069

While having the same superlattice transitional layer as MR3066, wafer MR3069 incorporates high-Al $Al_{0.75}Ga_{0.25}As$ barriers in the injector region, along with a correspondingly modified active region. L-I curves for a 3mm-long, 16m-wide device are shown in figure 5.9, with values of J_{th}=3.6kA/cm^2 and J_{th}=6.0kA/cm^2 being measured at 240K and 300K respectively. Almost identical threshold currents are observed for 21µm-wide devices. A peak output power at 240K of 0.36W represents an increase of ~0.15W compared to MR3066, while at 300K output powers remain unchanged at P≈0.09W. The emission wavelength of λ=10.49µm shown in the inset to figure 5.9 is consistent with that of MR3066, while the maximum temperature of operation is seen to reduce by 20K and 10K in comparison, for the 16µm and 21µm devices respectively.

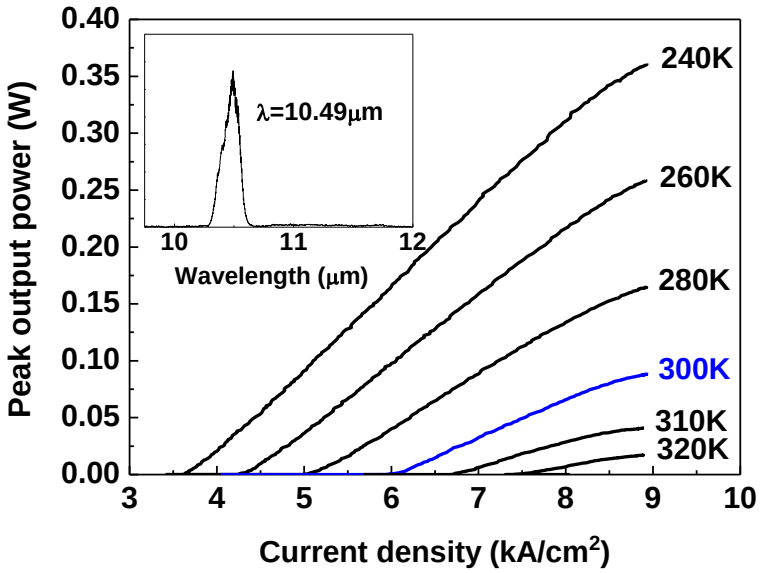

Figure 5.9: Peak output power vs. current density for a 3mm-long, 16μm-wide device fabricated from wafer MR3069. Inset: High-resolution spectra.

Figure 5.10 shows T_0 for the same 3mm-long 16μm-wide device from the usual fit of J_{th} vs. T. As discussed above, the motivation behind the addition of $Al_{0.75}Ga_{0.25}As$ barriers within the injector region of MR3069 was the desire to increase the high-temperature performance of devices. From the J_{th} vs. T data it is seen that a characteristic temperature of T_0=121±33K is observed for this QCL, which appears to represent an increase of ~20K in comparison to both MR3066 and MR3076 (containing $Al_{0.45}Ga_{0.55}As$ barriers). However, due to the large accompanying uncertainty in this value of T_0, this conclusion cannot be stated with any confidence without a larger sample of device characteristics.

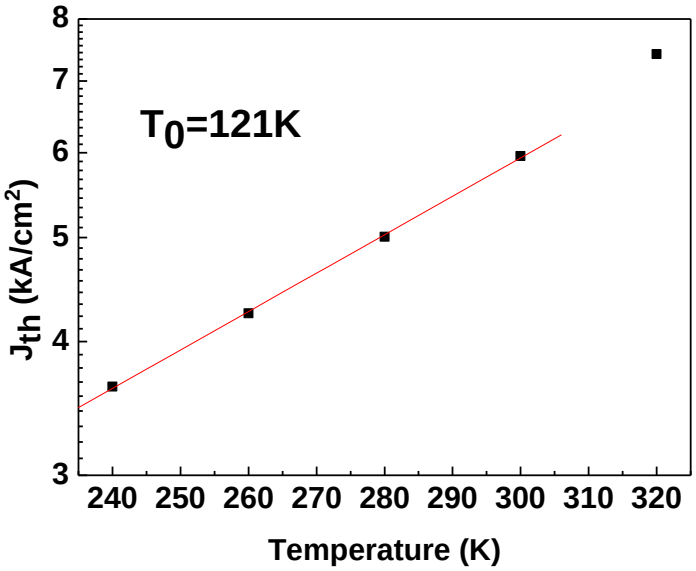

Figure 5.10: Threshold current density vs. operating temperature for a 3mm-long, 16µm-wide device fabricated from MR3069, yielding T_0=121K.

MR3082

Wafer MR3082 replicates the core region design, $Al_{0.75}Ga_{0.25}As$ injector region barriers and cladding layer structure of MR3069, but replaces the superlattice transitional layer with the stepped InGaP/InGaAlP TL present in MR3076. Shown in figure 5.11 is the L-I data and emission spectra for a 16µm-wide device, showing peak emission at λ=10.57µm - slightly longer than was observed previously for MR3069. Threshold current densities at lower temperatures are consistent with those of MR3069, with J_{th}=3.3kA/cm^2 measured at 240K. As can be seen however, the maximum operating temperature for this device is only slightly above 280K, at which point J_{th}=5.0kA/cm^2.

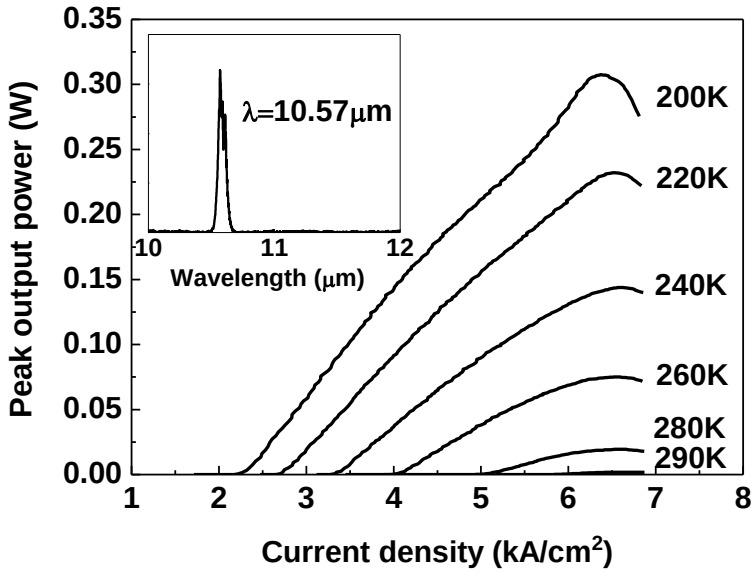

Figure 5.11: Peak output power vs. current density for a 3mm-long, 16μm-wide device fabricated from wafer MR3082. Inset: High-resolution spectra.

Low temperature peak output power is found to be 0.14W at 240K, less than half that typically observed at room temperature for other devices featured in this chapter, while at 280K output power is substantially lower with approximately 0.02W being measured. This reduced high-temperature performance is replicated in wider devices, where powers of ~0.17W and ~0.012W were recorded at 240K and 280K respectively. A characteristic temperature of T_0=99±16K can be extracted from the J_{th} vs. T data shown in figure 5.12, while a 21μm-wide device exhibited T_0=99±22K.

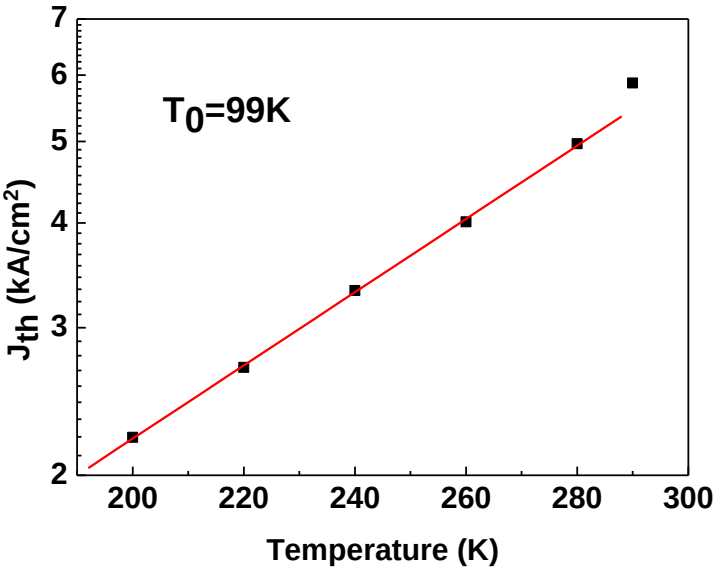

Figure 5.12: Threshold current density vs. operating temperature for a 3mm-long, 16µm-wide device fabricated from MR3082, yielding T_0=99K.

Table 5.2 contains a summary of the performance characteristics for the set of 3mm-long, 16µm-wide devices representing each wafer. It can be seen that the emission wavelengths remain consistent between devices with the same core region design i.e. MR3066/76 and MR3069/82, as would be expected. It was hoped the addition of $Al_{0.75}Ga_{0.25}As$ barriers in the core region of devices MR3069 and MR3082 would improve high-temperature performance by limiting the loss of electrons from the upper level of the active region to above-barrier continuum states. Enhancements that may have been expected include an increase in the maximum temperature of laser operation, a lowering of the threshold current densities at higher temperatures and a concomitant increase in the device characteristic temperature T_0. From the data relating to MR3069 and MR3082 however, the addition of $Al_{0.75}Ga_{0.25}As$ barriers is seen to have a detrimental effect on these areas of operation. No lowering of J_{th} is seen at higher temperatures when compared to MR3066 and MR3076, and at lower temperatures J_{th} has increased in comparison to the devices without $Al_{0.75}Ga_{0.25}As$ barriers. Operating voltages, particularly at 77K also appear to increase with the addition of $Al_{0.75}Ga_{0.25}As$ barriers to the QCL active region. The maximum temperature of operation has been reduced by T~20K in the case of MR3069 and T~50K for MR3082 when compared to devices with $Al_{0.45}Ga_{0.55}As$ barriers. Due to the large uncertainty in T_0 measurements, it

is also difficult to conclude that characteristic temperatures have been increased with respect to MR3066 and MR3076. It would appear then that the $Al_{0.75}Ga_{0.25}As$ barriers have not succeeded in producing the desired improvements in performance, the possible reasons for which are discussed in the next section.

In contrast to the difference between lasers with and without $Al_{0.75}Ga_{0.25}As$ barriers, very little difference in performance is observed for devices incorporating either the superlattice or stepped transitional layers. Threshold currents are consistent between MR3066 and MR3076, as are the maximum operating temperatures, while only a small increase in operating voltage is seen at low temperature for the stepped T.L. With the exception of MR3082 which operated at lower currents in comparison to all other devices, optical output power remains reasonably consistent across all devices at both room and low-temperature.

Wafer	**λ_{300K} (μm)**	**J_{th} (kA/cm^2)**	**Peak Power (W)**	**V_{max} (V)**	**T_0 (K)**	**T_{max} (K)**
MR3066 **Superlattice TL $Al_{0.45}Ga_{0.55}As$ Barriers**	10.43	3.0 (240K) 5.3 (300K)	0.21 (240K) 0.08 (300K)	29 (300K) 34 (80K)	102	340
MR3076 **Stepped TL $Al_{0.45}Ga_{0.55}As$ Barriers**	10.40	2.7 (240K) 5.1 (300K)	0.32 (240K) 0.13 (300K)	30 (300K) 36.5 (80K)	95	340
MR3069 **Superlattice TL $Al_{0.75}Ga_{0.25}As$ Barriers**	10.49	3.6 (240K) 6.0 (300K)	0.36 (240K) 0.09 (300K)	34 (300K) 42 (80K)	121	~320
MR3082 **Stepped TL $Al_{0.75}Ga_{0.25}As$ Barriers**	10.57	3.3 (240K) 5.0 (280K)	0.14 (240K) 0.02 (280K)	30 (300K) 40 (80K)	99	~290

Table 5.2: Performance summary for devices MR3066 through MR3082.

The increase in threshold current that results from the addition of $Al_{0.75}Ga_{0.25}As$ barriers is an undesired consequence of this particular modification. It is possible that rather than contributing to the blocking of electrons in the upper level of the active region, these high aluminium content barriers are providing an additional escape path for electrons in the form of scattering into states associated with the barrier's X-valley. Figure 5.13 shows a portion of the Γ-point and X-point conduction band profiles for MR3069, containing the four-well active region with upper and lower laser levels E_u and E_l respectively, as well as the three $Al_{0.75}Ga_{0.25}As$ barriers contained within the injector region. Also shown in figure 5.13 are the three lowest electronic states within the X-valleys of the $Al_{0.75}Ga_{0.25}As$ barriers. As the upper level wavefunction does not fully penetrate the injector region, it was assumed that Γ-X scattering would not significantly affect device performance despite the fact that there are three states lying within 50meV of E_u.

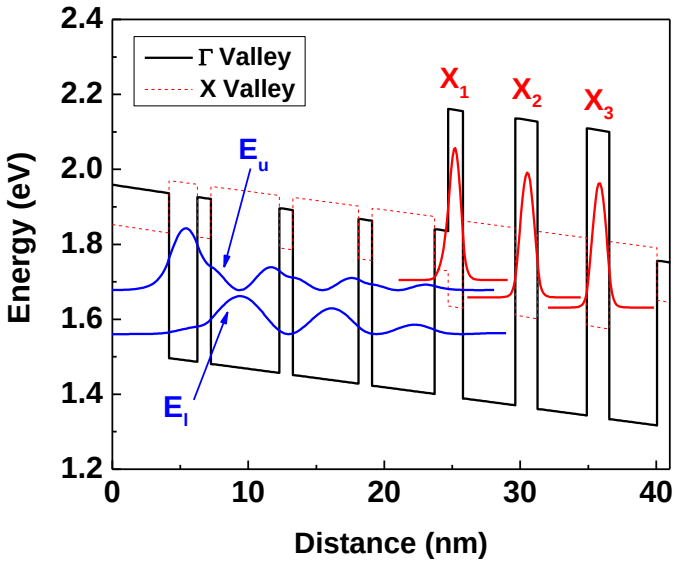

Figure 5.13: Γ-point and X-point conduction band profiles for the core region of MR3069 and MR3082 under a bias of 48kV/cm^2. The profile includes the moduli-squared of the electronic wavefunctions associated with the optical transition (shown in blue), and lowest electronic states associated with the X-vealley in the high-Al $Al_{0.75}Ga_{0.25}As$ barriers (red).

It has previously been shown however, that the position of the X-valley states within the device core region can severely limit device performance, particularly if they lie below the upper laser level, or very close above it. Wilson et al[5] showed that for QCL devices

in which the lowest X-valley state in the injection barrier was below the upper laser level (ΔE~35meV), lasing was severely compromised by Γ-X scattering causing a reduction in injection efficiency and population inversion. While the X-valley states in this case are those in the $Al_{0.75}Ga_{0.25}As$ exit barrier and the two following high-Al barriers, it is possible that the same scattering is occurring albeit on a reduced scale due to the fact that E_u only just penetrates to the injection barrier. It can be seen from figure 5.13 that E_u is positioned approximately 27meV below the X-valley state X_1, while being 19meV above X_2. The presence of Γ-X scattering would lead to a reduced population inversion in the device active region and may go towards explaining the slightly higher threshold current densities observed when compared to devices based on MR3066 and MR3076 which do not include high-Al barriers in the core. It is also possible that the exit barrier height and thickness are reducing the tunnelling rate τ_i^{-1}, from the exit barrier into the injector region. Since τ_i^{-1} is essentially inversely proportional to the width and height of the exit barrier[4], it may be that a reduction in one or both of these parameters (by reducing the Al content of the barrier for example) may help to improve device performance.

5.4 Conclusions

This chapter has been concerned with efforts to both reduce the large operating voltages observed in GaAs-based QCLs with InAlP waveguides (as described in chapter four), and to improve the high-temperature performance of these same devices. It has been shown how, by altering the composition and configuration of the transitional layers at the GaAs/InAlP interfaces within devices, operating voltages can be substantially reduced. This achievement demonstrates the importance of careful management of electron flow at these interfaces within the QCL structure, although there appears to be scope for further refinements as operating voltages remain high in comparison to devices with InGaP waveguides as described in the beginning of chapter four. The performance of these new devices in terms of the threshold current density does not quite reach the low levels observed for the previous InAlP waveguide QCLs with double-phonon active region, but nonetheless remains superior to that reported to-date for GaAs-based devices with more conventional GaAs and AlGaAs waveguide

structures[6-11]. The prospect of these devices operating in the CW regime appears remote however, while operating voltages remain comparatively high.

The addition of $Al_{0.75}Ga_{0.25}As$ barriers in the injector region was a strategy to reduce the escape of electrons into continuum states and improve the high-temperature performance of devices. No such performance enhancement could be ascertained however, with some evidence that threshold current densities were increased in comparison to devices with lower aluminium content $Al_{0.45}Ga_{0.55}As$ barriers. It is possible that this increase in J_{th} is related to the X-valley states in the high-Al barriers, although further investigation would be required to confirm this with any certainty. It is also possible that the reduced dipole matrix element of the diagonal transition within the active region is contributing to the reduced performance levels through a reduced optical gain. Whatever mechanism may be responsible, a reduction in both threshold current and operating voltage would need to be achieved in order to reduce the amount of device heating and enhance the possibility of CW operation.

1. D. P. Xu, A. Mirabedini, M. D'Souza, S. Li, D. Botez, A. Lyakh, Y. J. Shen, P. Zory and C. Gmachl, *Room-temperature, mid-infrared (λ=4.7μm) electroluminescence from single-stage intersubband GaAs-based edge emitters*, Applied Physics Letters, **85**, 4573-4575, (2004).

2. D. P. Xu, M. D'Souza, J. C. Shin, L. J. Mawst and D. Botez, *InGaAs/GaAsP/AlGaAs, deep-well, quantum-cascade light-emitting structures grown by metalorganic chemical vapor deposition*, Journal of Crystal Growth, **310**, 2370-2376, (2008).

3. J. C. Shin, M. D'Souza, Z. Liu, J. Kirch, L. J. Mawst, D. Botez, I. Vurgaftman and J. R. Meyer, *Highly temperature insensitive, deep-well 4.8μm emitting quantum cascade semiconductor lasers*, Applied Physics Letters, **94**, 201103, (2009).

4. Q. K. Yang, C. Mann, F. Fuchs, R. Kiefer, K. Kohler, N. Rollbuhler, H. Schneider and J. Wagner, *Improvement of λ~5μm quantum cascade lasers by blocking barriers in the active regions*, Applied Physics Letters, **80**, 2048-2050, (2002).

5. L. R. Wilson, D. A. Carder, J. W. Cockburn, R. P. Green, D. G. Revin, M. J. Steer, M. Hopkinson, G. Hill and R. Airey, *Intervalley scattering in GaAs-AlAs quantum cascade lasers*, Applied Physics Letters, **81**, 1378-1380, (2002).

6. C. Pflugl, W. Schrenk, S. Anders, G. Strasser, C. Becker, C. Sirtori, Y. Bonetti and A. Muller, *High-temperature performance of GaAs-based bound-to-continuum quantum-cascade lasers*, Applied Physics Letters, **83**, 4698-4700, (2003).

7. J. Q. Liu, F. Q. Liu, L. Li, Y. Shao, Y. Guo and Z. G. Wang, *High-power and low-threshold-current-density GaAs/AlGaAs quantum cascade lasers*, Chinese Physics Letters, **23**, 1784-1786, (2006).

8. J. Q. Liu, F. Q. Liu, S. Ye, L. Lu, G. Yu, Z. G. Wang and L. C. Wang, *High-duty-cycle operation of GaAs/AlGaAs quantum cascade laser above liquid nitrogen temperature*, Chinese Physics Letters, **23**, 2968-2971, (2006).

9. S. Hofling, V. D. Jovanovic, D. Indjin, J. P. Reithmaier, A. Forchel, Z. Ikonic, N. Vukmirovic, P. Harrison, A. Mircetic and V. Milanovic, *Dependence of saturation effects on electron confinement and injector doping in GaAs/$Al_{0.45}Ga_{0.55}As$ quantum-cascade lasers*, Applied Physics Letters, **88**, 251109, (2006).

10. M. Bugajski, K. Kosiel, A. Szerling, J. Kubacka-Traczyk, I. Sankowska, P. Karbownik, A. Trajnerowicz, E. P. Karbownik, K. Pierscinski and D. Pierscinska, *GaAs/AlGaAs (~9.4μm) quantum cascade lasers operating at 260K*, Bulletin of the Polish Academy of Sciences-Technical Sciences, **58**, 471-476, (2010).

11. K. Pierscinski, D. Pierscinska, M. Iwinska, K. Kosiel, A. Szerling, P. Karbownik and M. Bugajski, *Investigation of thermal properties of mid-infrared AlGaAs/GaAs quantum cascade lasers*, Journal of Applied Physics, **112**, 043112, (2012).

Chapter Six

Continuous-wave Operation of a GaAs-based QCL with InGaP Waveguide and Double-phonon Active Region

6.1 Introduction

Chapters four and five have outlined the strategies employed to improve the performance of GaAs-based QCLs using both InGaP and InAlP waveguides. In the case of devices with InAlP waveguides, it was seen how the introduction of transitional layers positioned at the interfaces between GaAs and InAlP led to a reduction in the large operating voltages that were observed in the first generation of devices. When contrasted to the more typical QCL voltages observed for lasers with InGaP waveguides however, these voltages were still excessive and would undoubtedly hinder operation at higher duty cycles and CW. In order to provide further enhancements to the performance of these GaAs-based QCLs - with a possible view to CW operation - it was decided to exploit, in combination, the design features of several of the lasers featured in chapter four.

It was seen how the introduction of a double-phonon active region design for devices featuring $In_{0.47}Al_{0.53}P$ waveguides, resulted in a significant reduction in measured threshold current densities (see section 4.6.2). It was also observed how devices with $In_{0.49}Ga_{0.51}P$ waveguides demonstrated typical operating voltages of ~14V at room temperature, compared to 25V for lasers using InAlP. Therefore, rather than continuing

with InAlP as a waveguide material, the next iteration in wafer design combines the InGaP waveguide structure of MR2784, with the double-phonon active region of MR2790 and later devices, in an attempt to combine these low threshold currents and operating voltages.

6.2 Wafer design

As with all designs presented in this thesis, wafers were grown using MOVPE under the conditions outlined in section 4.5.

MR3079

Shown in figure 6.1 is a schematic representation of the layer structure for wafer MR3079. As already noted, the design replicates the cladding structure and double-phonon active region of wafer MR2790, but replaces the $In_{0.47}Al_{0.53}P$ waveguide with $In_{0.49}Ga_{0.51}P$, as was used in wafers MR2784 and MR2785. Also in common with the previous InAlP wafers, transitional layers are included at two of the GaAs/InGaP interfaces of the structure in an attempt to further enhance the flow of electrons through devices. The first transitional layer (TL1) shown in figure 6.1 consists of 40nm of $In_{0.49}Ga_{0.51}P$ (N=1x10^{18}cm^{-3}) followed by 60nm of $In_{0.49}Ga_{0.51}P$ with graded doping from N=1x10^{18}cm^{-3} → 1x10^{17}cm^{-3}. Transitional layer 2 (TL2) is formed from 60nm of $In_{0.49}Ga_{0.51}P$ with graded doping from N=1x10^{17}cm^{-3} → 1x10^{18}cm^{-3} followed by a further 60nm of $In_{0.49}Ga_{0.51}P$ (N=1x10^{17}cm^{-3}).

Beginning from the GaAs substrate, the complete layer sequence for MR3079 was: 1µm GaAs cladding (N=3x10^{18}cm^{-3}), TL1, 3µm $In_{0.49}Ga_{0.51}P$ (N=1x10^{17}cm^{-3}) waveguide and 0.2µm GaAs spacer layer (N=5x10^{16}cm^{-3}), followed by the 55-period GaAs/$Al_{0.45}Ga_{0.55}As$ double-phonon core region (design given in section 4.5). The sequence then repeats in reverse with 0.2µm GaAs spacer, 3µm $In_{0.49}Ga_{0.51}P$ waveguide, TL2 and finally 1µm GaAs top cladding.

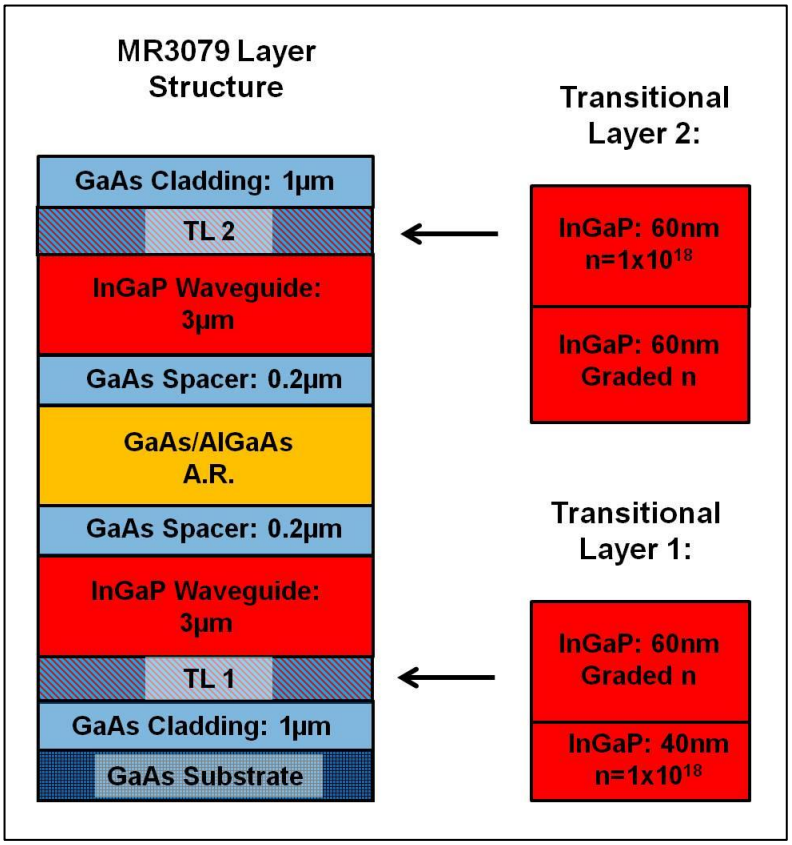

Figure 6.1: Schematic illustration of the semiconductor layer structure for MR3079, including transitional layers.

6.3 Device Performance

6.3.1 Optical and Electrical Performance

After processing, a set of 3mm-long, 16µm and 21µm-wide lasers were characterised in the usual manner, with figure 6.2 showing the L-I characteristics for a 16µm-wide device operating in pulsed mode. It can be seen that as expected, the emission wavelength of λ=10.42µm remains almost identical to that of the previous series of lasers which contain the same core region design (MR3066 and MR3076). More notable is the reduction in threshold current density that is observed when compared to the lowest measured J_{th} for devices with InGaP waveguides described in chapter four. At 240K, device MR3079 had a threshold current density of J_{th}=2.6kA/cm^2, rising to J_{th}=5.0kA/cm^2 at room temperature. Threshold currents for a 21µm-wide device were found to be consistent with the narrower laser, with J_{th}=2.7kA/cm^2 and J_{th}=5.1kA/cm^2 at

240K and 300K respectively. These threshold currents represent reductions of around 40% when compared to MR2784 (J_{th}=4.3kA/cm^2 and J_{th}=8.0kA/cm^2 at 240K and 300K respectively) and MR2785 (J_{th}=4.7kA/cm^2 and J_{th}=8.6kA/cm^2 at 240K and 300K respectively). This performance enhancement mirrors that observed in chapter four when switching from a single-phonon active region design to the double-phonon active region of samples MR2789 and MR2790, and demonstrates that the very low threshold currents subsequently observed are not restricted solely to QCLs with InAlP waveguides.

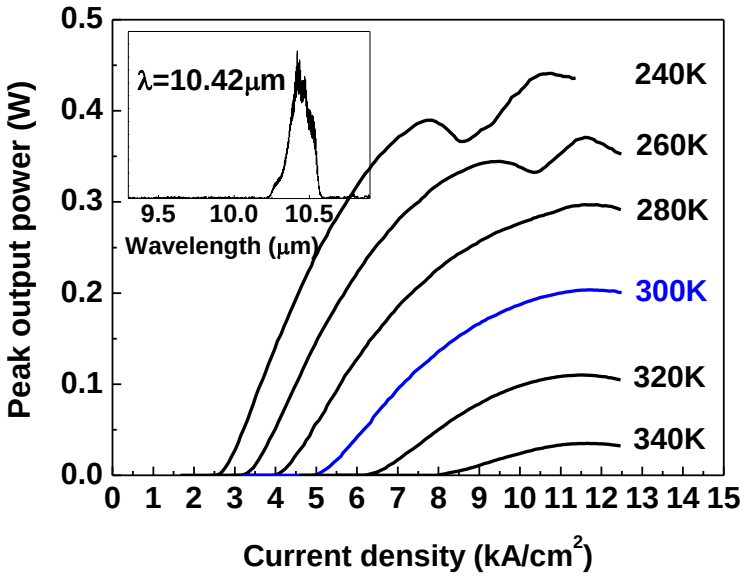

Figure 6.2: Peak output power vs. drive current (pulsed regime) for a 3mm-long, 16μm-wide device fabricated from wafer MR3079. Inset: High-resolution (0.25cm^{-1}) FTIR spectra showing emission at 10.42μm.

As would be expected for a device with an identical active region, threshold currents for MR3079 are consistent with those observed for devices MR3066 and MR3076 from chapter five. Also shown in figure 6.2 (as well as figures 5.5 and 5.7) is the atypical, low-temperature L-I behaviour close to rollover, where device output power begins to fluctuate. This behaviour could be caused by changes in the beam profile as the laser output switches between transverse laser modes at high currents, which combined with the non-unity collection efficiency of the laboratory optics can be recorded as a change in device output power. Peak output power for MR3079 was found to be 0.44W at 240K, falling to 0.20W at 300K for a 16μm wide device, while for a wider 21μm laser it

varied from 0.72W to 0.31W at 240K and 300K respectively. These powers compare favourably with the devices presented in chapter five, where maximum output was measured at 0.36W at 240K (MR3069) and 0.13W at 300K (MR3076), although they do not match those observed for MR2784 - 1.58W and 0.56W at room and low-temperature respectively. Figure 6.3 shows the calculated characteristic temperature for MR3079 of T_0=90±13K, which is consistent with all devices presented in chapter four.

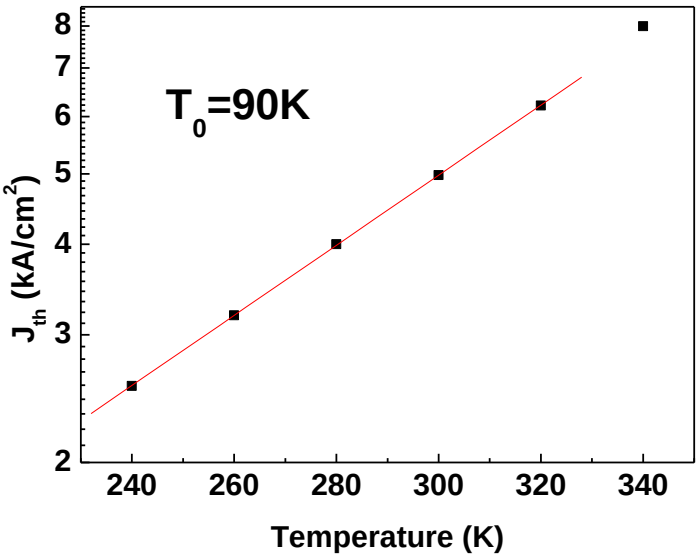

Figure 6.3: Threshold current density vs. operating temperature for a 3mm-long, 16µm-wide QCL fabricated from MR3079. The linear fit yields a characteristic temerature of T_0=90K.

The reduction in J_{th} that is observed for MR3079 represents the achievement of one aim of the decision to combine a double-phonon active region with an InGaP waveguide. A second desired outcome was a reduction in the large operating voltages that are a feature of devices incorporating InAlP waveguides, and shown in figure 6.4 are the I-V characteristics for a 16µm-wide device at both room temperature and 80K. From the data it is immediately apparent that operating voltages are reduced in comparison to the InAlP devices featured in chapter five, with voltage at room-temperature threshold (J_{th}=5.0kA/cm^2) measured at 15.7V. This represents a reduction of ~6.5V when compared to MR3076 (which had the lowest measured voltage at threshold). This voltage reduction is maintained over the entire operating range of the device, where at

9kA/cm^2 (the maximum current density for the previous lasers), V=20.3V compared to between 29V and 34V for MR3066 through MR3082. The disparity in voltage is increased at 80K where V=19.7V for MR3079, while for devices MR3066 through MR3082 voltages ranged from 34V to 42V.

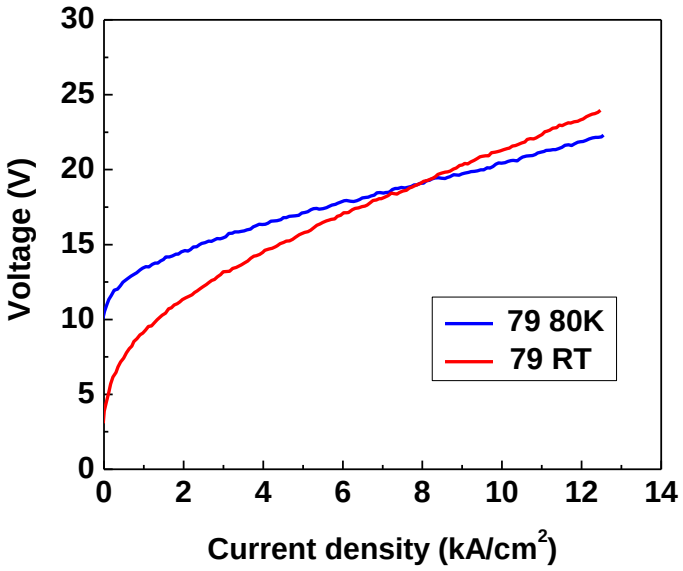

Figure 6.4: I-V characteristics for MR3079 at 80K and room-temperature.

The voltages observed for MR3079 represent a clear improvement over those measured for the InAlP devices, whilst also approaching those levels measured for the original InGaP lasers from chapter four. It is clear that the re-introduction of InGaP as a waveguide material has considerable benefits in terms of device operating voltage, while threshold currents are enhanced through the introduction of the double-phonon active region. Further enhancements in laser performance are possible through the addition of high-reflectivity (HR) coatings to device facets. Equation 3.5 shows how an increase in the reflectivity of one (or both) facets results in a decrease in mirror loss for the laser cavity, which should (from equation 3.4) result in a subsequent reduction in threshold current as well as an increase in optical output power. An HR coating consisting of a 500nm insulating layer of SiO_2 deposited by PECVD, followed by the evaporation of 10nm Ti and 100nm Au[1], was applied to a second 16µm-wide device

from wafer MR3079, before optical and electrical characterisation, the results of which are presented in the following section.

6.3.2 MR3079HR - Pulsed Mode Operation

L-I characteristics for the 3mm-long, 16µm-wide HR-coated device are shown in figure 6.5. As expected, the threshold current density has been reduced with J_{th}=2.3kA/cm^2 observed at 240K, rising to J_{th}=4.6kA/cm^2 at 300K. These currents represent a reduction of ~10% in comparison to the non-HR MR3079 QCLs presented previously, and are consistent with those measured for MR2790 - which had the lowest observed J_{th} of all devices presented in this thesis. Peak output power has increased in comparison to MR3079, with P=0.73W and P=0.31W observed at 240K and 300K respectively – an increase of 290mW and 110mW over non-coated lasers.

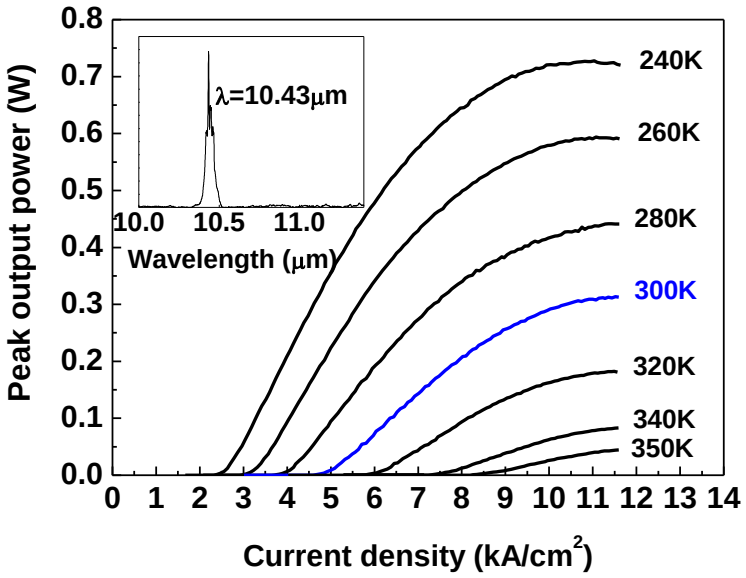

Figure 6.5: Peak output power vs. drive current (pulsed regime) for a 3mm-long, 16µm-wide device with high-reflectivity coating on the back facet (MR3079HR). Inset: FTIR spectra showing emission at 10.43µm.

Peak emission for this device is seen to occur at λ=10.43µm, virtually identical to its non-coated counterpart as would be expected, while a maximum operating temperature of 350K is also observed. The characteristic temperature of T_0=91±13K (figure 6.6) is also consistent with that measured for MR3079, as well as the previous devices with InGaP waveguides featured in chapter four.

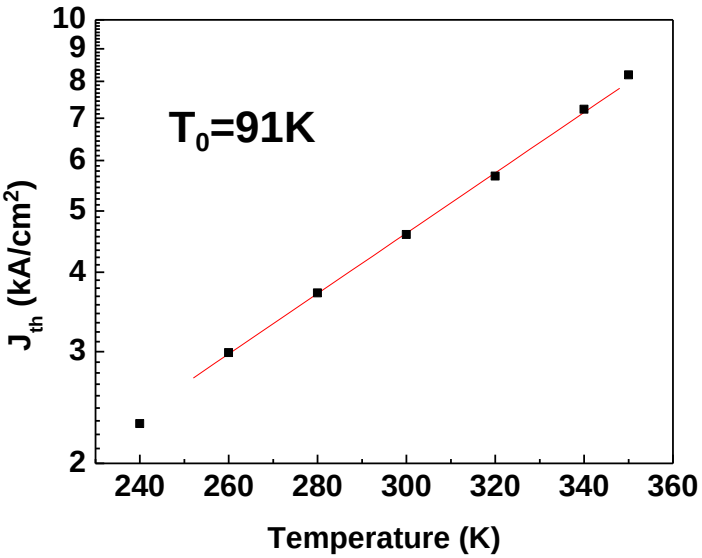

Figure 6.6: Threshold current density vs. operating temperature for MR3079HR, yielding T_0=91K.

Electrical characteristics remain essentially unchanged compared to MR3079, with voltage at room temperature threshold measured as V=15.8V, rising to V=23.1V at maximum drive current (figure 6.7).

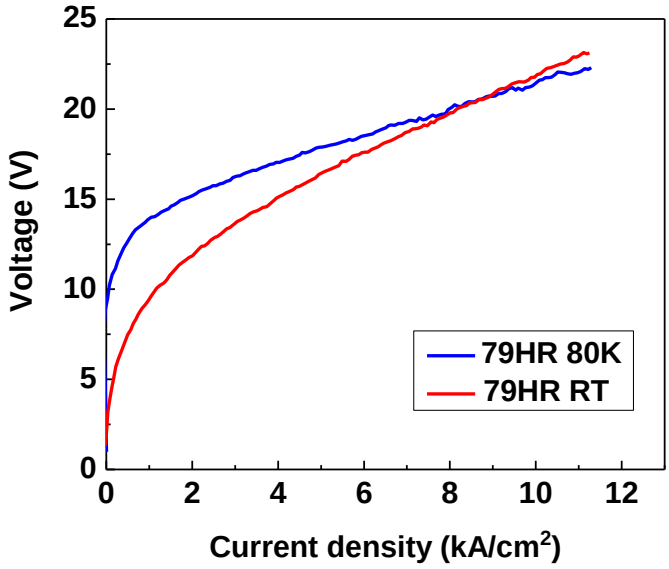

Figure 6.7: I-V characteristics for MR3079HR taken at 80K and room-temperature.

With the operating voltage for MR3079 lowered to levels approaching those observed for MR2784 and MR2785, and the further reduction in J_{th} achieved by the addition of an HR coating, it was decided to test laser operation in the CW regime. Previous demonstrations of CW operation with InP-based QCLs have utilised either advanced processing techniques such as the buried heterostructure configuration[2-4], or made use of highly thermally conductive submount materials such as copper, aluminium nitride or diamond[5-7]. Due to the standard way in which these devices were processed, and the poor thermal management afforded by the T05 headers on to which they would normally be soldered, gold-coated aluminium-nitride ceramic tiles were used as an alternative. In order to further increase the heat extraction from the laser ridges, ~5µm of electroplated gold was applied to the top contact of a sample of previously fabricated devices, before addition of the HR coating. For the purposes of testing devices, a row of HR-coated lasers were then cleaved into individual chips ~420µm wide, each one encompassing a single laser ridge. These chips were then indium-soldered epi-layer down onto the AlN tiles and wire-bonded from chip to tile for electrical contact.

A selection of 16µm and 21µm-wide lasers were tested in pulsed mode to determine threshold current, and the devices exhibiting the lowest J_{th} were then selected for testing in the CW regime.

6.3.3 MR3079HR - Continuous-wave Operation

Shown in figures 6.8 and 6.9 are the CW optical and electrical characteristics measured for 16µm and 21µm-wide epi-down mounted devices. The inset to the figures show the high-resolution (0.25cm^{-1}) spectra for each device recorded at 20K. It is seen that peak emission occurs at λ=10.27µm for the 16µm-wide device and is single mode (in comparison to the multi-mode emission observed in pulsed operation), while the 21µm laser has a double-peak at λ=10.17µm and λ=10.23µm. Current-voltage characteristics at 20K for both devices are virtually identical over the entire operating current range, with voltage at threshold measured as V=12.1V and V=12.0V for the 16µm and 21µm-wide lasers respectively. Maximum voltages of V=12.7V (16µm) and V=12.3V (21µm) are also observed.

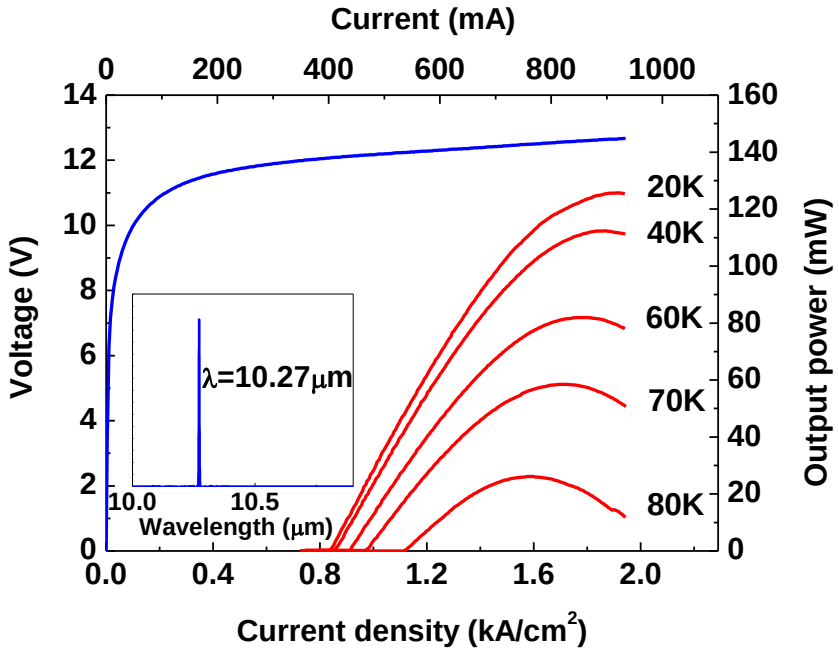

Figure 6.8: Continuous-wave optical and electrical characteristics for a 3mm-long, 16µm-wide HR-coated device (MR3079HR) mounted epi-layer down on AlN tiles. The I-V (20K) is shown in blue and the L-I in red. Inset: FTIR spectra.

Threshold current densities for these devices begin at J_{th}=0.84kA/cm^2 and J_{th}=0.77kA/cm^2 at 20K for the 16µm and 21µm-wide lasers respectively. These then rise to J_{th}=1.1kA/cm^2 at the maximum operating temperature of 80K for the 16µm-wide laser, and J_{th}=1.0kA/cm^2 at 65K for the 21µm-wide device. Peak output powers of P=126mW at 20K, falling to P=26mW at 80K are observed for the 16µm-wide device, while P=83mW and P=6mW at 80K and 65K respectively were measured for the wider laser.

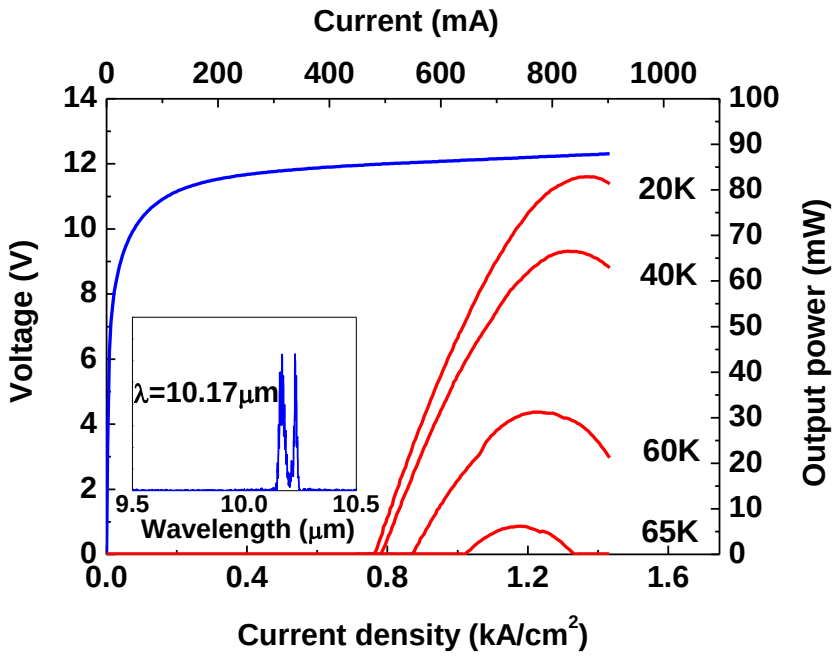

Figure 6.9: CW optical and electrical characteristics for a 3mm-long, 21µm-wide HR-coated device (MR3079HR) mounted epi-layer down. The I-V (20K) is shown in blue and the L-I in red. Inset: FTIR spectra.

This CW operation represents the first time such performance has been observed from GaAs devices at Sheffield, and is only one of a handful of times that CW operation has been reported for any GaAs-based QCL[8-10]. The best performing CW GaAs QCL to-date, reported by Page and co-workers[10], had a peak output power of 80mW and threshold current of 470mA (~3.3kA/cm^2) at 77K, along with a maximum operating temperature of 150K. These devices however, used non-standard fabrication techniques such as proton implantation to limit the current flow through the laser ridge and thus minimise device heating, as well as omitting an insulating dielectric layer. In view of

this, the performance achieved from our standard ridge-processed devices is encouraging and suggests that with further optimisation, the possibility exists of exceeding current state of the art CW performance. Possible improvements to consider include tailoring the width and doping level of the InGaP waveguide to ensure losses are minimised at the emission wavelength displayed by the lasers, while alterations to the active region design itself - for example by optimising the spatial nature of the optical transition - may also result in a further reduction in threshold current density. In terms of device processing, a switch to a trench configuration rather than the ridge pattern used in this work could allow a greater volume of electroplated gold to be deposited on the laser ridges, which in turn should aid the extraction of heat from the ridge during CW operation. Bonding of these trenched lasers to mounts with a higher thermal conductivity than AlN should also lead to more efficient heat extraction and allow devices to operate in CW at higher temperatures.

6.4 Conclusions

The work presented in this section has been concerned with pushing the performance limits of our GaAs-based QCLs with a view to eventual CW operation. It has been seen that the reintroduction of InGaP as a waveguide material, combined with a double-phonon active region results in pulsed regime laser characteristics that in some cases (i.e. threshold current) exceed current state-of-the-art levels, while in others (e.g. output power) remain at least comparable. The use of AlN tiles as device mounts, with their excellent capacity for thermal management, allows advantage to be taken of the reduced operating voltages and low-temperature threshold currents that are observed for these devices, and lead to the eventual achievement of CW operation. While the CW performance by no means matches that of the best CW GaAs devices reported in terms of output power or maximum operating temperature, the observed low-temperature threshold currents do in fact represent a reduction compared to those reported by Page et al[10]. It would seem reasonable therefore, to speculate that further improvements in CW performance could be achieved in future through the combination of improvements outlined above.

1. D. G. Revin, S. Zhang, J. P. Commin, K. Kennedy, A. B. Krysa and J. W. Cockburn, *High-Peak-Power Room-Temperature λ~3.6μm InGaAs-AlAs(Sb) Quantum Cascade Lasers*, IEEE Photonics Technology Letters, **22**, 757-759, (2010).

2. M. Beck, D. Hofstetter, T. Aellen, J. Faist, U. Oesterle, M. Ilegems, E. Gini and H. Melchior, *Continuous wave operation of a mid-infrared semiconductor laser at room temperature*, Science, **295**, 301-305, (2002).

3. D. A. Yarekha, M. Beck, S. Blaser, T. Aellen, E. Gini, D. Hofstetter and J. Faist, *Continuous-wave operation of quantum cascade laser emitting near 5.6μm*, Electronics Letters, **39**, 1123-1125, (2003).

4. T. Aellen, S. Blaser, M. Beck, D. Hofstetter, J. Faist and E. Gini, *Continuous-wave distributed-feedback quantum-cascade lasers on a Peltier cooler*, Applied Physics Letters, **83**, 1929-1931, (2003).

5. D. Hofstetter, M. Beck, T. Aellen, J. Faist, U. Oesterle, M. Ilegems, E. Gini and H. Melchior, *Continuous wave operation of a 9.3 mu m quantum cascade laser on a Peltier cooler*, Applied Physics Letters, **78**, 1964-1966, (2001).

6. J. S. Yu, S. R. Darvish, A. Evans, J. Nguyen, S. Slivken and M. Razeghi, *Room-temperature continuous-wave operation of quantum-cascade lasers at λ~4μm*, Applied Physics Letters, **88**, 041111, (2006).

7. J. S. Yu, A. Evans, S. Slivken, S. R. Darvish and M. Razeghi, *Temperature dependent characteristics of λ~3.8μm room-temperature continuous-wave quantum-cascade lasers*, Applied Physics Letters, **88**, 251118, (2006).

8. W. Schrenk, N. Finger, S. Gianordoli, E. Gornik and G. Strasser, *Continuous-wave operation of distributed feedback AlAs/GaAs superlattice quantum-cascade lasers*, Applied Physics Letters, **77**, 3328-3330, (2000).

9. H. Page, S. Dhillon, M. Calligaro, V. Ortiz and C. Sirtori, *Optimised device processing for continuous-wave operation in GaAs-based quantum cascade lasers*, Electronics Letters, **39**, 1053-1055, (2003).

10. H. Page, S. Dhillon, M. Calligaro, C. Becker, V. Ortiz and C. Sirtori, *Improved CW operation of GaAs-Based QC lasers: T-max=150 K*, IEEE Journal of Quantum Electronics, **40**, 665-672, (2004).

Chapter Seven

Conclusions and Future Outlook

This thesis has presented work aimed at advancing the performance of GaAs-based quantum cascade lasers and their associated waveguide structures. Historically, improvements in the performance of these devices has not kept pace with those of QCLs based on the InP material system, and so a strategy involving enhancements to both the QCL waveguide and active region has been employed in an attempt to address this disparity. Previous studies had shown that significant reductions in device threshold current density could be made by replacing the highly-doped GaAs waveguides that are commonly used in GaAs QCLs, with layers of InGaP. Lowering threshold current is a vital step on the road to improving the current state-of-the-art CW performance of these lasers.

Chapter four began by studying the effect that increasing the number of core region repeat periods of a previously studied GaAs QCL would have on device output. As expected, a significant increase in optical output power was observed (1.6W peak at 240K) which was interpreted as being a consequence of the increased modal overlap with the wider device core. A second new QCL design was also studied which replicated the wider core region, but altered the spatial nature of the optical transition within the device active region. By moving from a diagonal transition in which the confined electron states were localised in adjacent quantum wells, to a more vertical design in which the upper state partially penetrated the lower state well, it was thought that the intersubband gain could be increased through the large dipole matrix element associated with vertical optical transitions. The dramatic decrease in output power that was observed however (0.8W at 240K), suggested that the rather than an increase in gain, a larger than anticipated reduction in the active region population inversion had been achieved. This was thought to be a consequence of either a reduced upper state lifetime (due to the increased transition dipole matrix element), or a reduction in injection efficiency resulting from the decreased resonance between the upper laser

level and the injector level. In order to fully maximise device performance, future studies may need to include a focus on the optimisation of the spatial characteristics of the optical transition.

Calculations had suggested that a QCL waveguide consisting of InAlP layers should theoretically provide an increase in confinement of the optical mode compared to previous InGaP designs, due to the greater refractive index contrast between waveguide and core region. Bearing in mind the benefits to laser performance that this confinement increase might provide, two sets of devices were studied in which the previous InGaP waveguide layers were replaced by InAlP, with one laser also featuring a redesigned double-phonon active region. Characterisation of these QCLs revealed further reductions in threshold current in comparison to the equivalent lasers with InGaP waveguides, with the double-phonon device exhibiting the lowest threshold current densities yet observed for any GaAs-based QCL; $2kA/cm^2$ at 240K and $4kA/cm^2$ at room-temperature. Other device characteristics such as output power were at least comparable to the previous InGaP QCLs. Despite the low threshold currents however, all QCLs featuring InAlP waveguides exhibited large operating voltages - in some cases up to 60V at low temperature - and as a consequence many lasers failed during operation due to overheating. Those devices that were successfully characterised had to be done so under relatively low drive currents in order to prevent their failure. It was suggested that this excess voltage might be related to poor electron flow caused by the relatively large conduction band offset at the interfaces between the InAlP waveguide and the surrounding GaAs layers.

Chapter five therefore, focussed on the efforts made to reduce InAlP QCL operating voltages to more manageable levels. It was hoped that electron flow at the GaAs/InAlP interfaces could be improved by optimising the transitional layers between the GaAs and InAlP layers. Two transitional layer designs were tested; the first a superlattice of InGaP and InAlP and the second a ‘stepped’ design consisting of a thin layer of InGaP followed by a second thin InAlP layer. Keeping the previous double-phonon active region design, devices containing one or other of the two transitional layer designs were characterised in order to ascertain their effect on operating voltage. It was found that both designs resulted in a voltage reduction of ~12V at room-temperature and ~30V at 80K when compared to the InAlP QCLs from chapter four.

In addition to the effects of the transitional layers, a secondary study also looked at how increasing the aluminium content of several of the AlGaAs barriers within the injector region to 75% might affect the high-temperature performance of devices. This alteration to the core region was an attempt to limit the escape of electrons from the upper laser level into continuum states above the injector region. No performance enhancements were observed for these devices, and in some cases threshold currents were found to increase in comparison to devices with standard $Al_{0.45}Ga_{0.55}As$ barriers. It was thought that the high-Al content of the barriers was creating an escape channel for electrons in the form of X-valley states within the injector region. These states would decrease the overall efficiency of the active region and possibly counteract any potential advantages associated with the high-Al blocking barriers. A systematic study involving changes in barrier composition and X-valley position, and observation of the associated effects on device performance would be required to confirm this.

Although the reductions in operating voltage that were achieved through use of the transitional layers represented a positive progression, the voltages observed were still significantly higher than of earlier QCLs with InGaP waveguides. In addition to this, threshold currents were increased in comparison to the InAlP devices described in chapter four. If further performance enhancements are to be made, it would appear that future studies should include a concerted effort to fully understand the nature of the GaAs/InAlP interface, and the underlying causes of the excessive voltages that appear to be a consequence of the inclusion of InAlP. Determination of the precise nature of the conduction band profile at the GaAs/InAlP interfaces would be a useful endeavour in this regard, perhaps through methods such as the capacitance-voltage technique, or it may be possible to directly measure the voltage drops across the waveguide using Kelvin probe force microscopy (KFPM). The design of the InAlP waveguide could be altered somewhat, for example by thinning the InAlP layers in order to improve the flow of electrons through the structure, however this would come at a cost of increasing waveguide losses and may reduce some of the performance gains previously observed.

With the varied success achieved by using InAlP as a waveguide material, a reappraisal of InGaP was deemed appropriate in view of the low operating voltages that had previously been observed for InGaP waveguide devices in chapter four. Chapter six therefore, described how the successful double-phonon active region employed in the low-threshold InAlP QCLs was incorporated into a QCL structure with InGaP

waveguide layers, in an attempt to combine the low threshold currents and low operating voltages previously observed. Initial device characterisation revealed threshold currents that almost matched those of the InAlP QCLs, while as expected, operating voltages were reduced by a further 10V, to ~20V at room-temperature. The addition of a high-reflectivity coating to the back facet of the device led to a further reduction in threshold current, to a point where it was decided to attempt continuous wave operation. By utilising epi-layer-down bonding to AlN tiles, CW operation was observed up to a temperature of 80K - the first time CW lasing from a GaAs-based QCL had been observed at Sheffield.

Future work aimed at further improving the performance of these devices would be dependent on the waveguide material being considered. In the case of InGaP, due to the absence of the large operating voltages that were observed when using InAlP, immediate changes are likely to focus on improving the way devices are processed, as these would be relatively straightforward to implement. For example, by switching to a trench configuration to define the laser ridges and using narrower ridge widths and improved thermal packaging, heat flow away from the device core could easily be improved, thus enabling CW operation at higher temperatures. Furthermore, lowering the device emission wavelength could allow a reduction in waveguide loss and lead to an additional reduction in threshold current. This lowering of the threshold would also aid higher-temperature CW device performance.

InAlP has also shown promise as a new waveguide material for GaAs-based QCLs. The issue of large operating voltages however, must surely be addressed if its full potential is to be realised. Study of the GaAs/InAlP interfaces and the flow of electrons through them, would undoubtedly help in the pursuit of a solution to this problem. If voltages could be reduced to levels similar to those observed with InGaP, utilising the same changes in device processing outlined above could result in a dramatic leap in GaAs-based QCL performance. Although it may be some time before GaAs QCLs are able to match the CW performance of InP-based devices, the work outlined in this thesis represents very positive progress toward this ultimate goal.

Appendices

A1 - Calculation of Conduction Band Profiles and Electronic Wavefunctions

The conduction band profiles and accompanying electronic wavefunctions presented in this thesis were produced using 'ECA', a software package developed by Roland Teissier[1].

ECA allows the input of a GaAs/$Al_xGa_{1-x}As$ QCL core region structure, using the thickness of the GaAs wells and AlGaAs barriers as one input parameter, and the $Al_xGa_{1-x}As$ aluminium fraction (x) as the other. For the purposes of calculating the electronic wavefunctions and energy levels, the resulting conduction band profile is placed at the bottom of an infinite potential well, to which an electric field can be applied depending upon the desired alignment of energy levels. The program implements the transfer matrix method in order to solve the time-independent Schrödinger equation for the given potential profile, and return the electronic wavefuntions $\psi(z)$ and energy levels E for the QCL structure.

The GaAs/AlGaAs conduction band offset ΔE_c is calculated using a composition-dependent quadratic expression:

$$\Delta E_c = 911.2x + 147.4x^2 \qquad \text{(A1.1)}$$

where ΔE_c is in meV, and x is the $Al_xGa_{1-x}As$ aluminium fraction.

The effective masses of GaAs and $Al_xGa_{1-x}As$ used by ECA are as follows:

Material	Effective mass
GaAs	$0.067m_0$
$Al_xGa_{1-x}As$	$(0.067 + 0.042x)m_0$

Table A1.1: GaAs and $Al_xGa_{1-x}As$ electron effective masses used by the ECA software.

A2 - Calculation of Optical Mode Profiles

The optical mode profiles presented in this thesis were calculated using WGMOD (H-Scientific Ltd), an application which can determine the TM and TE mode profiles for a multi-layer structure if the refractive index and thickness of each layer is known. The refractive index n_{ref}, and absorption coefficient k are calculated for each layer using equations 2.30 to 2.33 (section 2.5), with the following values of effective mass m^* and high-frequency dielectric constant ε_∞:

Parameter	GaAs	$Al_{0.45}Ga_{0.55}As$	$In_{0.49}Ga_{0.51}P$	$In_{0.47}Al_{0.53}P$
m^* (m_0)	0.067[2]	0.100[2]	0.088[2]	0.150[3]
ε_∞	10.89[2]	9.66[2]	9.36[2]	8.10[4]

Table A2.1: Values of effective mass and high-frequency dielectric constant used in the calculation of refractive index and absorption coefficient for the QCL structures presented in this thesis.

The remaining parameters contained in equations 2.30 and 2.31 are standard physical constants, and thus n_{ref} and k can be determined for any wavelength λ, and doping concentration N (the electron scattering time is assumed to be $\tau=1\text{x}10^{-13}$s for all layers[5]). For the purposes of modelling, the core region is treated as a single layer with n_{ref} and k determined by an interpolation scheme based on the GaAs/AlGaAs ratio. As an example, for a wavelength of λ=9μm and using the layer doping levels of samples MR2785 and MR2789 given in section 4.5, the following values of n_{ref} and k for each layer are obtained:

Parameter at λ=9μm	GaAs Claddings	GaAs Spacer	GaAs/AlGaAs Core Region	$In_{0.49}Ga_{0.51}P$ Waveguide	$In_{0.47}Al_{0.53}P$ Waveguide
n_{ref}	2.76	3.29	3.23	3.05	2.84
k	0.0281	0.000393	0.0000702	0.000322	0.000203
α (cm^{-1})	390	5.48	0.980	4.50	2.84

Table A2.2: Refractive index, absorption coefficient and waveguide loss obtained for each layer of samples MR2785 and MR2789.

These values of n_{ref} and k, along with the corresponding layer thicknesses can be used to generate the required TM mode profile using the WGMOD software:

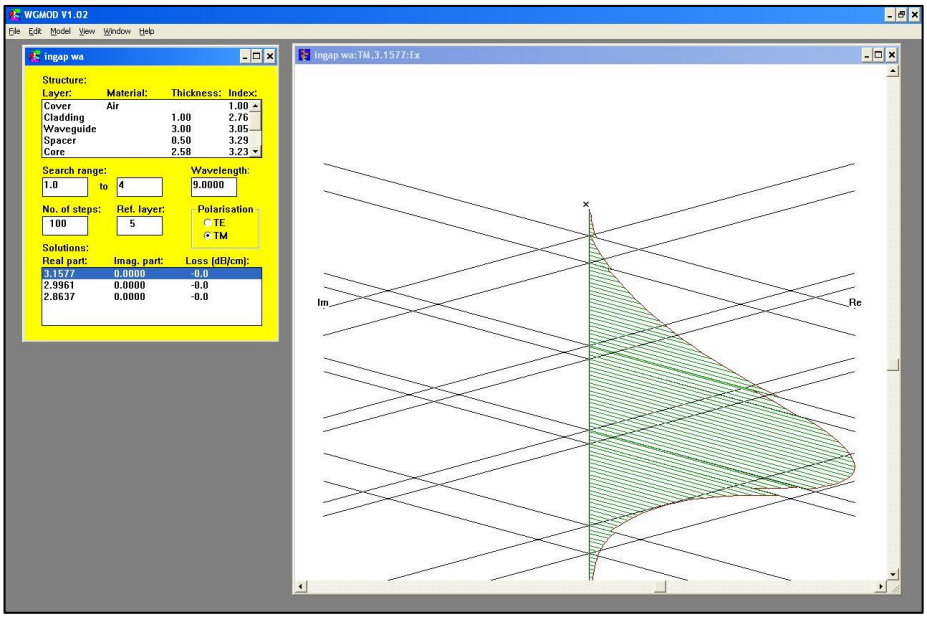

Figure A2.1: WGMOD software used to calculate optical mode profiles.

For a core region of width L, the overlap factor Γ is calculated simply as the ratio of the area of the optical mode bounded by the core, to that of the total mode area i.e.[6]:

$$\Gamma = \frac{\int_0^L E^2(z)}{\int_{-\infty}^{+\infty} E^2(z)} dz \qquad \text{(A2.1)}$$

The waveguide loss associated with each layer of the structure α_W^{Layer}, is given by[7]:

$$\alpha_W^{Layer} = \frac{2\omega k}{c} \tag{A2.2}$$

where ω is the angular frequency of emitted radiation and c the speed of light. Thus the total waveguide loss, α_W^{Tot} for the QCL structure is calculated as the sum of the individual layer losses, α_W^{Layer} multiplied by the proportion of the mode penetrating that layer (where L_i is the width of each individual layer):

$$\alpha_{\mathrm{W}}^{\mathrm{Tot}} = \sum \frac{\int_0^{L_i} E^2(z)}{\int_{-\infty}^{+\infty} E^2(z)} dz . \alpha_W^{Layer} \tag{A2.3}$$

1. Universite Montpellier 2, CNRS, Institut d'Electronique, Montpellier, France,

2. I. P. T. Institute, *New Semiconductor Materials: Characteristics and Properties [Online]*, Available at: http://www.ioffe.ru/SVA/NSM/Semicond/index.html, (2012).

3. S. Adachi, *Properties of Semiconductor Alloys*, (Wiley, 2009).

4. T. Hofmann, G. Leibiger, V. Gottschalch, I. Pietzonka and M. Schubert, *Infrared dielectric function and phonon modes of highly disordered* $(Al_xGa_{1-x})_{0.52}In_{0.48}P$, Physical Review B, **64**, 155206, (2001).

5. F. Capasso, A. Y. Cho, J. Faist, A. L. Hutchinson, C. Sirtori and D. L. Sivco, *Article Comprising a Semiconductor Waveguide Structure*, United States Patent 5502787, (1996).

6. J. Faist, *Quantum Casacde Lasers*, (Oxford, 2013).

7. M. Fox, *Optical Properties of Solids*, (OUP, 2001).